

AD-A045 022

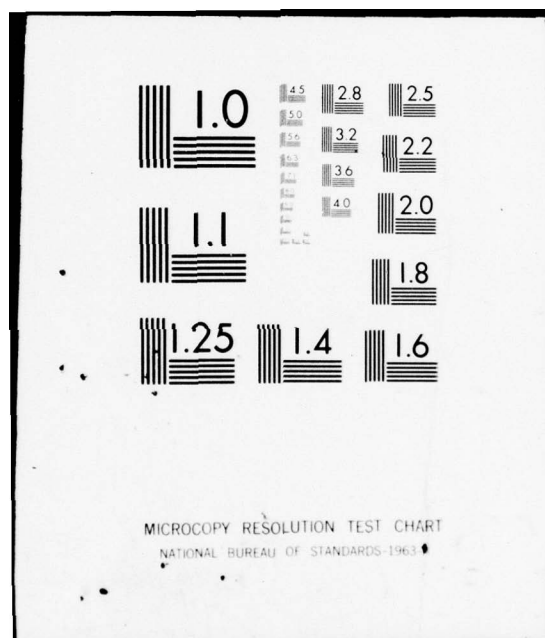
ARMY ENGINEER WATERWAYS EXPERIMENT STATION VICKSBURG MISS F/G 8/13  
GENERAL DEFORMATION (ELASTIC AND INELASTIC) AND STRESS DISTRIBUTION--ETC(U)  
SEP 77 R H LEDBETTER  
WES-TR-S-77-10

UNCLASSIFIED

NL

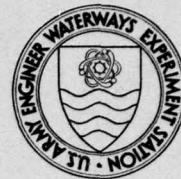
1 OF 2  
AD  
A045022







2  
B.S.



TECHNICAL REPORT S-77-10

AD A 045022

# GENERAL DEFORMATION (ELASTIC AND INELASTIC) AND STRESS DISTRIBUTION THEORY IN SOILS

by

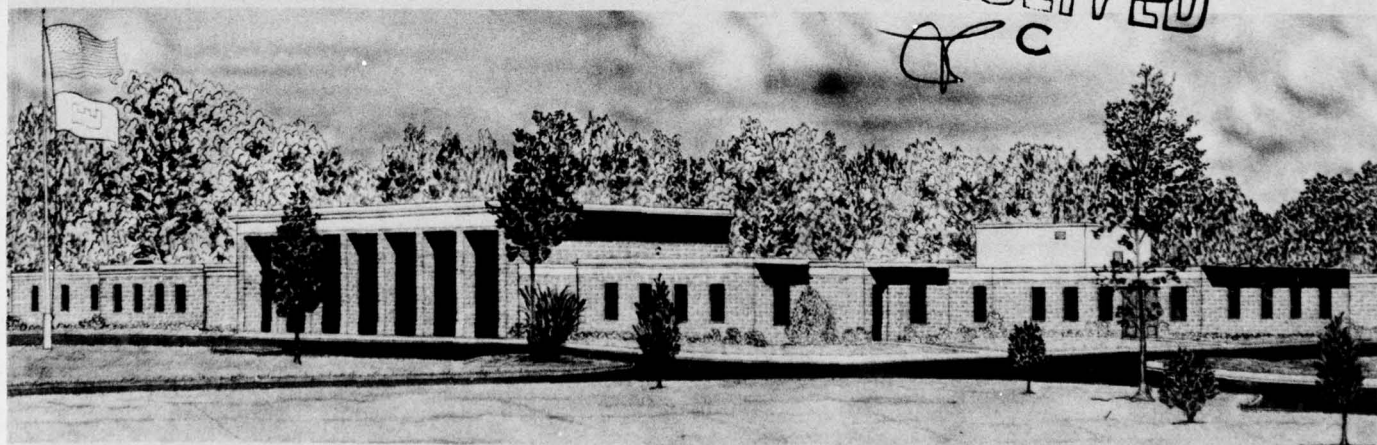
Richard H. Ledbetter

Soils and Pavements Laboratory  
U. S. Army Engineer Waterways Experiment Station  
P. O. Box 631, Vicksburg, Miss. 39180

September 1977

Final Report

Approved For Public Release; Distribution Unlimited



AD NO. \_\_\_\_\_  
DDC FILE COPY

Prepared for Assistant Secretary of the Army (R&D)  
Washington, D. C. 20314

Under Project No. 4A161101A91D

Destroy this report when no longer needed. Do not return  
it to the originator.

14 WES-TR-S-77-10

Unclassified

SECURITY CLASSIFICATION OF THIS PAGE (When Data Entered)

REPORT DOCUMENTATION PAGE		READ INSTRUCTIONS BEFORE COMPLETING FORM
1. REPORT NUMBER Technical Report S-77-10	2. GOVT ACCESSION NO.	3. RECIPIENT'S CATALOG NUMBER
4. TITLE (and Subtitle) GENERAL DEFORMATION (ELASTIC AND INELASTIC) AND STRESS DISTRIBUTION THEORY IN SOILS	5. TYPE OF REPORT & PERIOD COVERED Final report	6. PERFORMING ORG. REPORT NUMBER
7. AUTHOR(s) Richard H. Ledbetter	8. CONTRACT OR GRANT NUMBER(s)	
9. PERFORMING ORGANIZATION NAME AND ADDRESS U. S. Army Engineer Waterways Experiment Station Soils and Pavements Laboratory P. O. Box 631, Vicksburg, Miss. 39180	10. PROGRAM ELEMENT, PROJECT, TASK AREA & WORK UNIT NUMBERS Project No. 4A161101A91D	
11. CONTROLLING OFFICE NAME AND ADDRESS Assistant Secretary of the Army (R&D) Washington, D. C. 20310	12. REPORT DATE September 1977	13. NUMBER OF PAGES 118
14. MONITORING AGENCY NAME & ADDRESS (if different from Controlling Office)	15. SECURITY CLASS. (of this report) Unclassified	15a. DECLASSIFICATION/DOWNGRADING SCHEDULE
16. DISTRIBUTION STATEMENT (of this Report)  Approved for public release; distribution unlimited.		
17. DISTRIBUTION STATEMENT (of the abstract entered in Block 20, if different from Report)		
18. SUPPLEMENTARY NOTES		
19. KEY WORDS (Continue on reverse side if necessary and identify by block number) Cohesionless soils      Pavements Cohesive soils      Soils Elastic deformation      Static loads Inelastic behavior      Stress distribution Live loads      Vibratory loads		
20. ABSTRACT (Continue on reverse side if necessary and identify by block number) → A nonstrain-hardening general deformation theory that describes both elastic and inelastic behavior of soils, whether unbound or asphalt-bound, was developed. The theory circumvents the need for yield surfaces or yield stresses separating elastic and inelastic behavior, and it defines elastic plus inelastic behavior as they naturally and simultaneously occur. Soil behavior is unified by the theory being applicable to both cohesive and cohesionless soils. → one (Continued)		

DD FORM 1 JAN 73 1473

EDITION OF 1 NOV 65 IS OBSOLETE

Unclassified

SECURITY CLASSIFICATION OF THIS PAGE (When Data Entered)

0381004

Unclassified

SECURITY CLASSIFICATION OF THIS PAGE(When Data Entered)

20. ABSTRACT (Continued).

→ The theory is applicable to soils whether in a pavement structure or beneath a foundation and is applicable for static, moving, and vibratory loadings. Laboratory testing can establish the model and be directly applied to field behavior and vice versa. Soil stress distributions for field loading conditions can be derived from properties and requirements of the theory. Response to moving wheel loads for distributed and mixed traffic on a pavement structure can be completely simulated in laboratory tests based on the theory. Continuation of this research is being sponsored by the Department of Transportation, Transportation Systems Center. ↑

Unclassified

SECURITY CLASSIFICATION OF THIS PAGE(When Data Entered)

THE CONTENTS OF THIS REPORT ARE NOT TO BE  
USED FOR ADVERTISING, PUBLICATION, OR  
PROMOTIONAL PURPOSES. CITATION OF TRADE  
NAMES DOES NOT CONSTITUTE AN OFFICIAL EN-  
DORSEMENT OR APPROVAL OF THE USE OF SUCH  
COMMERCIAL PRODUCTS.

ACCESS	
NTS	on <input checked="" type="checkbox"/>
DOC	B.H. Section <input type="checkbox"/>
MANAGEMENT	<input type="checkbox"/>
15110117	
BY	
DISTRIBUTION/AVAILABILITY NOTES	
JAN 1971	
A	

## PREFACE

The investigation reported herein was conducted under Department of the Army Project No. 4A161101A91D, In-House Laboratory Independent Research (ILIR) Program, sponsored by the Assistant Secretary of the Army (R&D). The ILIR project was entitled "Development of Pseudoplastic Deformation Theory for Pavement-Soil System Behavior." Authorization for the study was granted by WESVB Disposition Form, dated 24 July 1975, subject: "In-House Laboratory Independent Research Program, FY 1976." The investigation was conducted during the period November 1975-September 1977 in the Soils and Pavements Laboratory (S&PL), U. S. Army Engineer Waterways Experiment Station (WES).

The laboratory tests were conducted by Dr. Frank C. Townsend of the Soils Research Facility, S&PL. Much valued advice and support concerning this investigation were given by Dr. Townsend. The study was conducted and this report prepared by Mr. Richard H. Ledbetter under the general supervision of Messrs. H. H. Ulery, Jr., Chief, Pavement Design Division, and J. P. Sale, Chief, S&PL.

Directors of WES during the investigation and preparation of this report were COL G. H. Hilt, CE, and COL J. L. Cannon, CE. Technical Director was Mr. F. R. Brown.

## CONTENTS

	<u>Page</u>
PREFACE . . . . .	2
CONVERSION FACTORS, U. S. CUSTOMARY TO METRIC (SI)	
UNITS OF MEASUREMENT . . . . .	4
PART I: INTRODUCTION . . . . .	5
Background . . . . .	5
Purpose . . . . .	6
Scope . . . . .	6
PART II: LOAD RESPONSE OF PAVEMENT STRUCTURES . . . . .	8
Relative Displacements and Motion . . . . .	8
Stresses . . . . .	37
PART III: DEVELOPMENT OF GENERAL DEFORMATION	
(ELASTIC AND INELASTIC) MODEL . . . . .	40
Stress Path Induced by a Moving Wheel . . . . .	42
Deformation Response to Stress Paths . . . . .	49
Laboratory Tests . . . . .	58
PART IV: GENERAL DEFORMATION MODEL APPLIED TO	
FIELD CONDITIONS . . . . .	94
Deformation Zones . . . . .	94
Stress Distribution . . . . .	99
Field Tests . . . . .	105
PART V: CONCLUSIONS AND RECOMMENDATIONS . . . . .	116
Conclusions . . . . .	116
Recommendations . . . . .	117
REFERENCES . . . . .	118

CONVERSION FACTORS, U. S. CUSTOMARY TO METRIC (SI)  
UNITS OF MEASUREMENT

U. S. customary units of measurement used in this report can be converted to metric (SI) units as follows:

<u>Multiply</u>	<u>By</u>	<u>To Obtain</u>
inches	25.4	millimetres
feet	0.3048	metres
cubic inches	$1.638706 \times 10^{-5}$	cubic metres
pounds (mass)	0.4535924	kilograms
kips (mass)	453.5924	kilograms
pounds (mass) per cubic foot	16.01846	kilograms per cubic metre
pounds (force)	4.448222	newtons
kips (force)	4448.222	newtons
pounds (force) per square inch	6894.757	pascals
degrees (angular)	0.01745329	radians

GENERAL DEFORMATION (ELASTIC AND INELASTIC)  
AND STRESS DISTRIBUTION THEORY IN SOILS

PART I: INTRODUCTION

Background

1. Present airfield pavement design procedures, whether empirically or theoretically based, cannot accurately predict the actual behavior and response of a pavement structure (the surface and foundation soils) to various loading conditions, including distributed and mixed traffic, and various material conditions. Therefore, there was a need to closely study and determine the internal behavior patterns and mechanisms of pavement structures. Actual internal behavior has not been accurately defined in the past, and to formulate a good theoretical pavement structure model, the internal behavior should be fairly accurately known and not assumed.

2. Field instrumentation measurements taken in pavement test sections since the 1940's<sup>1,2,3</sup> have shown large repetitive inelastic movements occurring. The repetitive inelastic movements are upward as well as downward and can be as large as the elastic movements, depending on the loading history. (The inelastic behavior is of a pseudoplastic nature and is defined in Part II.) Therefore, the inelastic movements are not negligible and are not of minor importance to the overall behavior of a pavement structure. In fact, this inelastic behavior in all probability may be the major controlling factor or mechanism for pavement performance and life. Inelastic behavior occurs in both flexible and rigid pavement structures<sup>3</sup> and may possibly be a common characteristic that links or ties together the performance of all pavement types.

3. Presently, all pavement structure design and/or behavior models are based on the mechanics of continuum solids invoking the theory of elasticity partially or entirely. Inelastic behavior is

assumed to be negligible or nonexistent. Rutting in pavement structures is recognized as being inelastic; however, most attempts to analyze or predict rutting are based on manipulations of elastic theory. In general, linear and nonlinear elastic models do not give good predictions of the measured elastic phase of behavior,<sup>4</sup> and the patterns can be distinctly different. Elastic models cannot predict or duplicate the measured repetitive inelastic phase of behavior. However, the author recognizes that manipulations of and correlations involving elastic constants can improve the qualitative agreement between elastic model predictions and actual measurements of the elastic behavior phase.

#### Purpose

4. This investigation was undertaken in an effort, to the extent possible within time and monetary constraints, to determine, study, and define the actual physical mechanisms that control and produce the real internal behavior of pavement structures subjected to various loading conditions. In addition, the purpose was to model and predict these behavior patterns and to develop the basic foundation for a theory of pavement structure behavior.

#### Scope

5. The internal behavior patterns, as determined from existing field instrumentation measurements, were investigated as deemed applicable from the posture of several methodologies of material behaviors in the realm of elasticity and plasticity. Internal behavior patterns were also investigated in consideration of the present state of knowledge of soil material behavior in laboratory testing.

6. The elastic and inelastic behavior patterns measured in pavement structures are not related to failure conditions and are not at or near a failure envelope or surface, such as the envelope in Mohr-Coulomb failure law. One of the central basic ideas of theories of

plasticity in continua is that, at any stage of loading, a yield condition or surface can be defined, which separates stress states that are reached elastically from those which are reached plastically. The behavior of the yield surface in stress space lies at the heart of plasticity theory. In the author's opinion, the major effort of current work dealing with plasticity in soils is concerned with establishing the proper yield surfaces--its shape, how and why it moves in stress space, and all the theoretical and mathematical ramifications attached to it. All current plasticity models for soils (see References 5-7, as a limited selection) are primarily strain hardening models with yield surfaces continuously moving outward. In the author's opinion, for soil there are no physically satisfying theoretical approaches for making a yield surface contract in these models.

7. Measured behavior in pavement structures requires a yield surface (if one exists) that can be continuously contracting and expanding. Also, measured behavior implies elastic and inelastic behavior occurring simultaneously and not elastic occurring prior to inelastic as would be required by a yield surface. In fact, some data imply that the inelastic component of behavior must fully occur before elastic response can fully occur. Based on the above discussions and in the author's belief, measured behavior data demand a more basic search of fundamental soil material behavior for explanations.

8. In consideration of measured behavior and of the current directions of plasticity, this study took the approach that a yield surface in stress space is not the central theme or key to inelastic behavior and is negligible or may even be nonexistent. The study also took the approach that behavior is governed or controlled by deformation rules or laws and not by stress laws, except at complete failure of the material.

## PART II: LOAD RESPONSE OF PAVEMENT STRUCTURES

9. This part of the report is mainly a summary of the studies of References 2, 3, and 8, and they should be consulted for complete details. A summary of the above-mentioned studies is believed to be essential to the unity and clarity of this report.

### Relative Displacements and Motion

10. Pavement structures (both flexible and rigid) respond to loading conditions with both elastic and inelastic behavior phases which occur simultaneously but which are in some respects independent of each other. The inelastic behavior is dependent on the following:

- a. Magnitude of load.
- b. Number of wheels.
- c. Pavement structure strength.
- d. Rate of load application.
- e. Loading sequence of offset position with respect to a point in the pavement structure.
- f. Temperature in temperature-dependent materials.
- g. Load history, which means the magnitude of the previous load and the offset position with respect to a point in the pavement structure.

Elastic behavior is not dependent on rate of load application or temperature unless the material is viscoelastic, such as asphalt. Also, elastic behavior is not dependent on loading sequence or load history.

11. Due to the nature of inelastic behavior coupled with the influence of random and distributed traffic or static loads acting over a pavement surface, a pavement structure is continuously pulsating upward, downward, and laterally. (Likened the behavior to that of a ball of putty being kneaded.) The pavement structure is plastic to the extent that it is stable at various levels to which it might be worked under loaded conditions, and it exhibits elastic behavior at each of its changing states of inelasticity with the elastic behavior operating from a floating reference.<sup>2</sup>

12. The inelastic behavior described above is of a pseudoplastic nature that can be characterized as follows:<sup>3</sup>

- a. If a material is loaded so that deformation is induced which does not completely recover and the material is never loaded again, the residual deformation is permanent (never recovers).
- b. However, if the material is loaded again in the same or another location, changes in the above-mentioned residual deformation may occur (e.g. changes in direction and/or magnitude) that may result in a new residual deformation that is again subject to this definition.

This inelastic behavior is not a permanent nonrecoverable displacement; it recovers as a function of load history.

13. Inelastic behavior does not appear to be directly related to measured total stress but is directly influenced by load history. (This suggests a deformation law.) For repeated loadings at the same point on a pavement structure not near failure, the inelastic response approaches zero after only a single or a few load applications, whereas the elastic response remains constant with load applications at the same point. However, upon loading at a different location, the inelastic phase is recovered and again becomes active at the previous point. Depending on load history and structure strength, the inelastic phase at a given point may require more than one load application for completion.

14. The elastic phase of behavior in a pavement structure is relatively constant,<sup>2,3</sup> except for viscoelastic materials. Also, the elastic behavior is symmetric, repetitive up to thousands of load repetitions, and independent of load history. The inelastic phase of behavior is symmetric and repetitive only for a symmetric or orderly load sequence. Random loading produces random and erratic inelastic behavior, but the elastic behavior is unaffected. Inelastic displacement may range from a magnitude of zero to many times the elastic response, depending on the load history and rate of load application.<sup>3</sup> As can be seen from the above discussion, a specific total (elastic plus inelastic) movement or displacement is impossible to define except for a single load application in the load history of

a pavement structure or for high rates of loading at which the inelastic response is essentially zero and only elastic response is occurring. At any point in time of the load history, the magnitude of total movement can range from the elastic response value to many times this value.

15. Inelastic behavior includes an increment of permanent displacement. For a full sequence of load applications (from an offset of no-load influence on one side of a point in a pavement structure to an offset of no-load influence on the opposite side), these increments of permanent displacement accumulate and can be determined.<sup>2</sup> However, according to the definition, this is the permanent displacement if and only if another load application or sequence is not applied causing an upward movement recovering part of it and changing the permanent to inelastic displacement.

16. The relationships of various vehicle loads, number of wheels, and structure behavioral patterns are not linear. In fact, they are very nonlinear, increasing with both load and number of wheels. Work concerned with the characteristics of the elastic phase of behavior can be found in References 2, 3, 4, 8, and 9. References 2, 4, and 9 include specific work with the principle of superposition and test section data.

17. This inelastic behavior has been noticed in pavement and soil tests since the 1940's. However, the erratic behavior as indicated by instruments has always been described as an ambiguous phenomenon due possibly to unstable (varying or changing zero) instrumentation or has simply been assumed to be meaningless.<sup>1</sup> The consequence of inelastic behavior has led to testing procedures in which the pavement or soil has been loaded at a point repeatedly (conditioning) in the belief that it causes instrument responses to be "stable" before recording the responses. By conditioning, the inelastic response, which can be erratic, can be made to approach zero. That is, after repeated load application at the same point, the response becomes entirely elastic. While this type conditioning temporarily eliminates the inelastic movements, it is not really representative of behavior

under actual traffic loading, since traffic is randomly distributed and approaches a normal distribution with time. Therefore, in actual use, the pavement never becomes conditioned and the inelastic displacements are continually occurring at varying magnitudes, depending upon the loading history.

18. Even as a pavement structure is being constructed, it is experiencing changing inelastic behavior at a point as compaction is being applied. Therefore, this inelastic phase of material behavior could also have importance in compaction studies. Testing procedures employing conditioning for field tests of pavement structures or soil masses and conditioning in laboratory testing can lead to erroneous conclusions that the materials are primarily elastic and strain hardening.

19. The Stockton Airfield pavement tests<sup>1</sup> noted a changing phenomenon occurring. In order to get rid of the phenomenon, conditioning was conducted by repeating traffic in a single wheel path until "stability" was reached, and then the instrument indications were recorded. Therefore, the reported measurements in Reference 1 are mainly elastic behavior, and the inelastic phase is unknown. Also, upward movement occurred when an adjacent wheel path was run. Instrumented homogeneous sand and clay tests at the U. S. Army Engineer Waterways Experiment Station (WES)<sup>10</sup> were conditioned tests by the fact that repetitive check tests were run prior to regular testing and the regular tests were repetitive. The measured responses were, therefore, primarily elastic. The AASHO Road Test<sup>11</sup> was conducted by conditioning. Repetitive wheel paths and plate tests were run, and the data were averaged. Therefore, the average values reflect primarily elastic response. The degree to which inelastic behavior affects the average values depends on the inelastic magnitude at a point in time and the number of repetitions.

20. The WES multiple-wheel heavy gear load (MWHGL) study<sup>2</sup> was nonconditioned pavement tests. A thorough analysis and study of the instrumentation data resulted in identification of a load- and position-dependent (load history), moving (floating) reference for each gage. This floating reference reflects the pavement structure real behavior

and is defined by the pavement rebound positions after each load application. The instruments and pavement structure, and thus the zero reference point, physically moved as the soil and pavement structure mass was kneaded by distributed traffic. WES deflection gages measured vertical motion in the MWHGL test section and were located at different depths with all anchored at a depth of 12 ft\* (inertial reference). These gages measured total pavement structure movement and not individual pavement element or layer movements (the latter require a noninertial reference). The floating reference was found to be active for the full instrumented depth of the structures.

21. The mechanism for the floating reference was not known at the time, and there was a possibility that it was a function of the instruments and not real behavior. Thorough instrument and electrical system checks were made, and they indicated the validity of the measurements. However, there were no other movement measuring instruments in the test section to verify the behavior. The elastic response derived from the floating reference was believed correct, even though the cause of the floating reference was unknown. This was based on characteristics of the elastic response.<sup>2,4,9</sup> Due to the above discussion, only the elastic responses were presented in the figures of Reference 2. However, based on the following discussions in this part, the inelastic responses can be obtained from the tabulated data in Reference 2.

22. In WES test section studies subsequent to the MWHGL study, movement measuring instruments (Bison coils) that operate on an entirely different principle from that of the WES deflection gage were used. Bison coil measurements verified the behavioral patterns indicated by the WES deflection gages in the MWHGL tests, and they also extended the knowledge of the character of the behavioral phases. The Bison coils gave internal responses (noninertial reference) for individual pavement structure elements or layers, whereas the WES deflection gages gave responses for the total pavement structure (inertial reference).

---

\* A table of factors for converting U. S. customary units of measurement to metric (SI) units is presented on page 3.

23. In addition to verifying the inelastic and elastic phases of behavior, the Bison coil responses to static load showed that elastic expansion or swell was occurring internally in the pavement structure elements with respect to gear-to-gage offset. Recorded vehicle traffic also showed that elastic expansion was occurring at lateral offset distances as well as in front of the wheels. This additional elastic phase of behavior needed to be verified not only in other pavement structures but with other types of instruments, and verification was obtained in the dynamic load tests.<sup>3,8</sup>

24. Additional information was also gained concerning the inelastic phase of behavior in the subsequent WES test section studies. Bison coils were recorded for a majority of the applied traffic, and these recordings showed that, for a given sequence of load applications with a given wheel configuration and load, the inelastic response had a specific form or pattern and was cyclic with the traffic pattern. The inelastic response was nearly constant under traffic until failure (as defined by WES for its test sections), at which point it increased drastically. However, the elastic response remained nearly constant even past failure. Similar behavior had also been observed in the static load tests of the MWHGL study before, during, and after traffic. Information concerning this behavior at failure, however, is very limited and not conclusive, and much more information needs to be obtained in this subject area. This trend at failure has been discussed because it concerns the inelastic behavior specifically, has been indicated by data, and could be very important in defining a mechanism or mechanisms of failure.

25. The aircraft dynamic loads study<sup>3,8</sup> further verified the measured behavior patterns indicated by the two different displacement instruments. Furthermore, verification concerning the elastic response was obtained with a third type of instrument (velocity gage) that has an entirely different operating principal. The aircraft dynamic loads study consisted of instrumented aircraft and pavement structures, both flexible and rigid. Pavement structure measurements mainly consisted

of relative displacements (vertical and lateral) of both the total structure and layers and of vertical stresses.

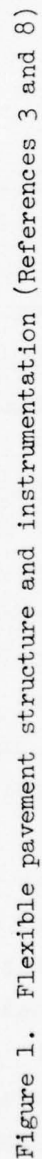
26. The following findings of the aircraft dynamic loads study are believed pertinent to this report:

- a. Elastic (including viscoelastic) and inelastic phases of material behavior were found acting in the displacements of both flexible and rigid nonconditioned pavements. The magnitude and direction of movement of the inelastic response were controlled by the gear-to-gage offset distance. Changes in direction of the inelastic response and upward movement at the various offsets and in the immediate gage vicinity occurred. However, the elastic and inelastic responses exhibited symmetry and repetition. Inelastic response was symmetric and repetitive for a given symmetric or orderly load sequence.
- b. In order to be able to fully interpret and analyze the nonconditioned pavement structure response data, the elastic and inelastic phases had to be separated (they occur simultaneously) and treated independently in the investigation of static and dynamic load test results. Instrument responses could not be completely analyzed unless the inelastic behavior was fully recognized and utilized.
- c. Two different types of displacement responses were identified as acting in both flexible and rigid pavements. The two types are total pavement structure response as assumed to be referenced to infinity (inertial reference) and individual pavement structure element response referenced internally to each element (noninertial reference). Each type of response exhibited both elastic and inelastic material behavioral phases.
- d. Bow waves in front of the wheels and elastic vertical expansions behind and adjacent to the wheels were found to occur within the structural elements (noninertial reference) of both pavement structures under moving aircraft.
- e. Test results showed inelastic behavior to be highly dependent on temperature, rate of load application, and load history (magnitude of load and lateral position of aircraft).
- f. Inelastic displacements larger than the elastic displacements were measured within the velocity range of static load to low-speed taxi.

- g. Test results showed elastic behavior to be almost constant for stiff pavement structures (rigid and low-temperature bituminous pavements) and the probable viscoelastic effects to be more pronounced at high temperatures in bituminous materials.
- h. The elastic and inelastic displacement behavioral phases directly associate the behavior of WES pavement test sections under simulated aircraft loads and wheel configurations and distributed (not conditioning) traffic to actual pavement behavior under actual aircraft operations.

27. The nature and behavior of the inelastic phase of movement have not been defined, fully described, or utilized in the past. It is real and is an important part of pavement structure response.<sup>3,8</sup> In analysis and interpretation of instrument response data from nonconditioned pavement structures, the inelastic behavior can be of a critical nature and should be considered. For random or distributed pavement loadings (which represent real loading conditions), instrument responses cannot be fully or correctly analyzed unless the inelastic behavior is fully recognized and utilized. In order to illustrate the interpretation and behavior of the elastic and inelastic phases in instrument responses, the following paragraphs present an actual data example. References 3 and 8 present in detail the methodologies used in the interpretation and analysis of data. Also, to clarify and illustrate the main points of the previous discussions, actual data figures are presented. These illustrations are presented at this point, because they should now have more significance after the previous main discussions.

28. The data interpretation example is from the data of Reference 3 for which the instrumented pavement structures were as shown in Figures 1 and 2. Consider the two series of static load tests shown in Figure 3. This figure represents the initial no-load reading, load on reading, and load off (rebound) reading of a WES deflection gage measuring between the 0- and 15-ft depths (inertial reference) of the flexible pavement structure during the warm weather tests in 1974. The data shown in Figure 3 were obtained by performing successive sequences of B-727 load application (load off, load on, load off) for both series of tests with the left (crosshatched) wheel of the dual-wheel main gear located



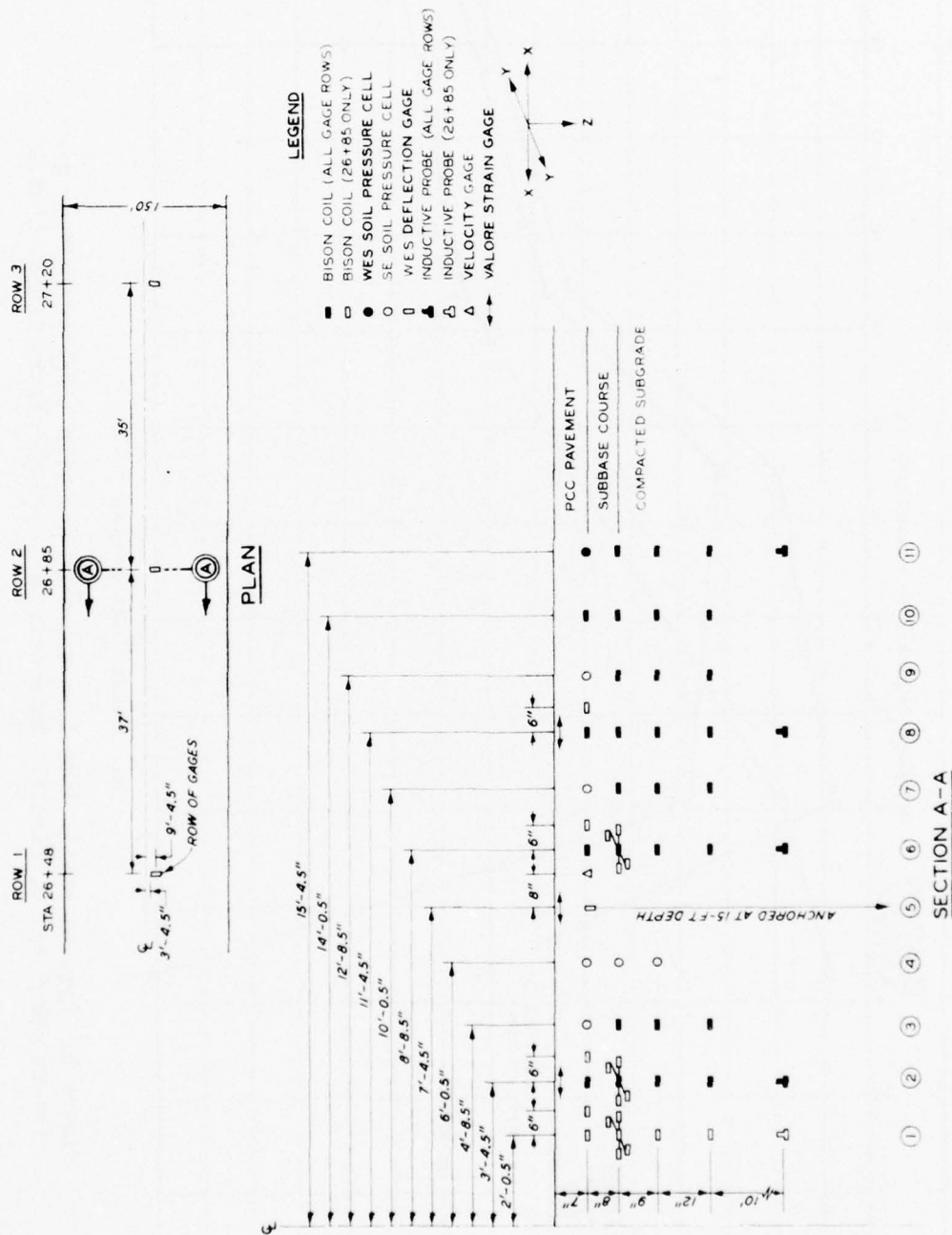
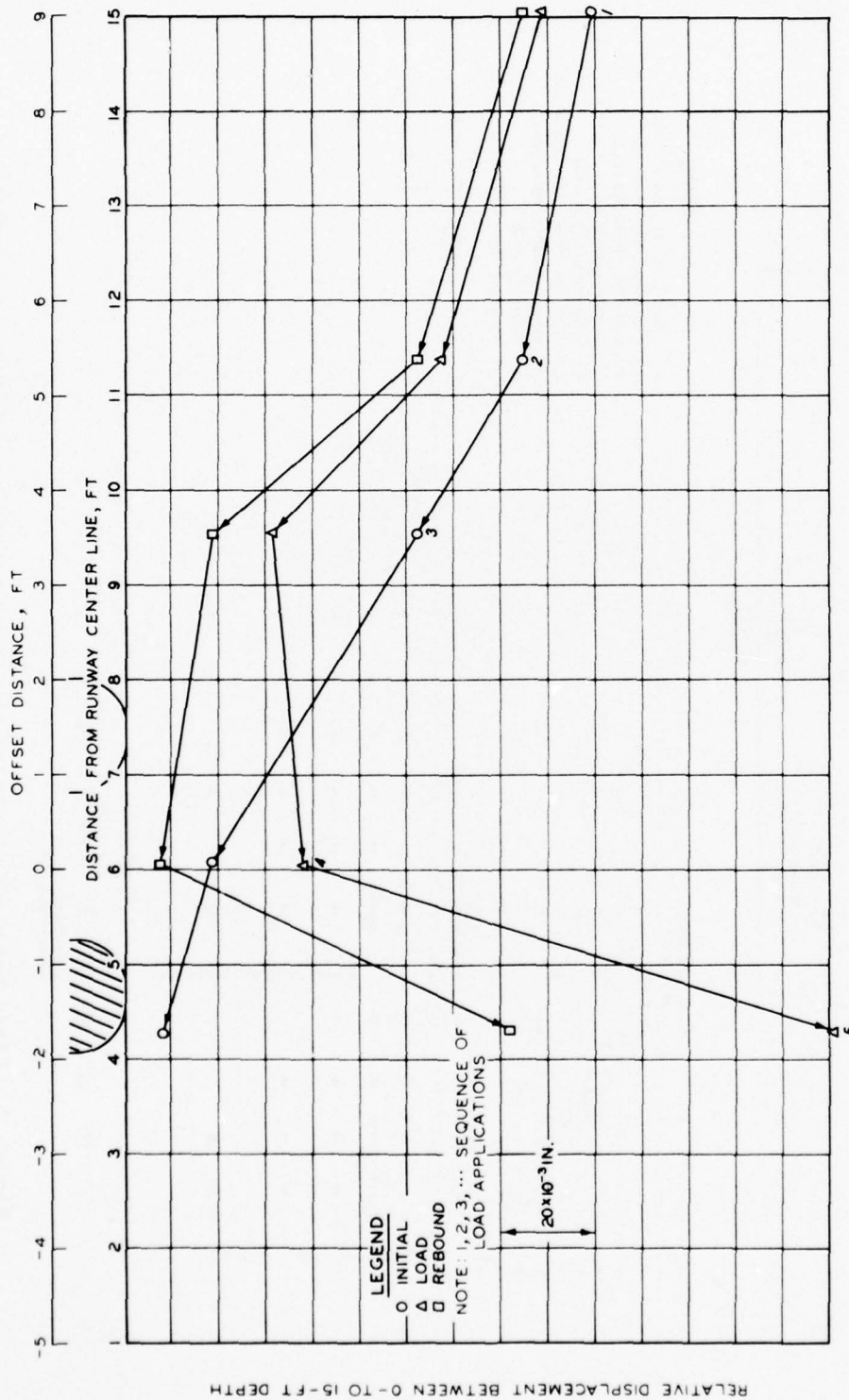
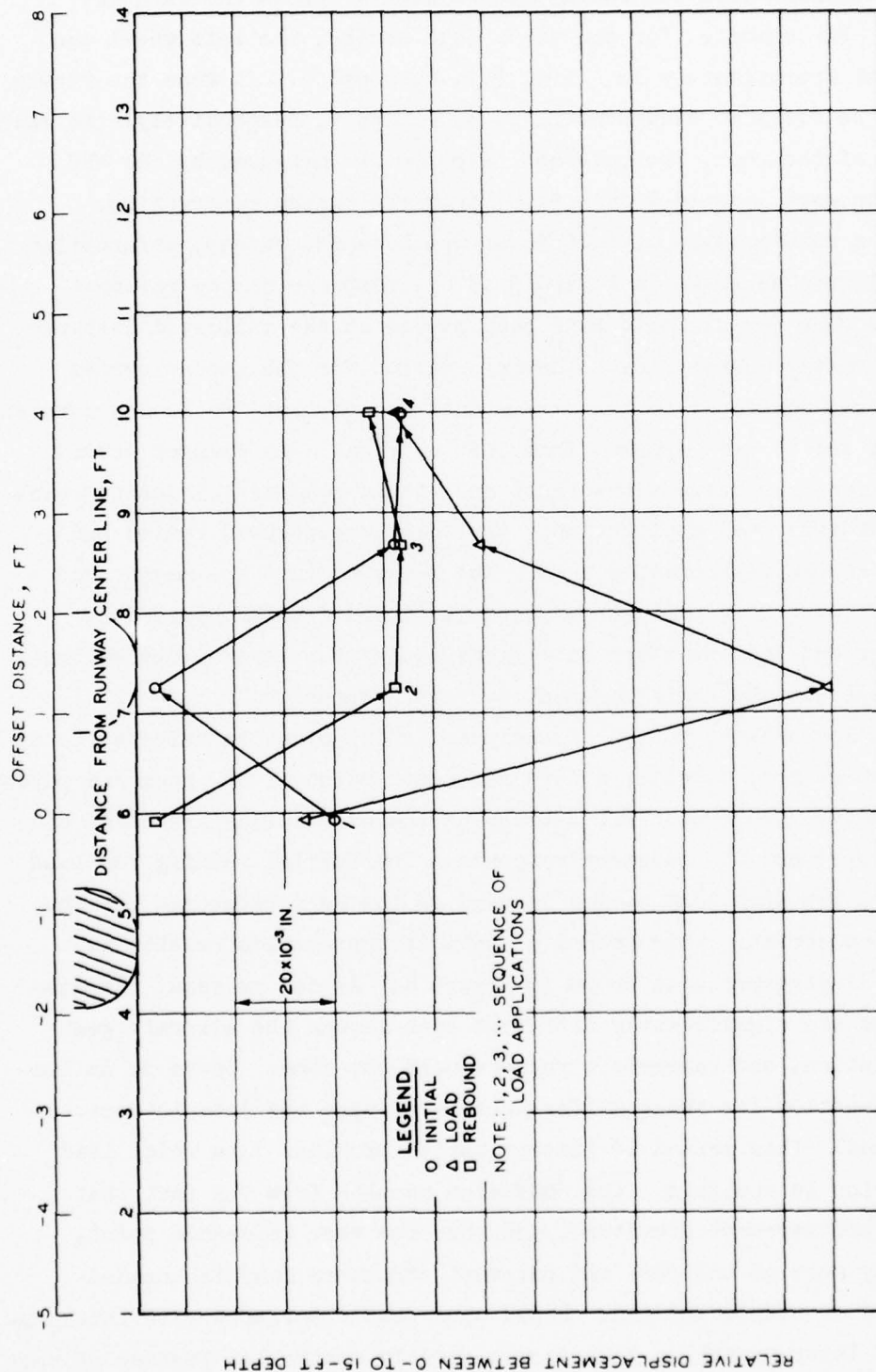


Figure 2. Rigid pavement structure and instrumentation (References 3 and 8)



a. First load series

Figure 3. Typical static load test measurements with a WES deflection gage (References 3 and 8, flexible pavement, 0- to 15-ft depth) (sheet 1 of 2)



b. Second load series

Figure 3 (sheet 2 of 2)

at the distances from the runway center line at which the data are plotted. For example, for the first load series, the left wheel was located at approximately 15, 11.3, 9.6, 6.1, and 4.2 ft from the runway center line for load sequences 1, 2, 3, 4, and 5, respectively. At each location of the gear, the pavement response was measured by the WES deflection gage located 7 ft 4.5 in. from the runway center line. Assuming a relationship of reciprocal displacement exists, information can be plotted as shown in Figure 3 as the response of the pavement structure when the aircraft main gear passes at the indicated distance from the runway center line. The information for the second series of tests was developed in the same manner except that the load sequences (1, 2, 3, and 4) were applied from left to right. An elapsed period of 1 day occurred between the first and second load series during which time 23 dynamic load applications (including creep-speed taxis) had occurred on the instrumented area. The behavior (not the magnitude) shown in Figure 3 is typical for both rigid and flexible pavement structures and for the Bison coil (measured across layers) and Valore strain gage (on the rigid pavement surface) responses.

29. For a first method of analysis, which might be referred to as a standard method, consider a zero reference point of the gage and pavement structure from which all subsequent loaded readings are taken and used to represent the pavement response. The initial reading for load sequence 1 for each load series is used as the zero reference for the entire load series. This method of data interpretation results in relative displacements as shown in Figure 4. As can be seen, the displacements are significantly different even though the aircraft gear load, location, and pavement structure were the same. There is no logical explanation for these differences based upon the data interpretation method. This method of interpretation provides data which lead to confusion in analysis. The confusion results from the fact that the gage and pavement structure, and thus the zero reference point, physically move as the soil and pavement structure mass is kneaded by traffic or static loading. Based upon past experience with interpretation of instrumentation data from carefully controlled testing of test

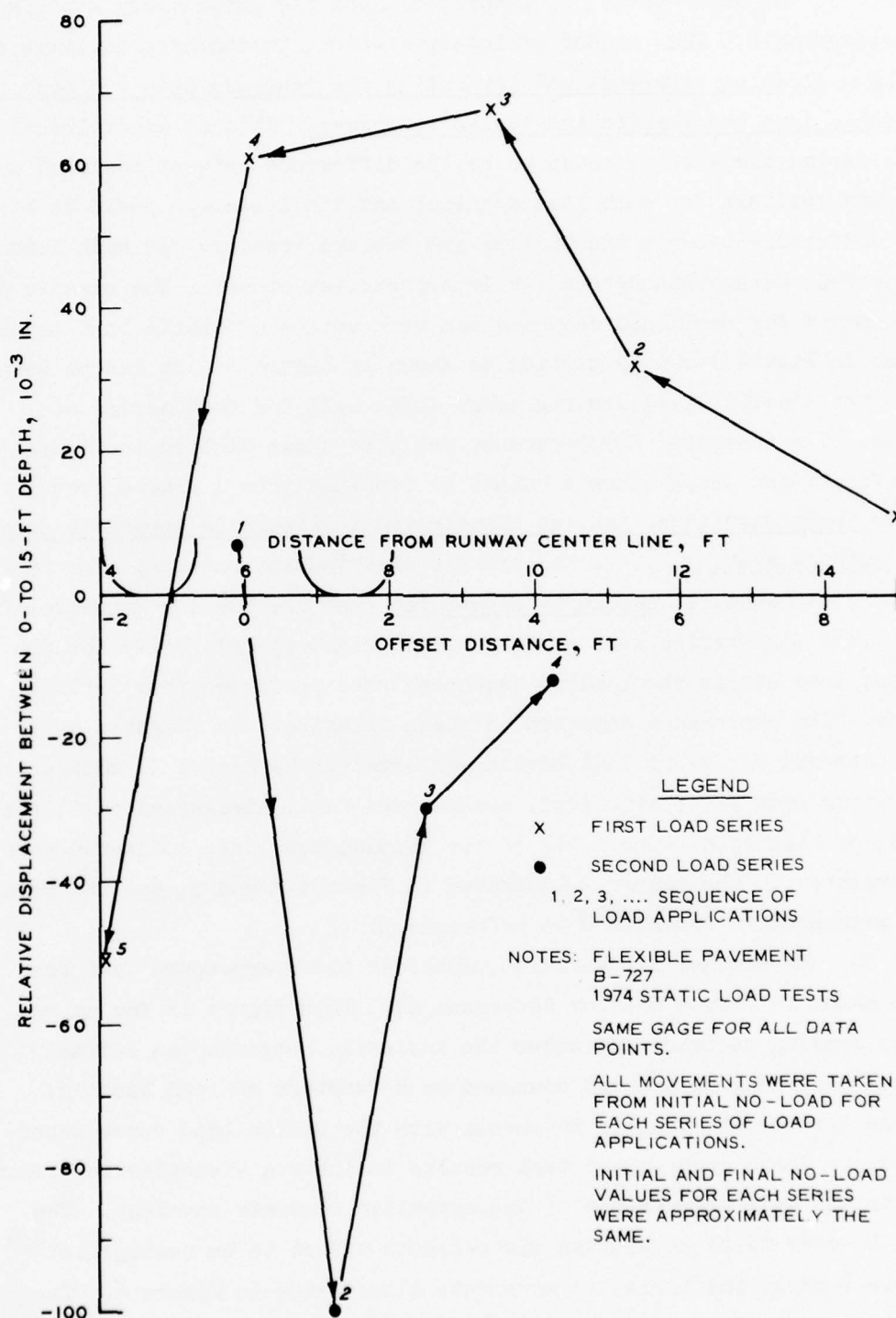


Figure 4. Relative displacements from a common reference (References 3 and 8)

sections, the data can be reinterpreted using the methodology explained in Reference 8. This method of interpretation, in summary, consists of using a floating reference and separating the response data for each load sequence into the elastic and inelastic phases. This is accomplished by considering the elastic phase to be the difference between the load and rebound readings for each load sequence and the inelastic phase to be the difference between the initial and rebound readings for each load sequence. Using this method for interpretation of data, the elastic displacements for each load sequence and both series of static load tests shown in Figure 3 can be plotted as shown in Figure 5. It can be seen that the elastic displacements agree quite well for both series of tests. The inelastic displacements are also shown plotted in Figure 5; however, these displacements cannot be combined into a single curve since their magnitudes are (as illustrated in Figure 5) dependent upon the loading history, i.e., the traffic distribution pattern. For the data illustrated, it should be remembered that the loading sequences for the first load series were performed from right to left while for the second load series the loading sequences were performed from left to right. The phenomenon depicted in these illustrations (Figures 3-5) was observed for every load series performed in Reference 3, whether the operating mode was static load, creep-speed taxi, high-speed taxi, rotation, or high-speed turn. All of the displacement data collected were interpreted in the manner illustrated in Figures 3 and 5, and the results are presented in Appendix B to Reference 3.

30. As another illustration, consider the creep-speed taxi test data shown in Figure 6 (from Reference 3). This figure is for an orderly loading sequence and shows the inelastic response (as defined above) occurring upward and downward as a function of load history. Figure 7 shows the elastic movements with the static load curve superimposed. These creep-speed taxi results indicate a viscoelastic effect due to the warm temperature of the asphaltic concrete pavement. The cold weather tests showed the viscoelastic effect to be negligible.<sup>3,8</sup> Figure 8 shows the inelastic movements illustrated in Figure 6. The elastic and inelastic responses actually occurred simultaneously but

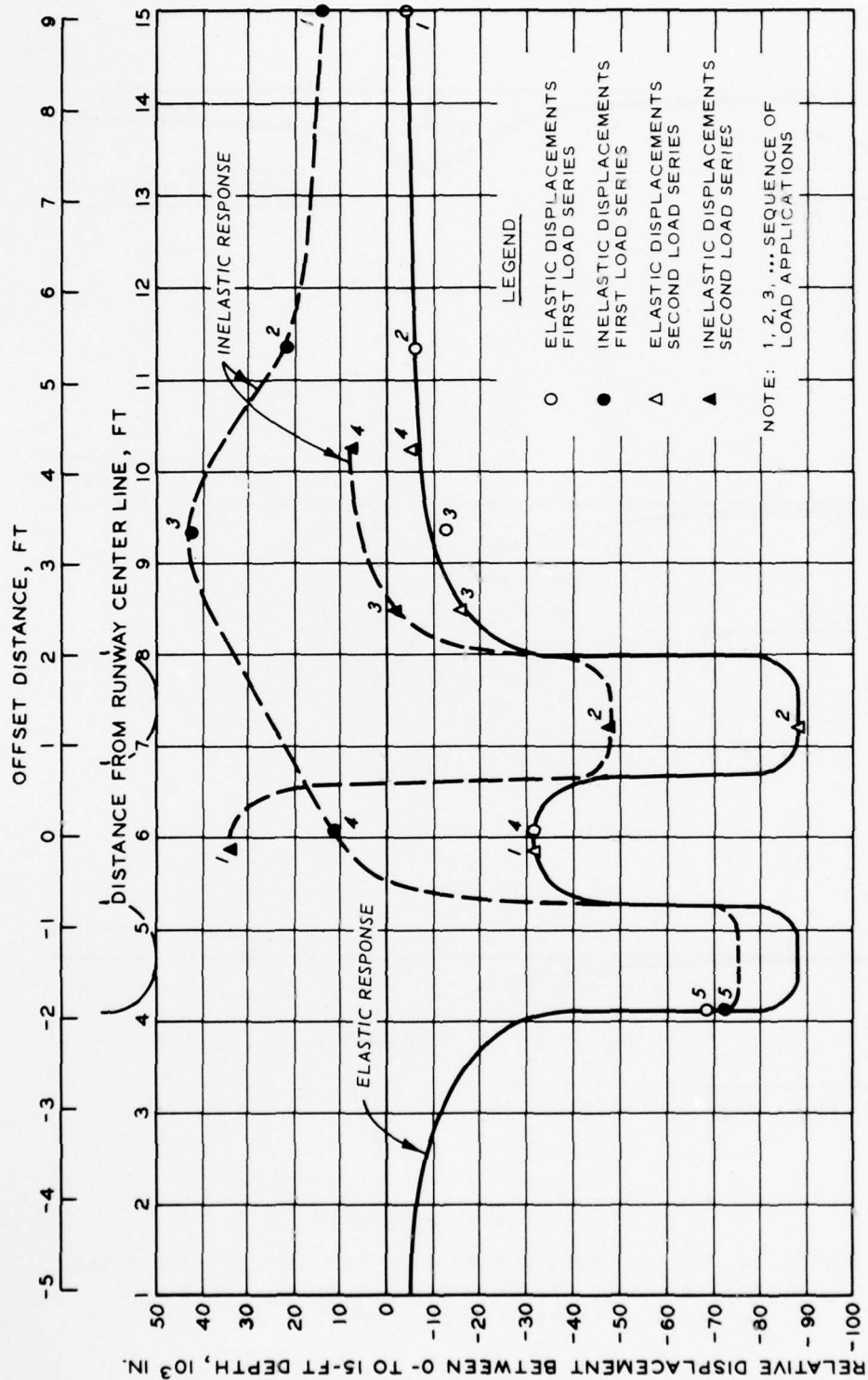
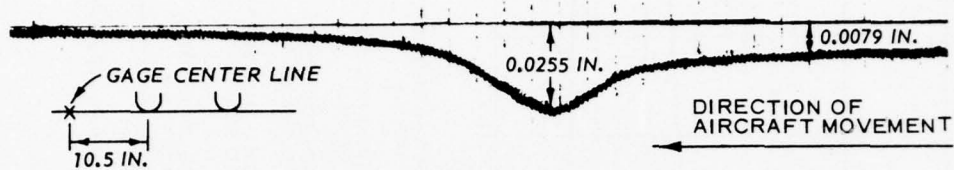
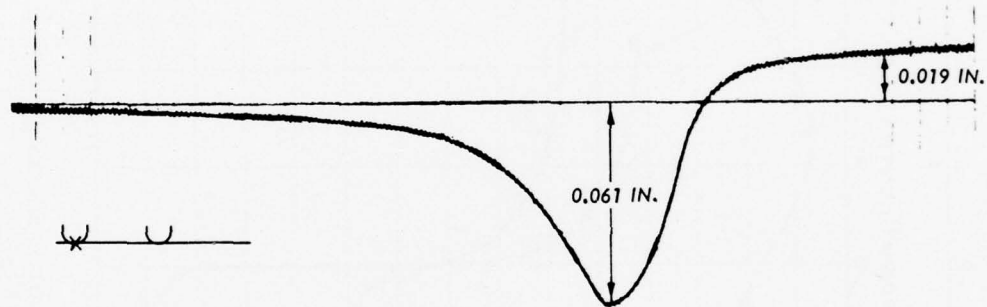


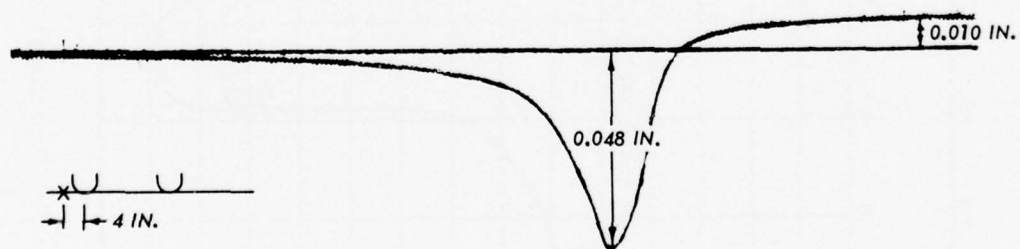
Figure 5. Typical static load test results measured with a WES deflection gage, from Figure 3



a. 10.5-in. offset

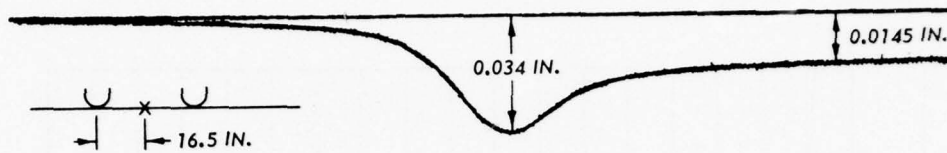


b. 0-in. offset

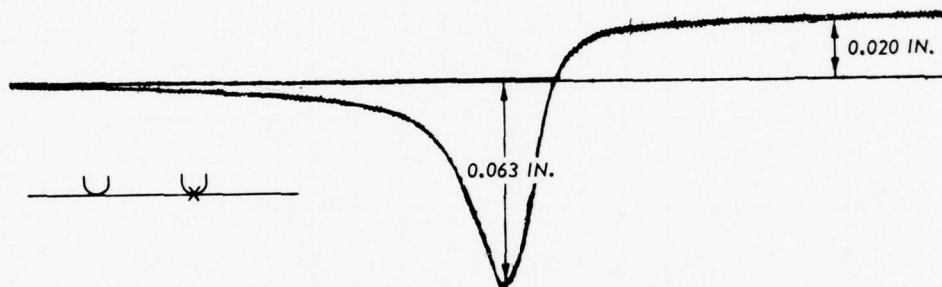


c. 4-in. offset

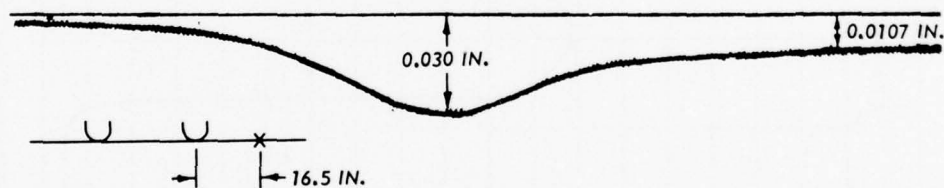
Figure 6. Typical analog recording for WES deflection gage (References 3 and 8, flexible pavement creep-speed taxi tests) (sheet 1 of 2)



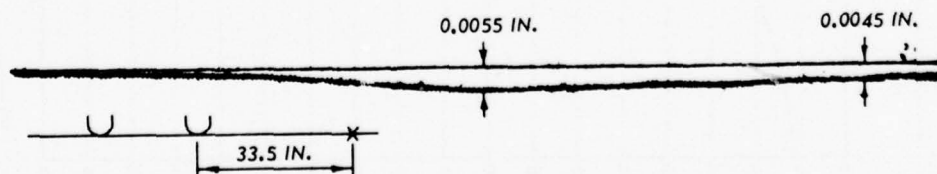
d. 16.5-in. offset



e. 0-in. offset



f. 16.5-in. offset



g. 33.5-in. offset

Figure 6 (sheet 2 of 2)

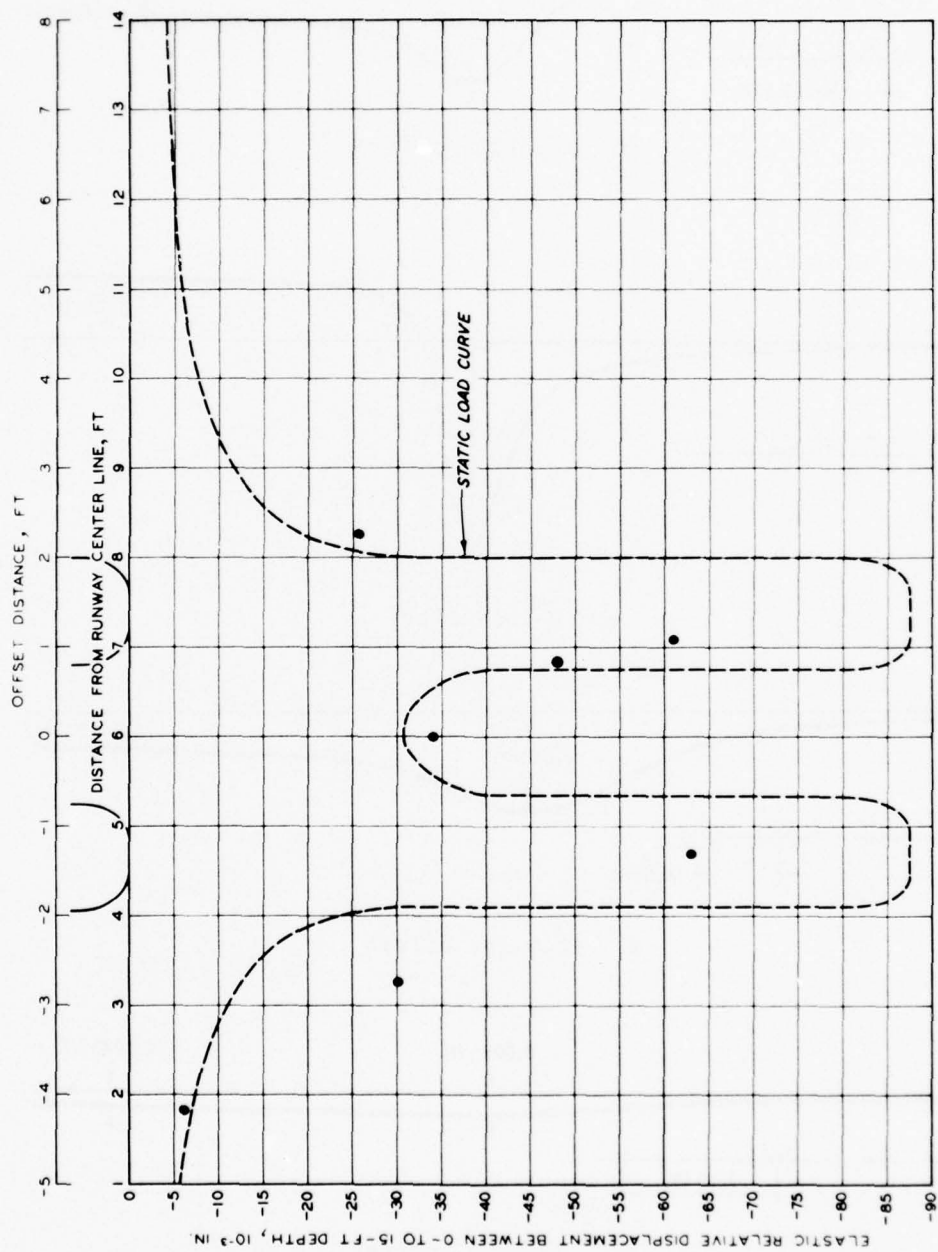


Figure 7. Typical creep-speed taxi test elastic relative displacements corresponding to Figure 6

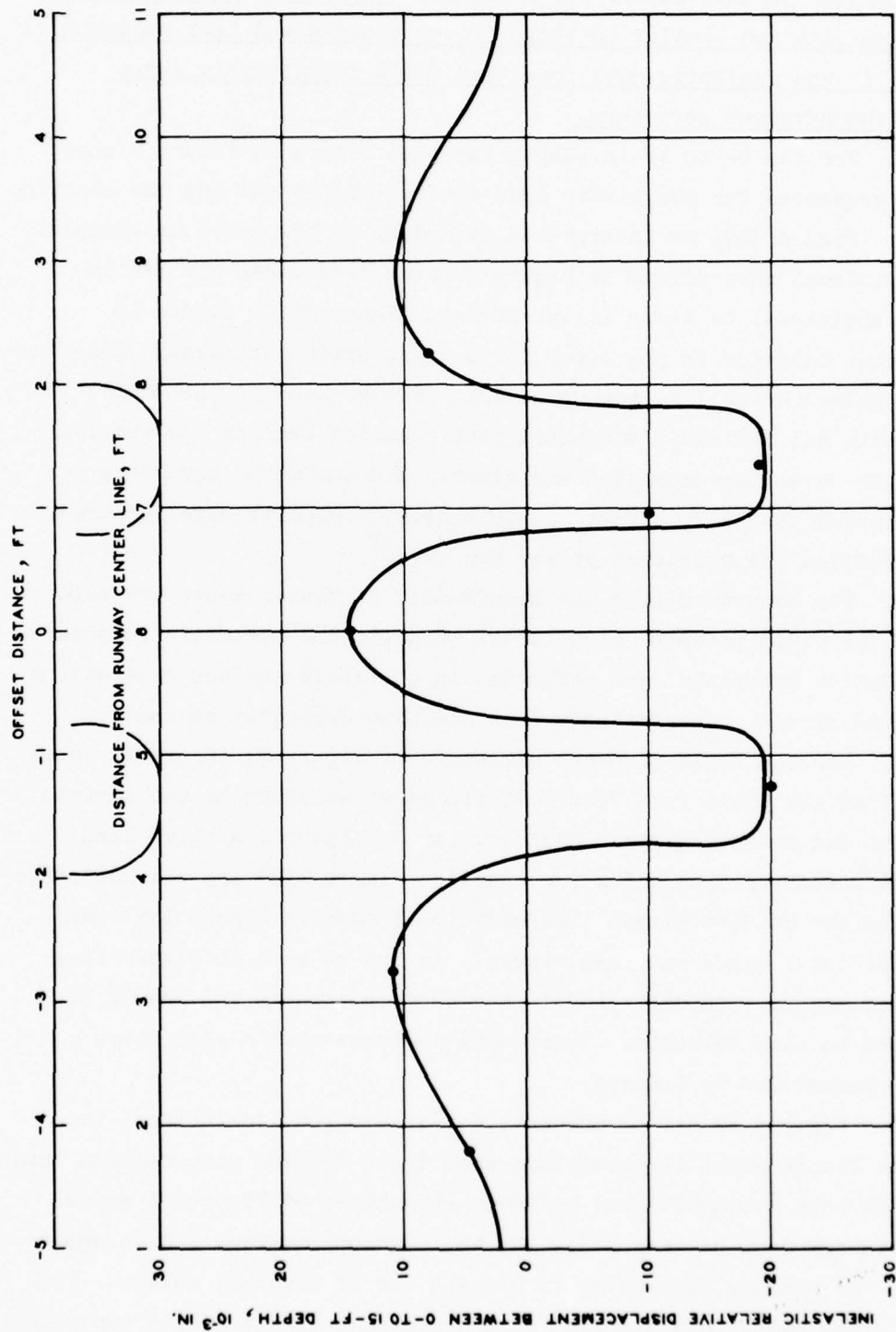


Figure 8. Inelastic wave form for creep-speed taxi tests illustrated in Figure 6

were separated in this manner for analysis. For any load sequence and rate of application similar to those in the creep-speed taxi sequence, Figure 6 is the inelastic wave form that would repetitively sweep through the pavement structure.

31. For the 9- to 18-in.-depth layer in Figure 1, Figure 9 shows loading sequences for two static load series (Figure 9a) and the elastic response (Figure 9b), as interpreted according to the previous example. (The additional data points in Figure 9b came from gages and static test in addition to those illustrated in Figure 9a.) Figure 10 illustrates behavior in the layer for a creep-speed taxi test. Figure 10a shows the uplift (bow wave) immediately ahead of the wheels and elastic and inelastic movements that occurred beneath the wheels. Figure 10b shows the expansion and elastic and inelastic movements that occurred at a 3-ft offset to the wheels. Velocity gage measurements verified the existence of the bow wave.<sup>3</sup>

32. The behaviors (not the magnitudes) presented above are also typical for rigid pavement structures. Elastic and inelastic responses in foundation materials<sup>3</sup> are reflected in the rigid surface by creating stress and strain concentrations that are also dependent on load history. For the rigid pavement structure of Figure 2, Figure 11 shows static load test data from Valore strain gages embedded in the surface of a slab and measuring horizontal strains.<sup>3</sup> Figure 11a shows load sequence movements from which the elastic (Figure 11b) and the inelastic responses can be determined. The additional data in Figure 11b came from additional gages and load tests.<sup>3</sup> As can be seen in Figure 11a, inelastic response is reflected in the surface strains and should be important to slab behavior. These data indicate that a slab stays bent or warped due to loading.

33. Figures 12 and 13 present, for static load conditions, the relative displacement distributions with depth for the gear maximum load points in both nonconditioned pavement structures of Figures 1 and 2. (The data are from Reference 3.) At the pavement surface and in upper layers, the maximum load point is beneath one of the dual wheels. The maximum load point then migrates with depth into the geometric centroid

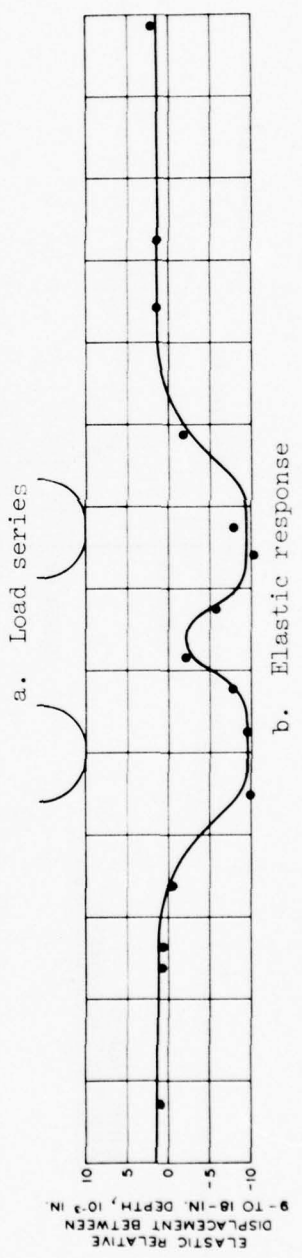
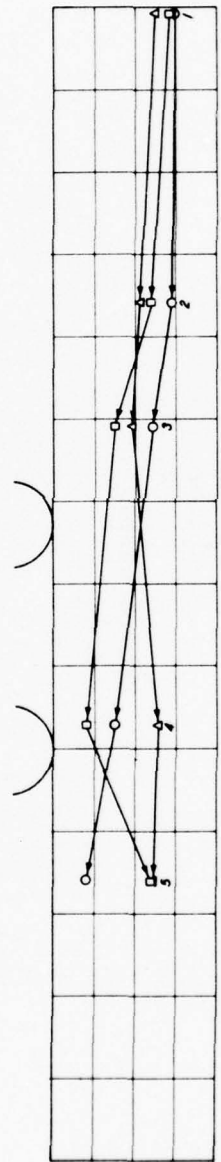
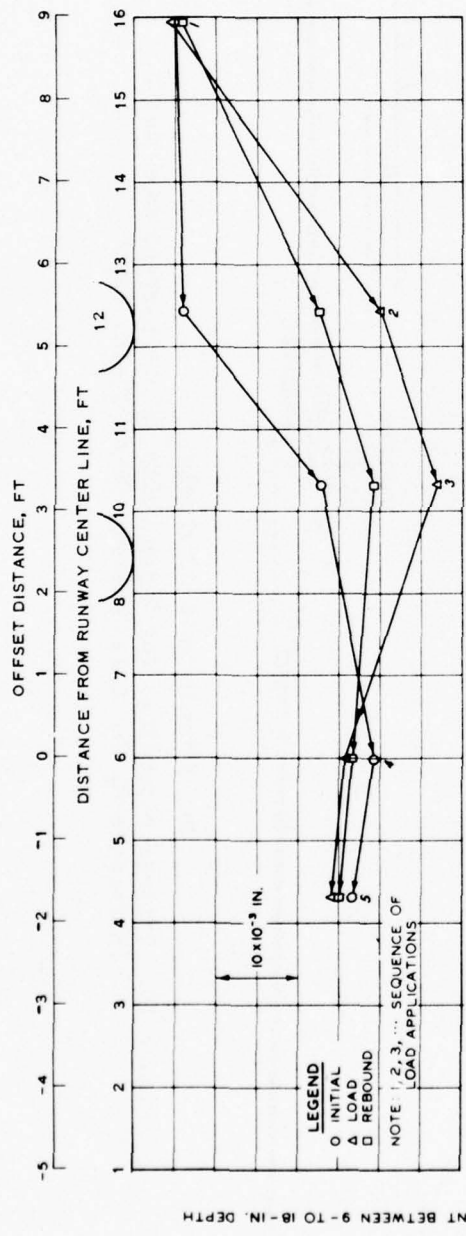
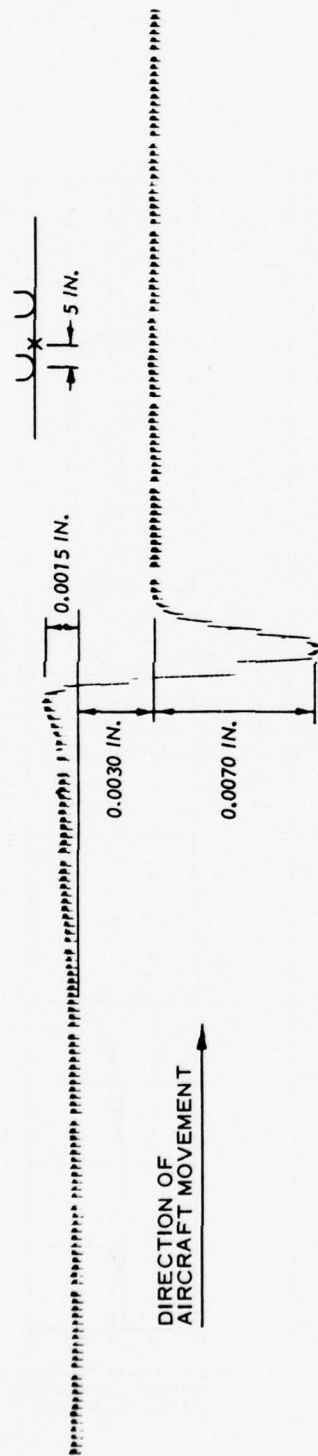
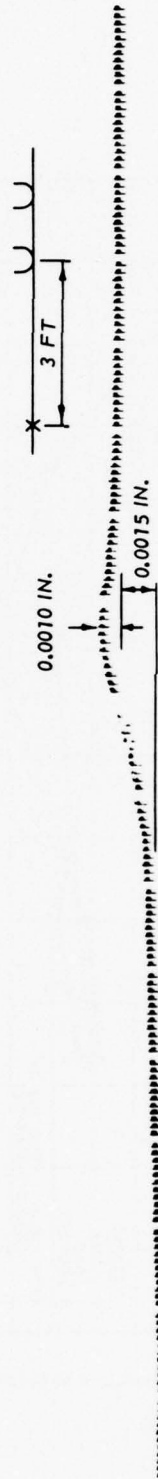


Figure 9. Typical static load test results measured with Bison coils (Reference 8, flexible pavement 9- to 18-in. depth)

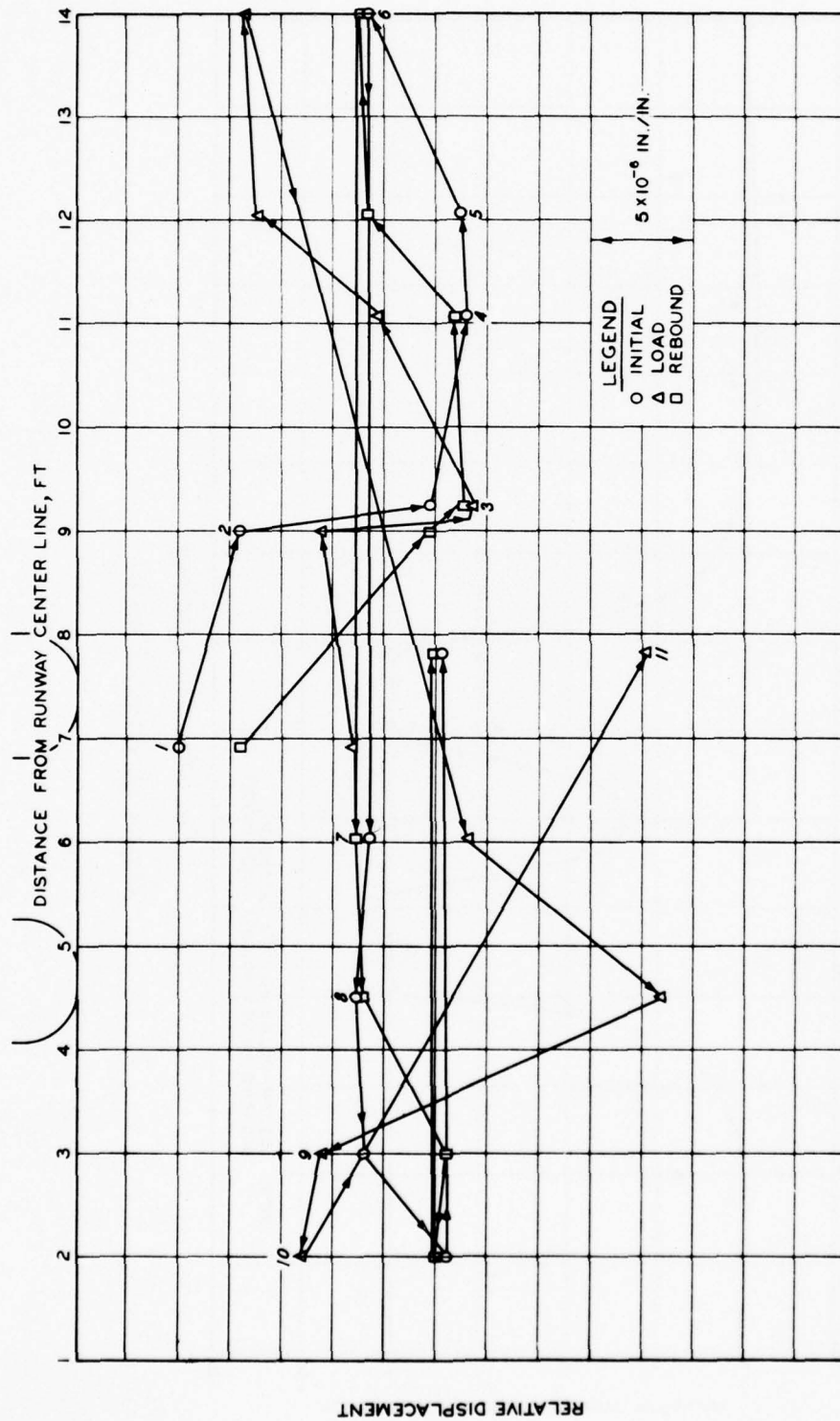


a. Beneath wheels



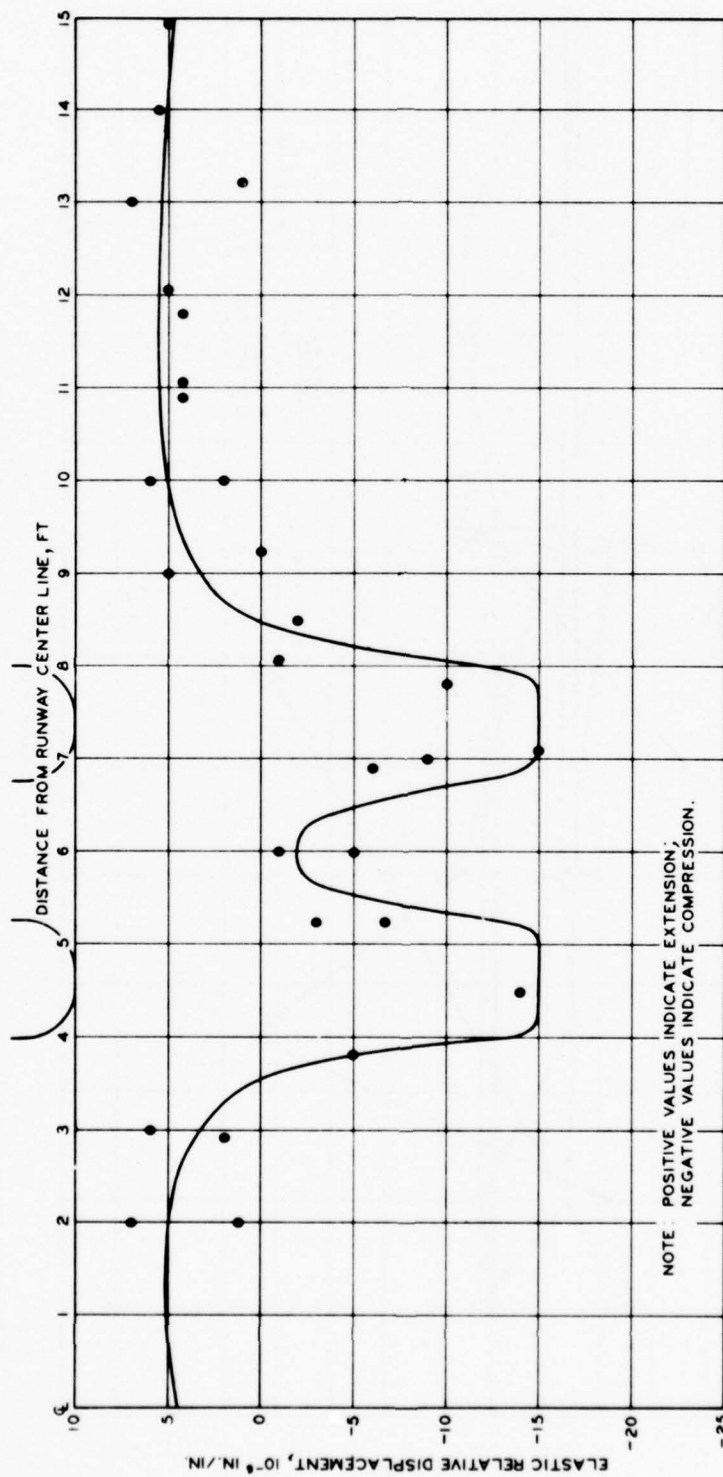
b. Beneath axis of wheels

Figure 10. Typical recordings for Bison coils in creep-speed taxi tests  
(Reference 8, flexible pavement, 9- to 18-in. depth)



a. Load series

Figure 11. Typical horizontal transverse deformation static load test results of Valore strain gages on the surface of a rigid pavement structure (Reference 8) (sheet 1 of 2)



b. Elastic response

Figure 11 (sheet 2 of 2)

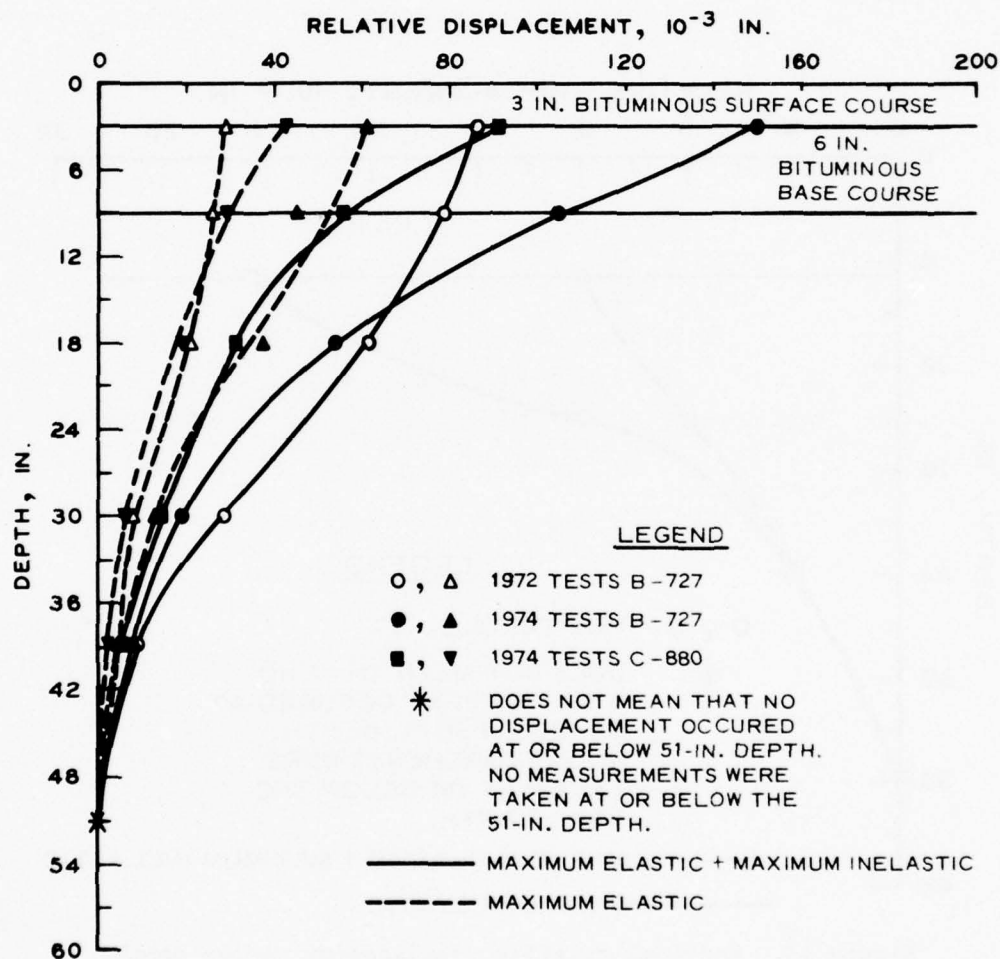


Figure 12. Vertical relative displacement versus depth, flexible pavement structure (Reference 3)

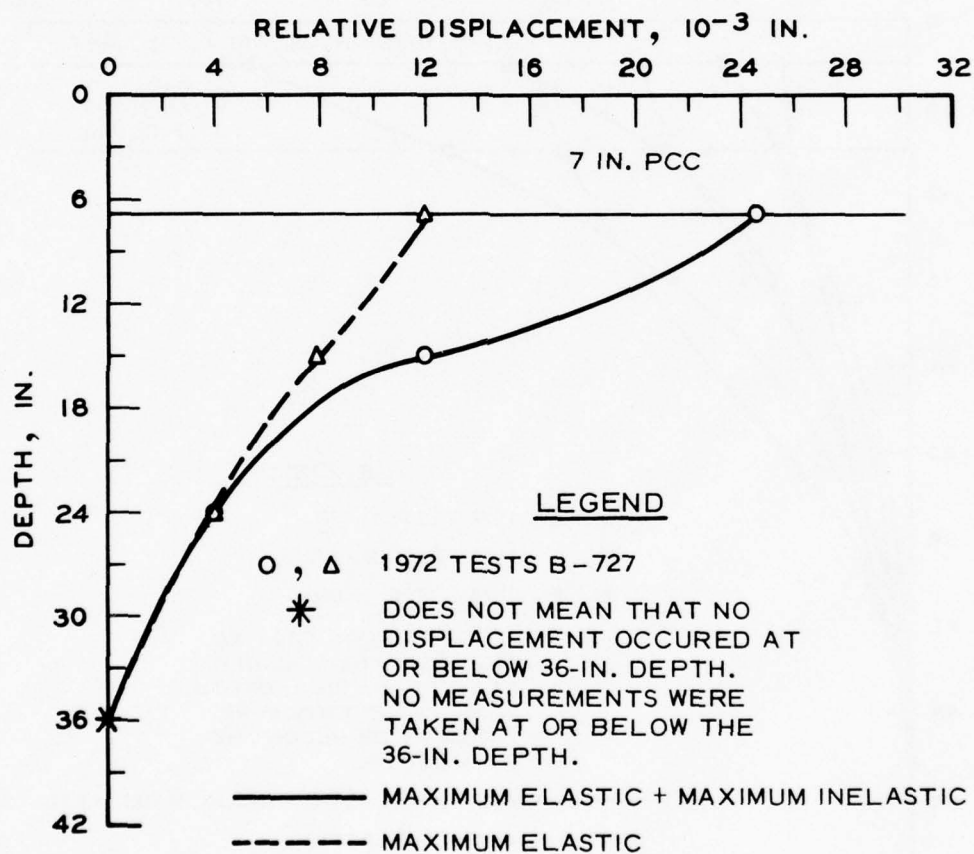


Figure 13. Vertical relative displacement versus depth, rigid pavement structure (Reference 3)

of the gear, which occurred at a depth of about 3 ft in the flexible pavement structure and at the bottom of the concrete slab in the rigid pavement structure.

34. The data in Figures 12 and 13 are accumulated vertical relative displacements measured within the pavement structure layers. To permit accumulating and plotting of the data, the Bison coils at the 51- and 36-in. depths of the flexible and rigid pavement structures, respectively, had to be assumed as zero reference points since no measurements were made below these depths. However, this assumption does not mean that no displacements occurred below the 51- and 36-in. depths. Figures 12 and 13 show the maximum elastic response that was measured. They also show the maximum elastic plus the maximum inelastic response that was measured, because the elastic and inelastic responses do occur simultaneously. For a single static load application of the aircraft on the pavements, the maximum elastic plus inelastic curves represent the maximum relative displacements that could be expected. However, depending on the load history, the actual displacement for any specific loading could be anywhere between the elastic and elastic plus inelastic curves. Load tests conducted after first conditioning the pavement structures would produce only the elastic response curves, and a significant displacement (inelastic) would not be obtained.

35. Figure 14 is a portion of a movement record that was recorded under distributed traffic of one main gear (at 30 kips per wheel) of the C-5A aircraft on a WES pavement test section. The test pavement structure consisted of 3 in. of asphaltic concrete over 21 in. of high quality crushed limestone with a heavy clay--4 CBR--subgrade. Figure 14 was recorded between the 9- to 24-in. depth (noninertial reference).

36. For the above test section, traffic was distributed by five traffic runs in a 16-ft wide lane. Traffic was applied by running an orderly series (1, 2, 3, 4, 5, 5, 4, 3, 3, 2, 1, and repeating) of the runs with a forward and reverse pass in each row. The traffic runs and whether forward or reverse pass are indicated in Figure 14.

37. Discernible in Figure 14 are the following:

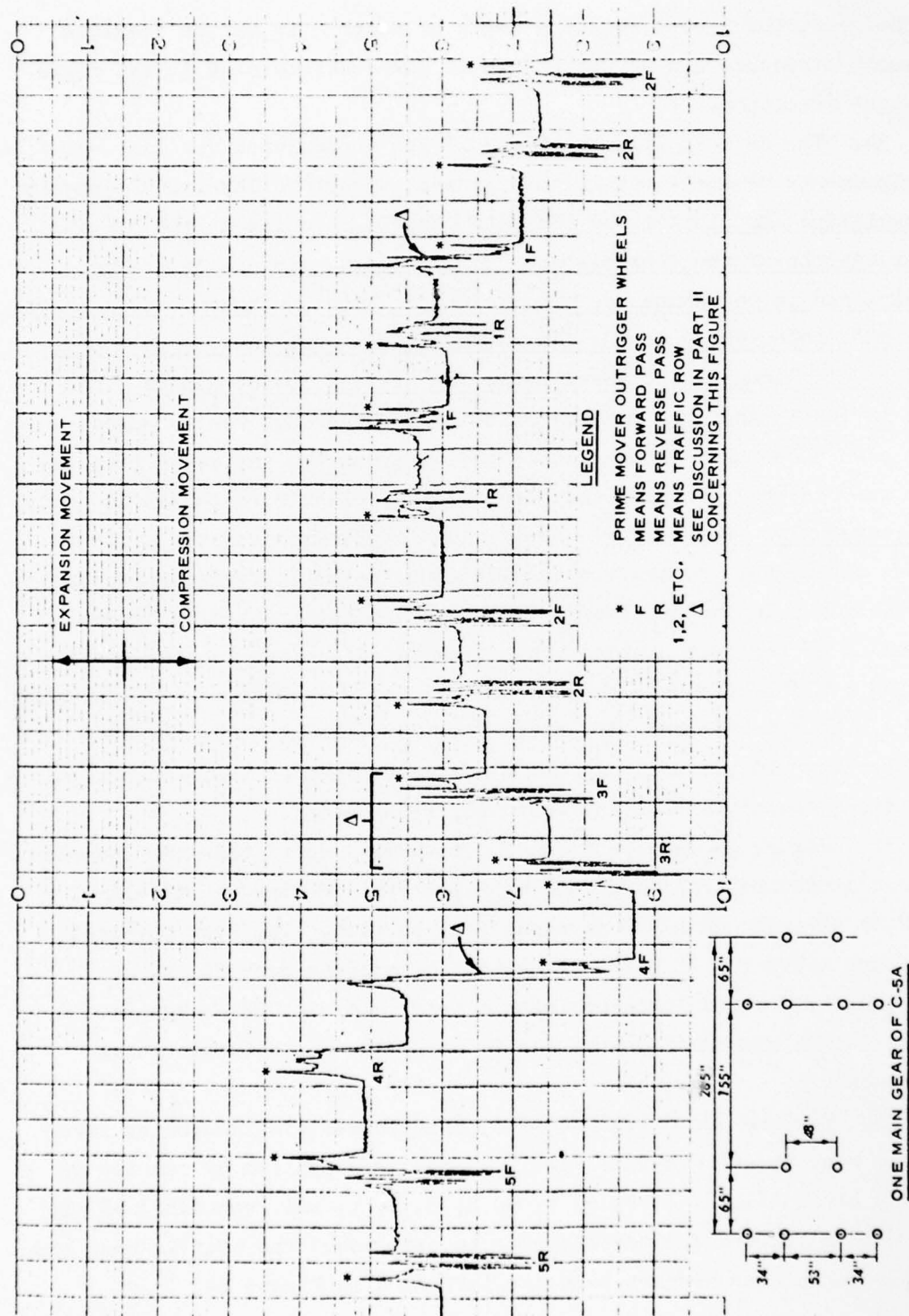


Figure 14. Typical portion of a movement record of Bison coils in crushed stone (9- to 24-in. depth)

- a. The changing states of inelastic equilibrium (floating reference) as a function of load history.
- b. The wave form that was repetitive with the orderly series of applied repetitive traffic.
- c. Expansion movement caused by the outrigger wheels of the prime mover, which pulled the aircraft gear load cart.
- d. Expansion movements (bow waves) in front of each group of wheels.
- e. Expansion movements adjacent to and behind the wheels.
- f. Compression movements beneath the wheels.
- g. For a given traffic row repeated in the series, the equality and repetitiveness of elastic movements independent of load history.
- h. Inelastic movements as large as and larger than elastic movements.

The recorded patterns can be reduced to elastic and inelastic movements as described previously.

38. Of importance in Figure 14 are the locations marked by a  $\Delta$ . The simultaneous occurrence of elastic and inelastic responses can be seen at these locations, with the inelastic dominating the behavior. Responses at these locations,  $\Delta$ , show that the inelastic phase of behavior must fully or approximately attain its state of equilibrium or stability before the simultaneous elastic phase of behavior can distinctly occur. In other words, elastic response can get lost in the total movement if inelastic equilibrium does not fully occur. The small changes in the floating reference between forward and reverse runs on a row were caused by the load cart not tracking in exactly the same wheel paths.

#### Stresses

39. Vertical stresses measured within pavement structures by pressure cells show no residual stresses to be acting. The load-induced vertical stresses are totally recovered, i.e. elastic (corresponding to the elastic phase of behavior), upon removal or passage of a load, and they are symmetric and repetitive. Any measured differences

between initial and final no-load responses are within the noise and variation levels of the instruments that have been used. The complex inelastic behavior previously described does not seem to induce residual stress; therefore, the pressure cells apparently are carried with or ride within the pulsating structures.

40. This behavior has been verified by two entirely different types of pressure cells. In the tests of Reference 2, WES soil pressure cells were used. These cells are 6 in. in diameter, 1 in. thick, and have a mercury- or oil-filled cavity between the faceplate and strain-gaged diaphragm. Stresses acting on the faceplate are averaged and transmitted by the liquid to the active diaphragm. The WES soil pressure cell has an aspect ratio of 0.167.

41. In the tests of Reference 3, SE soil pressure cells were used. This pressure cell was also developed at WES for measurement of blast stresses in soil. The pressure cell is designed so that the soil stresses act directly on a semiconductor-gaged diaphragm rather than through a stress-averaging chamber. The SE soil pressure cells are 1 in. in diameter, 0.23 in. thick, and have an aspect ratio of 0.188.

42. Figure 15 shows a typical pressure cell response record for vertical stress. (The record is typical for response beneath wheels and at offset distances from wheels.) This record is for an SE soil pressure cell in the tests of Reference 3; however, it is also characteristic of WES soil pressure cells. Figure 15 was recorded at the bottom of the 9- to 18-in. depth layer of Figure 1 for a creep-speed taxi.

43. As should be obvious from the above discussions, inelastic displacement behavior is not directly related to or controlled by induced vertical stress. Induced vertical stress is not affected by load history. Vertical stress acts downward, but the inelastic vertical displacement can occur upward or downward depending only on load history.

DIRECTION OF  
AIRCRAFT MOVEMENT

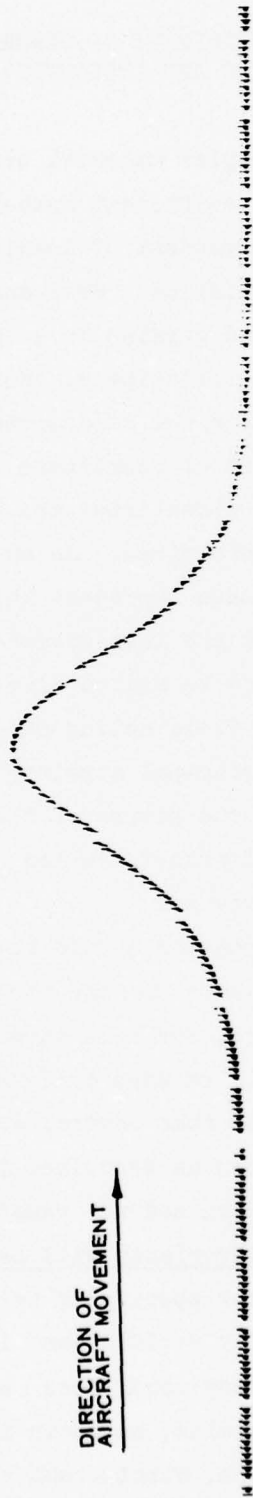
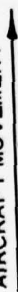


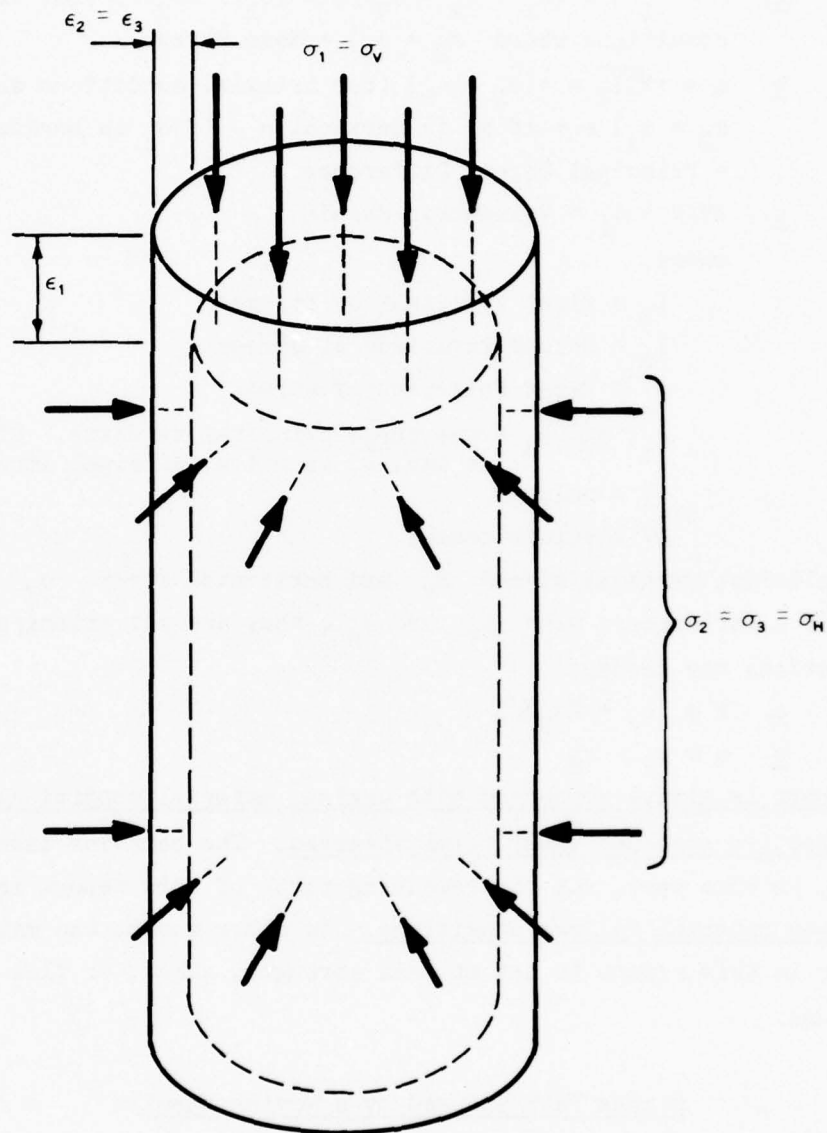
Figure 15. Typical recording for a WES SE soil pressure cell  
(References 3 and 8)

PART III: DEVELOPMENT OF GENERAL DEFORMATION  
(ELASTIC AND INELASTIC) MODEL

44. In the study of complex material behavior, the starting point should involve a minimum but sufficient number of parameters. Ideally, the parameters should be independent of loading and deformation conditions and be unique characteristics. Such characteristics do exist and are the principal stresses and strains in a body of material and also the invariants defined by the principals. For a stress field acting on or within a body, there is a set of components (three principal stresses) that are independent of coordinate systems. By knowing the principal stresses and their directions, the stress components on any plane within a body can be determined. As an example, Mohr's circles formed by the principal stresses represent the complete state of stress. Because of similarity between the laws governing both stress and strain, the characteristics of one may be stated directly for the other. Also, for a displacement or strain field acting on or within a body, there is a set of components (three principal strains) that are as stated above for stress. Coefficients of the powers of the principals are independent of coordinates and orthogonal transformation or rotation of axes; therefore, they are the invariants.

45. Complex material behavior should be defined by the principal stresses, strains, and invariants for the stress and displacement fields of a material body. Therefore, for this investigation, functions of the principles and invariants will be used to determine, study, and define the actual physical mechanisms that control and produce the internal behavior of pavement structures as described in Part II of this report.

46. For this investigation and the remainder of this report, functions of principals and invariants will be for triaxial test conditions. The specific reason for specifying triaxial test conditions is material behavior can be easily verified and investigated in laboratory triaxial testing. Triaxial test conditions result in only two principal stresses and two principal strains, as shown in Figure 16. Sign convention will be compressive stress, strain, and volume change as positive.



$\sigma_1, \sigma_2, \sigma_3$  PRINCIPAL STRESSES  
 $\epsilon_1, \epsilon_2, \epsilon_3$  PRINCIPAL STRAINS

Figure 16. A material under triaxial test conditions

47. The functions of the principals and invariants will be as follows (these are used in soil mechanics literature):

- a.  $P = I_1/3 = (\sigma_1 + \sigma_2 + \sigma_3)/3 = (\sigma_1 + 2\sigma_2)/3$  (for triaxial conditions where  $\sigma_2 = \sigma_3$ ) = Mean Stress.
- b.  $q = \pm\sqrt{3I_2} = \pm(\sigma_1 - \sigma_2)$  (for triaxial conditions where  $\sigma_2 = \sigma_3$ ) = + if  $\sigma_1$  is vertical = - if  $\sigma_1$  is horizontal = Principal Stress Difference
- c.  $\Delta V/V \approx J_1$  = Volumetric Strain

where

$I_1$  = first invariant of stress

$I_2$  = second invariant of stress

$J_1$  = first invariant of strain

$\sigma_1, \sigma_2, \sigma_3$  = the three principal stresses. Sigma with a bar,  $\bar{\sigma}$ , is not a principal stress

$V$  = volume

$\Delta V$  = volume change

For simplicity, vertical stress  $\sigma_V$  and horizontal stress  $\sigma_H$  will be used. If a bar appears over  $\sigma_V$  or  $\sigma_H$ , they are not principals.

The functions now become:

a.  $P = (\sigma_V + 2\sigma_H)/3$

b.  $q = \sigma_V - \sigma_H$

This report is always concerned with drained material conditions such that effective stresses equal total stresses. The behavior described in Part II, in this part, and the remaining parts of this report is not at or near material failure conditions. In other words, the material behavior in this report is not at peak strength, shear, or flow conditions.

#### Stress Path Induced by a Moving Wheel

48. The total state of stress at a point in a body can be represented by Mohr's circles. However, the state of stress can also be represented by plotting a point (stress point) whose coordinates are  $P$  and  $q$ . A  $P$ - $q$  diagram presents a stress space. As the states of

stress on a body change, stress points can be plotted for each change. By connecting the stress points in the P-q space, a stress path is formed. This stress path represents the stress history that the body underwent due to the changing states of stress. Also, a stress path can be followed for laboratory testing. In the P-q stress space q is positive if the major principal plane (a principal plane is the plane upon which the principal stress acts and is normal to it) is inclined equal to or less than  $\pm 45^\circ$  to the horizontal. If q is negative, the major principal plane is inclined less than  $\pm 45^\circ$  to the vertical. Therefore, a stress path can also represent the rotation or changing of principal axes if they do so with changing stress states.

49. Consider, now, the stress states at a point in a pavement structure as the pavement structure is subjected to a moving wheel load. Let the initial in situ stress state be isotropic such that  $\sigma_V = \sigma_H$ , and the principal planes are vertical and horizontal. Horizontal stresses first start increasing as the wheel moves toward the point. As this occurs,  $\sigma_H$  becomes greater than  $\sigma_V$ , and the major principal plane is vertical. The wheel moves closer to the point, and  $\sigma_H$  continues to increase. However, vertical stress starts to increase, and the major principal plane starts to rotate. Prior to the wheel reaching the point,  $\sigma_H$  reaches a maximum rate of increase, the major principal plane still rotating. From this time until the wheel passes the point,  $\sigma_V$  is increasing at a faster rate than  $\sigma_H$  and becomes greater than  $\sigma_H$ . The major principal plane continues to rotate and becomes inclined less than  $45^\circ$  to the horizontal when  $\sigma_V$  becomes greater than  $\sigma_H$ . Vertical stress reaches a maximum when the point is beneath the wheel, and the major principal plane has rotated to the horizontal. As the wheel moves past the point,  $\sigma_V$  decreases at a faster rate than  $\sigma_H$ , and the major principal plane rotates off the horizontal. Vertical stress continues to decrease to less than  $\sigma_H$ , and the principal plane continues to rotate to less than  $45^\circ$  to the vertical when  $\sigma_H$  becomes greater than  $\sigma_V$ . As  $\sigma_H$  and  $\sigma_V$  continue to decrease, the major principal plane rotates to the vertical. When the point in the pavement structure no longer feels load influence, the point is back to in situ

stress state and the principal planes are once again vertical and horizontal. This paragraph has described the stress history at a point in a pavement structure subjected to a moving wheel load. (The author realizes the fact that there are major, intermediate, and minor principal stresses acting. However, consider that at the initial start (in situ) the intermediate and minor principals are probably equal and approximately equal to the major. As  $\sigma_H$  starts increasing, the major and intermediate are probably equal, and beneath the wheel the intermediate and minor are probably equal. This therefore results in the largest Mohr stress circle always being defined by  $\sigma_V$  and  $\sigma_H$  at the most important states of stress. Due to the changing stress states described above and to the behaviors described in Part II, the author believes that in situ (no load) conditions are at or near an isotropic stress state. This corresponds to  $K_o = \sigma_H/\sigma_V = 1$  .)

50. Now that the stress history for a point in a pavement structure has been described, it can obviously be portrayed by a stress path in a P-q stress space. For regions ahead of the wheel and from in situ conditions the path is in negative q space. A peak is reached in negative q space at the point where  $\sigma_V$  starts increasing faster than  $\sigma_H$  . The path turns at this point and goes toward positive q . At the point where  $\sigma_V = \sigma_H$  , q equals zero. When  $\sigma_V$  becomes greater than  $\sigma_H$  and beneath the wheel, the path is in positive q space. As the wheel passes the point, the path comes back toward negative q ., into negative q space, and back to in situ no-load state. The principal axes are rotating with the major principal plane less than  $45^\circ$  to the vertical in the negative q space, equal to  $45^\circ$  when q equals zero, and less than  $45^\circ$  to the horizontal in the positive q space. Thus, stress history and rotation of principal axes in a pavement structure or soil mass can be defined in a P-q stress space.

51. Figure 17 shows a stress path such as described above. Points in the figure are defined as follows:

- a. At point A (in situ stress state),  $\sigma_V = \sigma_H$  equals isotropic conditions.
- b. At point B,  $\sigma_V$  starts increasing faster than  $\sigma_H$  .

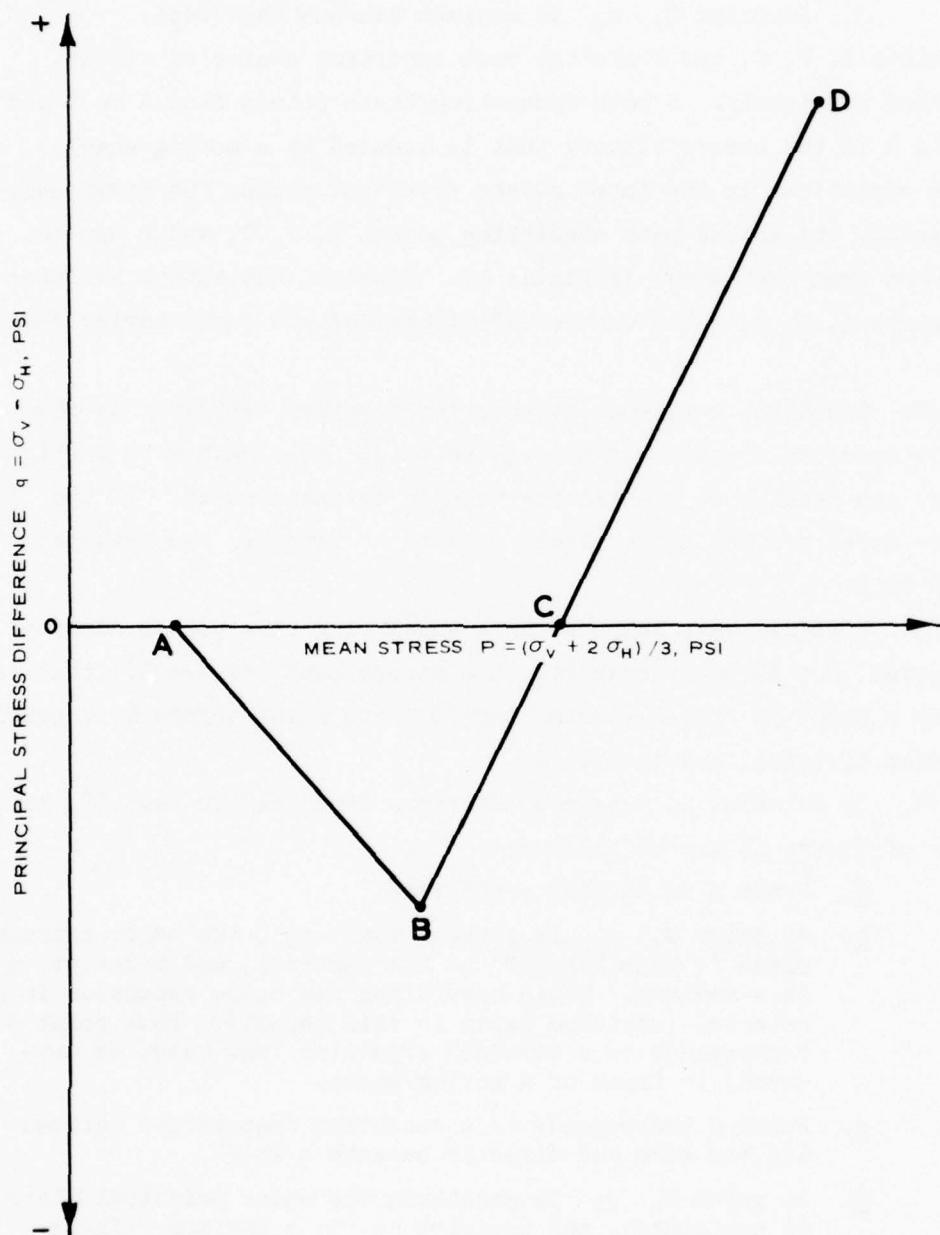


Figure 17. P-q stress space for a moving wheel load

c. At point C,  $\sigma_V = \sigma_H$  (path crosses through an isotropic stress point).

d. At point D,  $\sigma_V$  is maximum beneath the wheel.

The points A, B, C, and D are the most important states of stress, described previously. A path connecting these points from A to D and back to A is the stress history that is induced by a moving wheel. Due to variations in the intermediate principal stress (as previously discussed), the actual path connecting points A, B, C, and D may be different from that shown in Figure 17. However, the author believes the points A, B, C, and D can be definitely defined for a moving wheel load.

52. Consider, now, what happens for a parked vehicle. As the vehicle moves to a point and stops, the point feels path A to D (Figure 17) and remains at D until the vehicle is again moved. If the vehicle moves off the point either forward or reverse, the path is from D to A.

53. Consider what happens for a wheel load that passes adjacent to a point, not directly over it. The stress path (Figure 17) that is felt at a point is from A to some intermediate point before D, depending on offset distance, and back to A.

54. In relation to measured behaviors described in Part II, the points of Figure 17 are as follows:

a. Point A is in situ conditions.

b. At point B,  $\sigma_H$  is greater than  $\sigma_V$ , the major principal plane is less than  $45^\circ$  to the vertical, and negative  $q$  is a maximum. These conditions can cause expansion in a material (verified later in this report). Thus point B corresponds to a vertical expansion (bow wave, as measured) in front of a moving wheel.

c. Point C corresponds to a condition that exists between the bow wave and directly beneath a wheel.

d. At point D,  $\sigma_V$  is greatest, the major principal plane is horizontal, and positive  $q$  is a maximum. These conditions (as are well known) cause compression in a material. Thus, point D corresponds to the vertical compression (as is measured) beneath a moving wheel.

e. Adjacent to a moving wheel, point B occurs and is measured as the vertical expansion (shown in Part II).

- f. As a moving wheel passes a point, the corresponding measured movements (Part II) can be seen as the path goes from D back to A. Measured stresses do return to the in situ no-load state with no residual stresses occurring (Part II).

Obviously, Figure 17 also applies to static load tests with a wheel which rolls up to a point and stops or to static and dynamic plate loads. The positive  $q$  space represents the stress states beneath the load, and the negative  $q$  space represents the stress states at offset distance points.

55. The stress path of Figure 17 can be easily conducted in triaxial laboratory tests. Thus, a moving wheel load can be fully simulated in a triaxial test by following the correct stress path from A to D and back to A. The moving wheel load can be simulated as either passing directly over a point or at various offset distances. Also, a distributed or random traffic pattern can be simulated by following various combinations of the path (such as A-B-A, A-B-C-B-A, A-B-C-D-C-B-A, and repeating). Mixed traffic, different loads, can be simulated by following one path and then following another path that is shifted in  $P$ - $q$  space due to the changed load.

56. The majority of soil testing and characterization in the past and the present has been and is conducted entirely in the positive  $q$  space. Figure 18 shows the most common load path (whether monotonic or repetitive loading) that is followed in anisotropic load tests whether confined or unconfined. This type load path, A-E, is used and assumed to characterize materials for moving load, dynamic load, and static load conditions. Characterizations and elastic theoretical solutions are based on this test path and are used for material behavior whether directly beneath a load or at offset distances from the load. Modulus values such as Young's modulus  $E$ , resilient modulus  $M_R$ , bulk modulus  $B$ , etc., are based on load paths similar to A-E.

57. Paths similar to Figure 18 are representative of conditions directly beneath a plate or footing subjected to static or dynamic loading. However, the path, A-E, is not representative of offset conditions adjacent to a plate or footing and certainly does not apply to

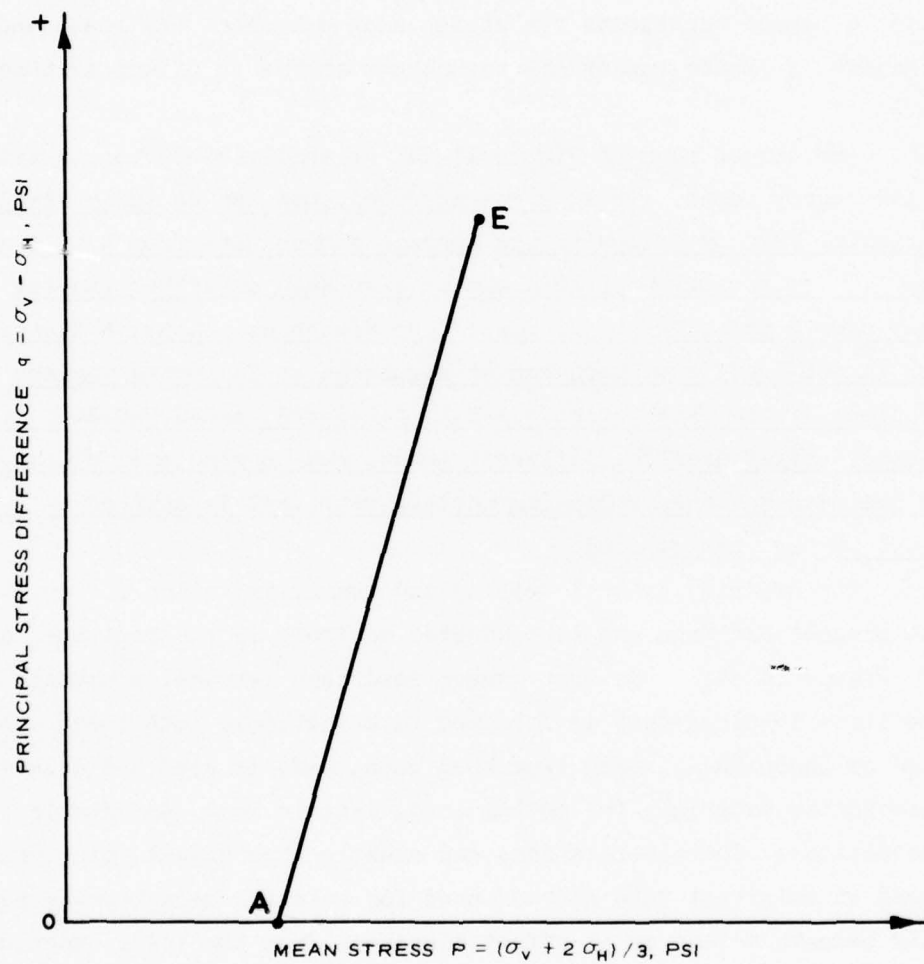


Figure 18. Most common soil testing P-q stress space

moving load conditions such as a wheel. Offset conditions should be characterized in the negative  $q$  space, which would result in different modulus values from the positive  $q$  space. Moving wheel load conditions cannot be characterized by a single modulus in either positive or negative  $q$  space but must consist of a multiple of moduli, as the path (totally or portions) in Figure 17 is traversed.

#### Deformation Response to Stress Paths

58. The  $P$ - $q$  stress space is formed by functions of the stress invariants; therefore, to characterize deformation and to be consistent with the stress space, consider the invariants of strain. Strain invariants are formed from the products of the principal strains,  $\epsilon_1$ ,  $\epsilon_2$ ,  $\epsilon_3$ . The first invariant of strain  $J_1$  equals  $\epsilon_1 + \epsilon_2 + \epsilon_3$  and is independent of coordinates and rotation of axes. For a given displacement or strain field,  $J_1$  has a unique value invariant with respect to order of the principal strains. As is obvious, a unique value of  $J_1$  can be obtained that is not directly related to the magnitude of any one or two principal strains.

59. As an example of the nature of the invariant  $J_1$ , consider a displacement field on a body with  $\epsilon_1$ ,  $\epsilon_2$ ,  $\epsilon_3$  taking on certain values under load conditions. Remove the displacement field, and  $J_1$  goes back to at-rest state. Apply the displacement field again, and let  $\epsilon_1$  take on a value different from above. The other principal strains  $\epsilon_2$  and  $\epsilon_3$  will therefore take on values such that the magnitude of  $J_1$  remains unchanged. In other words, a magnitude of  $J_1$  can be achieved for a given displacement field no matter how any one principal strain varies with load and deformation history. For a variation in one of the principal strains, the others will compensate so that  $J_1$  remains unchanged. This discussion of the nature and possible behavior concerning  $J_1$  is at least conceptually implicative of the deformation behavior described in Part II.

60. Consider, now, how the behavior of  $J_1$  in a material can be studied. In addition to the sum of principal strains,  $J_1$  is

approximately equal to volumetric strain  $\Delta V/V$  if the higher order products of strain terms are neglected. Thus,  $J_1$  can be studied and measured directly in a laboratory by simply measuring volumetric strain. Also, when principal strains are varying as described above,  $J_1$  can be determined and studied much more simply by the  $\Delta V/V$  behavior.

61. Consider the known behavior of drained soil samples in laboratory testing. As a sample is compressively loaded, unloaded, reloaded, unloaded, reloaded, etc., to larger loads, the volume decreases under load and expands with unload. The behavior can be broken down into elastic phase with unload, inelastic phase as the difference between load and unload, and elastic plus inelastic phases occurring simultaneously with loading. Observation of a family of laboratory-determined curves for such testing, whether isotropic ( $q = 0$ ) or anisotropic ( $q = \text{positive}$ ) loading, reveals that the different loading, reloading, and unloading curves have definite similarity of shape and behavior, each to its own type. Also, in repetitive loading to the same load, the reload and unload volume changes become equal. The above type loading corresponds, in Figure 18, to moving along the  $P$  axis (isotropic) or following a path similar to A-E (anisotropic).

62. Laboratory tests, Reference 12, on two cohesive soils indicated that volume change versus  $P$  was approximately the same curve for anisotropically (positive  $q$ ) and isotropically consolidated specimens. This indicates that in some three-dimensional space there is a compression wall on which all compressive points lie whether isotropically or anisotropically loaded. Considering the possible existence of unique compression walls, there should probably exist unique expansion,  $\sigma_H > \sigma_V$  and negative  $q$ , walls. (Soil testing terminology for  $\sigma_H > \sigma_V$  tests is "extension." However, the author of this report prefers the term "expansion," because no external tensile forces are applied to a soil sample.)

63. In consideration of the known volume change characteristics of soils, a three-dimensional behavior model describing field-measured behavior patterns (Part II) for moving wheel loads can be conceptually established. The third dimension of the  $P$ - $q$  stress space should, at

least, be a function,  $\Delta V/V$ , of the first invariant of strain. Within the  $P-q - \Delta V/V$  model, there should be unique compression and expansion walls for both anisotropic and isotropic loading and unloading.

64. For regions ahead of and adjacent to a moving wheel or adjacent to a plate ( $\sigma_H > \sigma_V$ ), the states of stress are in the negative  $q$  space, peak at point B in Figure 17, and are on an expansion wall of  $\Delta V/V$ . Therefore, the measured field behavior is expansion (bow wave for in front of the wheel). Directly beneath the moving wheel or plate, the states of stress are in the positive  $q$  space, peak at point D in Figure 17, and are on a compression wall of  $\Delta V/V$ . The measured field behavior is, therefore, compression. At a point in a pavement structure and with the passage of a wheel load directly over it, the states of deformation follow a path in the  $P-q - \Delta V/V$  model that goes first into expansion, crosses (at point C, Figure 17) into compression, goes back into expansion, and continues back to at-rest equilibrium. The deformation path is defined and controlled by the stress path.

65. For the passage of a wheel load or for a plate load test, the inelastic response at a point is upward or downward depending on magnitude and position of the previous load and on the magnitude and position of the present load. The  $P-q - \Delta V/V$  model is also dependent on load history in consideration of inelastic deformation. Inelastic volumetric strain (the difference between prior to load and unload  $\Delta V/V$ ) occurs in compression or expansion depending on the portion of a stress path (Figure 17) traversed and on what path and portion was previously traversed. For a moving-wheel stress path and due to the inelastic  $\Delta V/V$  that is continuously occurring, the unload, at-rest, volume is continuously changing and pulsating in compression and expansion, depending on load history. Thus, the pulsating at-rest volume is the floating or changing reference as compared to measured field tests (Part II).

66. Due to the invariant nature of volumetric strain,  $\Delta V/V$  has unique load and unload values independent of the initial or at-rest volume. However, the  $\Delta V/V$  values are dependent on the displacement field. In other words, the at-rest volume can be changing due to load history, but the  $\Delta V/V$  values for a given load condition are unique.

The uniqueness of the  $\Delta V/V$  terms for load and unload, therefore, causes unload (elastic) response to appear constant (in a given density range of a material and within the sensitivity of measuring instruments) for a given loading, and the at-rest unload volume to be changing.

67. From known soil behavior in laboratory compression tests, three  $\Delta V/V$  characteristic response curves (initial load, reload, unload) should exist. At first appearance, this is in violation of the invariant nature of  $\Delta V/V$ . However, consider that the load displacement field (thus  $\Delta V/V$ ) changes between initial load and reload due to the changing inelastic response. The displacement field associated with unload (elastic) does not change, and  $\Delta V/V$  unload is unique whether unloading from initial load or reload conditions. With continued reloading to a given load state, the displacement field continues to change (because of inelastic response) until the  $\Delta V/V$  end points for reload and unload are equal. At this point, inelastic response is zero and constant elastic response, therefore, occurs with repetitive loading. The above discussion has just described conditioning of material whether in a laboratory or in the field. Similar behavior, as described for compression, should occur for expansion. As discussed in Part II, inelastic response is a function of time and load history; therefore, the transition of initial load  $\Delta V/V$  to constant reload-unload  $\Delta V/V$  response is a function of time (rate of loading) and load history.

68. Based on the above discussion, there should exist initial load, unload, and initial reload  $\Delta V/V$  characteristic response curves, depending on load history. Also, because of the invariant nature of  $\Delta V/V$ , on some normalized basis there should exist only two characteristic response curves: load and unload. In other words, on a normalized comparison the initial load and reload  $\Delta V/V$  curves should be the same. (This will be shown in the next section.)

69. The  $P-q - \Delta V/V$  model represents a lumped parameter model. Factors (Poisson's ratio, cohesion, friction, etc.) that affect various behavior (such as strain components, strength, directional response to anisotropic loading, confinement, etc.) are lumped into one invariant parameter,  $\Delta V/V$ .

70. Figures 19 and 20 present three-dimensional views of the  $P$ - $q$  -  $\Delta V/V$  model. (Positive  $\Delta V/V$  is volume decrease.) For clarity the total model was separated into the load portions, Figure 19, and the unload portions, Figure 20. Projections onto the  $P$ - $\Delta V/V$  plane will be presented in the next section, and they will help Figures 19 and 20 become more perceptible. Also for clarity, only one compression and one expansion load wall are shown in Figure 19, even though two exist: initial load and reload.

71. For Figure 19, the basic characteristic responses are compression and expansion loading. The compression load wall exists in the positive  $q$  and  $\Delta V/V$  space, intersects the failure plane which forms a failure line, and intersects the  $P$ - $\Delta V/V$  plane on the isotropic load line. Anisotropic compression load points lie on the wall in the positive  $q$  and  $\Delta V/V$  space. The expansion load wall exists in the negative  $q$  and  $\Delta V/V$  space, intersects the failure plane which forms a failure line, and intersects the  $P$ - $\Delta V/V$  plane. A dash-dot-dash line is shown along the expansion wall, because the wall cannot be established by isotropic load conditions. In order to establish the wall, anisotropic expansion loading ( $\sigma_H > \sigma_V$ ) would follow a path along the wall in  $-q$  and  $-\Delta V/V$  space.

72. The expansion load wall lies in the  $-q$  quadrant where the major principal axis is less than  $\pm 45^\circ$  to the vertical. The compression load wall lies in the  $+q$  quadrant where the major principal axis is less than  $\pm 45^\circ$  to the horizontal. A stress path, such as for a moving wheel load, that goes from the  $-q$  space to the  $+q$  space and, naturally, has a rotation or changing of the principal axes must pass through the isotropic ( $q = 0$ ) plane ( $P$ - $\Delta V/V$  plane). All paths pass through the  $P$ - $\Delta V/V$  plane along a unique line. This line is labeled in Figure 19 as the line of  $90^\circ$  change of principal axes. Above the line, the major principal axis is less than  $\pm 45^\circ$  to the horizontal, and below the line the major principal axis is less than  $\pm 45^\circ$  to the vertical. In laboratory triaxial tests following a moving-wheel stress path, the line of axes change represents where the sample passes through isotropic load ( $\sigma_H = \sigma_V$ ) state, and the major principal axis rotates  $90^\circ$ . At the

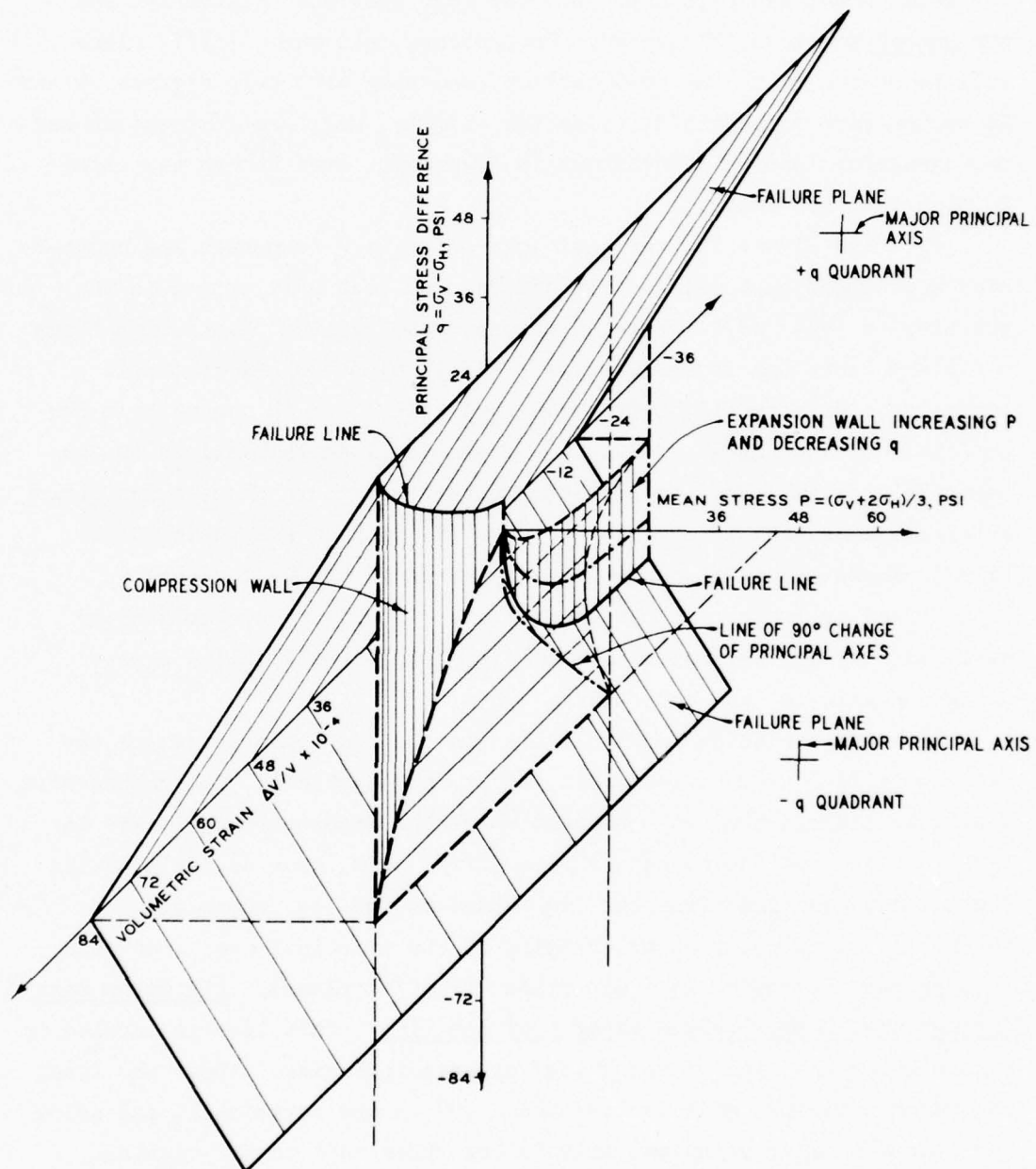


Figure 19. General deformation load model

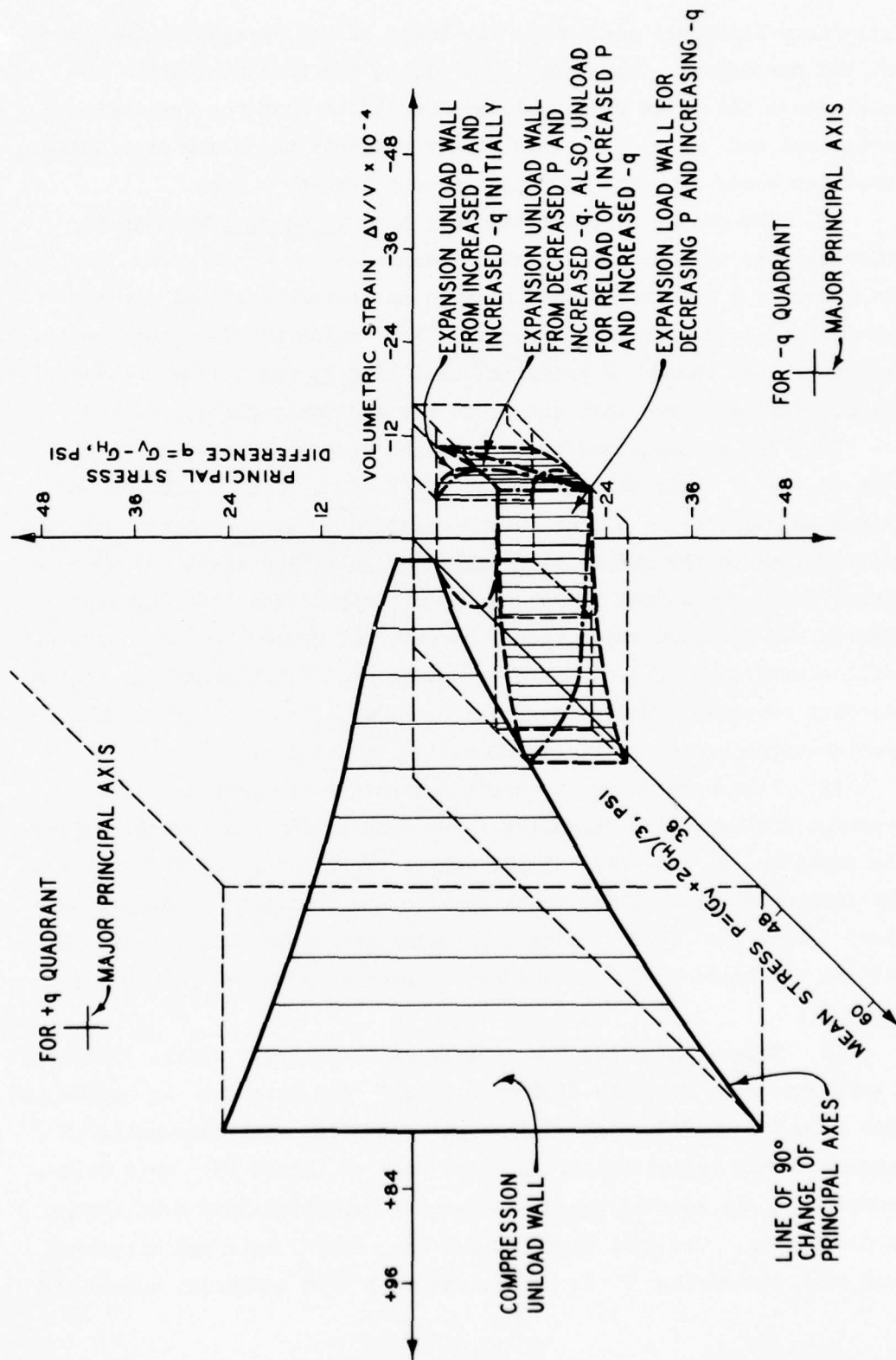


Figure 20. General deformation unload model

laboratory isotropic load state the major principal axis is both vertical and horizontal. For field conditions, the line represents the point where the major principal axis is  $45^\circ$  to both the vertical and horizontal and  $\sigma_H = \sigma_V$ . This line represents the state separating expansion zones from the compression zone beneath a load.

73. The change of principal axes line is unique, because it represents an unload from expansion (decrease in  $-q$  back to  $q = 0$  even though  $P$  is increasing) back to an isotropic unload state. Isotropic unload state has a unique  $\Delta V/V$  value as discussed previously. Therefore, the change of principal axes line is the unique characteristic unload response curve that exists in the isotropic plane,  $P-\Delta V/V$ .

74. For a wheel-loading stress path such as Figure 17, point A lies on the  $P$  axis at  $q = 0$  and  $\Delta V/V = 0$ , point B lies on the expansion wall, point C lies on the change of principal axes line, and point D lies on the compression wall. For a moving wheel and when the stress state moves from the change of principal axes line (located between the bow wave and directly beneath the wheel) to the compression wall, a very fast movement must be occurring. Field-measured vertical velocity response, References 3 and 8, shows this to be true with accelerations exceeding the acceleration of gravity.

75. Figure 20 shows the basic characteristic responses for compression and expansion unloading. The compression unload wall exists in the positive  $q$  and  $\Delta V/V$  space and intersects the  $P-\Delta V/V$  plane at the isotropic unload line, which is also the change of principal axes line. Above the  $P-\Delta V/V$  plane the major principal axis is less than  $\pm 45^\circ$  to the horizontal. Anisotropic compression unload points lie on the wall.

76. Expansion unload has several characteristic walls. There is a wall extending from the isotropic unload line into the  $-q$  space and back into the  $-\Delta V/V$  space. The wall comes in, with decreasing  $P$ , tangent to the expansion initial load wall of Figure 19. This occurs because  $-q$  is increasing and represents expansion load even though  $P$  is decreasing. The wall farthest out the  $-\Delta V/V$  axis and extending back with decreasing  $P$  is the unload wall from expansion reload and

the unload wall from the above expansion load wall for decreasing  $P$  and increasing  $-q$ . Decreasing  $P$  and increasing  $-q$  and coming to the expansion load wall affects a material as if it has been reloaded by increasing  $P$  and increasing  $-q$  from at-rest state. Therefore, unloading from the  $+q$  space into the  $-q$  space and to at-rest state will always follow the expansion unload from reload wall. The inner expansion unload wall, going back to at-rest state, is the unload wall from initial expansion loading. Unload from expansion reload is along the outer wall going back to at-rest state. This above unload behavior in the  $-q$  space materialized from laboratory test results and will become more clear in the next section. At the time of writing this report, the author is not sure why two expansion unload walls exist. They may be occurring because of laboratory-imposed test conditions.

77. Because of the stress path, load history, and distributed traffic for moving wheel loads (which must include compaction equipment), a pavement structure point is always moving lastly in the  $-q$  space. Therefore, the author believes that the unload wall for expansion reload is the only one existing in a pavement structure. The inner expansion unload wall occurs in laboratory initial load testing and may, depending on stress history, occur in field plate load testing not on a pavement structure.

78. For unloading of the stress path in Figure 17, point D lies on the compression unload wall in Figure 20, point C lies on the change of principal axes line, point B lies on the expansion load wall for decreasing  $P$  and increasing  $-q$ , and point A lies on the unload wall for expansion reload. The inelastic response that occurs in a material is the difference between the prior to load  $\Delta V/V$  (which is zero in the model) point and the unload  $\Delta V/V$  point. Whether the inelastic response is expansion or compression depends on load history and the portion of a stress path traversed (which means directly beneath a load or at an offset).

79. The  $P-q - \Delta V/V$  model, Figures 19 and 20, will give inelastic and elastic behaviors that are consistent with field-measured behaviors. Elastic and inelastic expansions in front of (bow wave), adjacent to, and

behind a moving wheel load are predicted by the model. Beneath a wheel, the model predicts elastic and inelastic compression. Also, the model predicts a continuously changing or floating no-load reference. The model can be used to simulate a moving wheel load and traffic (whether mixed, distributed, or random) in a laboratory triaxial test. Also, the model can be used to predict plate load tests whether static or dynamic. The difference between a moving wheel and a plate load is the stress paths. Response behavior to any loading (stress path) can be investigated by the  $P-q - \Delta V/V$  model.

#### Laboratory Tests

80. Verification of the  $P-q - \Delta V/V$  model must come from both laboratory and field testing. As previously discussed and consistent with field measurements, Part II, the model predicts a floating reference. Therefore, laboratory testing of the model must use a floating reference. The laboratory sample floating reference is the changing at-rest volume. In other words,  $\Delta V/V$  load must be calculated in laboratory tests by using the changing at-rest volume as the initial volume for each loading. The final load volume of each loading should be used in calculating  $\Delta V/V$  unload, because the unload behavior is distinct and separate from load behavior.

81. An undisturbed sample of Vicksburg loess was investigated in a drained triaxial test. Vicksburg loess is a frictional and cohesive ( $\phi$  and  $C$ ) soil with  $\phi$  averaging about  $26^\circ$  and  $C$  averaging about 6-7 psi. The undisturbed sample conditions were average dry density  $\gamma_D$  of 86.3 pcf, average water content  $\omega$  of 19.0 percent, a liquid limit of 27, and a plastic limit of 24. A standard 6-in.-high and 2.8-in.-diam triaxial specimen was used with frictionless platens. LVDT clamps (Reference 13) were used during testing to externally measure volume changes of the center two-thirds of the specimen. Two LVDT clamps measured diameter changes, and two clamps measured height changes.

82. Figure 21 shows the various stress path tests that were conducted on the loess sample. At-rest condition was  $P = 3$  and  $q = 0$ . To establish the characteristic response walls of the  $P$ - $q$  -  $\Delta V/V$  model, only expansion and isotropic compression tests need to be conducted. The load series for these characterization tests needs only to be a few load, unload, and reload tests. Figure 21 shows the characterization stress paths as compression load path along the  $P$  axis with  $q = 0$  and the expansion load path. For this loess characterization test more cycles than necessary were conducted. The characterization tests were as follows:

- a. Expansion to  $P = 11$  and  $q = -12$  and unload.
- b. Compression load, unload, and reload cycles to  $P = 30$ ,  $q = 0$ .
- c. Expansion to  $P = 11$  and  $q = -12$  and unload.
- d. Compression to  $P = 45$  and  $q = 0$ , and unload.

Data were taken at several points along the paths.

83. The above loess characterization tests formed the unique walls of the  $P$ - $q$  -  $\Delta V/V$  model. Figures 19 and 20 are for the loess sample. Projection of the  $P$ - $q$  -  $\Delta V/V$  model onto the  $P$ - $\Delta V/V$  plane results in Figure 22. Figure 22 shows the data from the above loess characterization tests and how they formed the basic behavior responses of the model.

84. Due to the uniqueness of the  $\Delta V/V$  responses, reloading past a prior load point comes to the initial load curve. This is how the initial load curve of Figure 22 was developed, and this behavior will be verified in a sand test presented later.

85. In order to illustrate the meaning of the characteristic response curves of Figure 22, consider a compressive loading and unload cycle for  $P = 3$  to 18 to 3. If the loading is an initial load, the volumetric strain  $\Delta V/V$  will follow the initial load curve to  $P = 18$ . However, if the loading is a reload, the  $\Delta V/V$  path will follow the reload curve. The unload  $\Delta V/V$  path from either initial loading or reloading will follow the unload curve from  $P = 18$ . Elastic response will be the  $\Delta V/V$  unload, inelastic response will be the difference

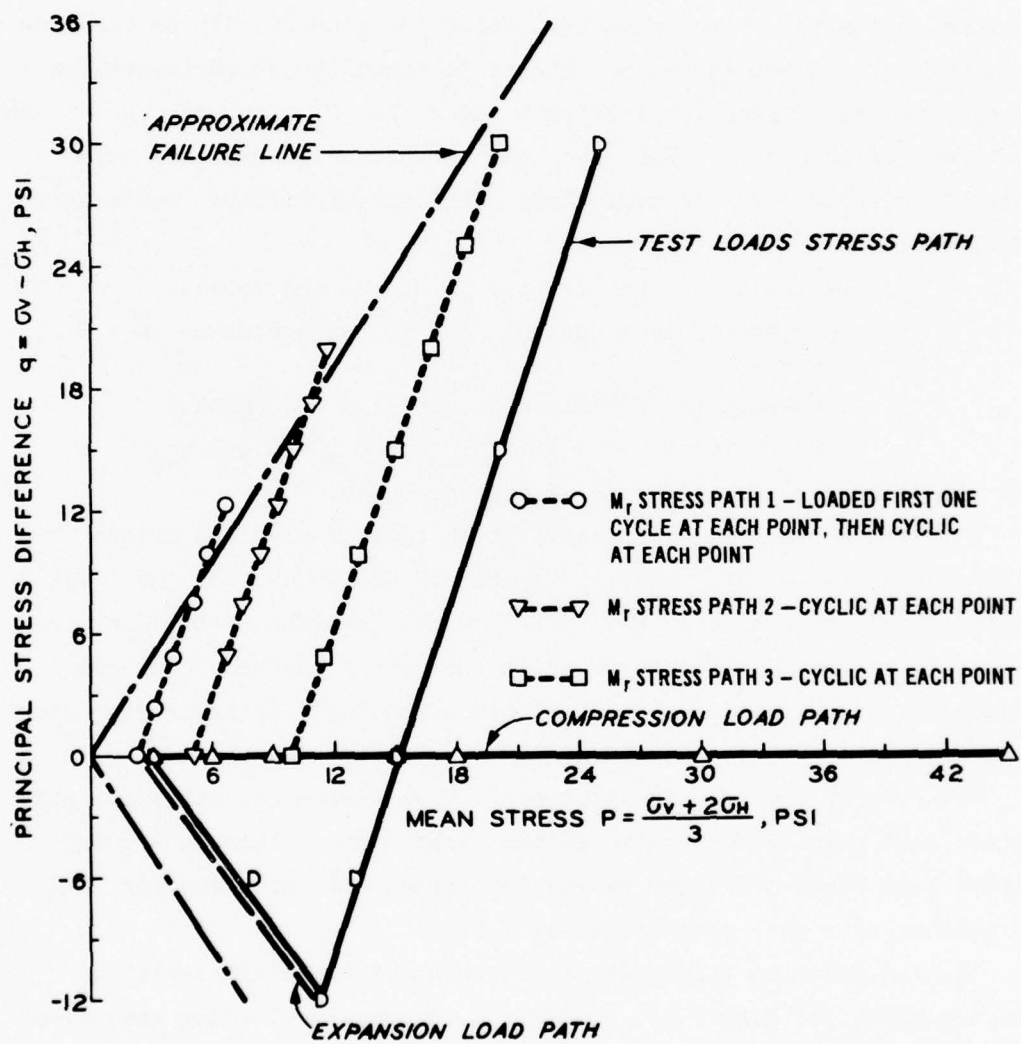


Figure 21. Stress path tests for Vicksburg loess

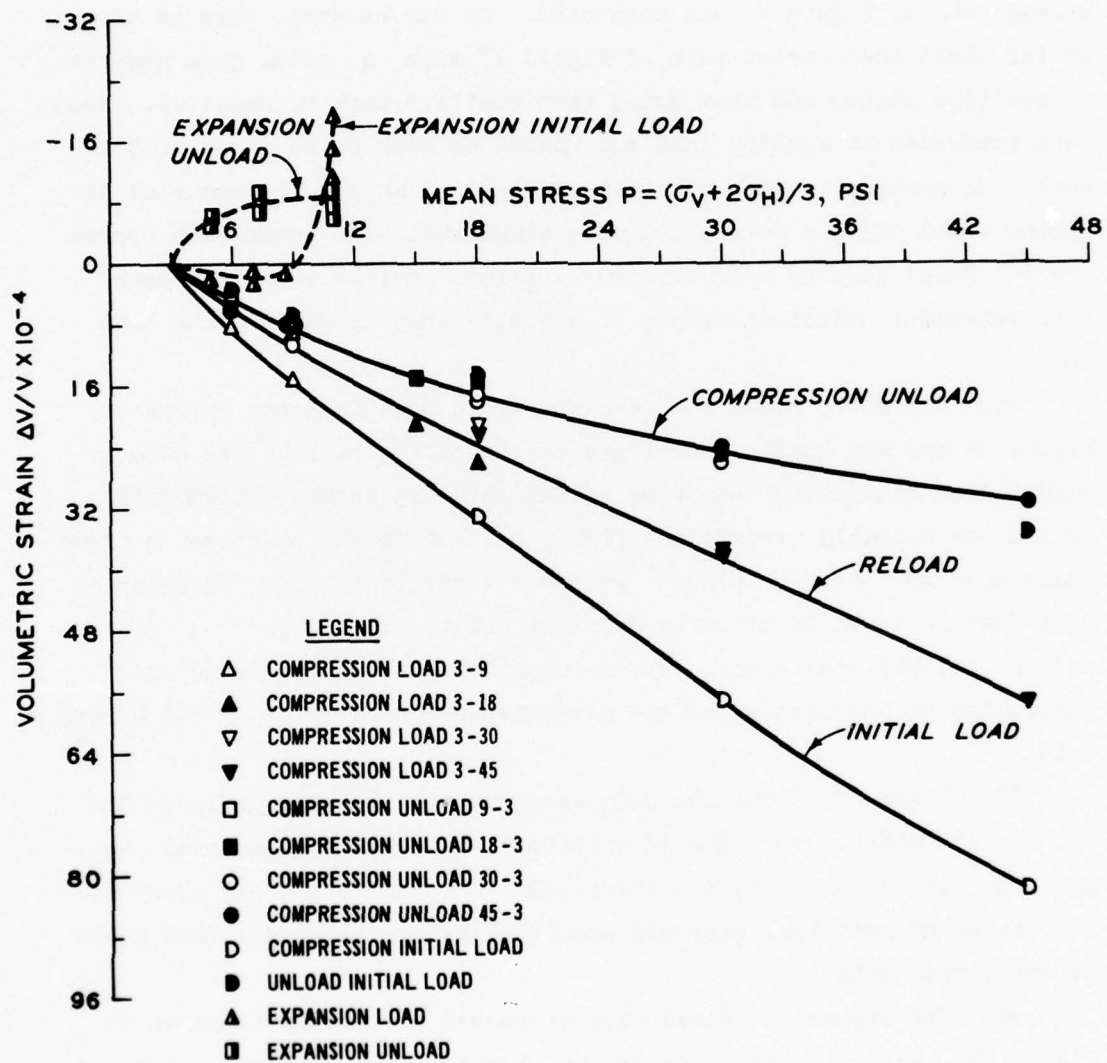


Figure 22. Compression and expansion characteristics for Vicksburg loess

between unload at  $P = 18$  and the initial load or reload at  $P = 18$ , and the simultaneous elastic plus inelastic response will be the initial load or reload  $\Delta V/V$ .

86. To further verify the  $P$ - $q$  -  $\Delta V/V$  model, the test loads stress path of Figure 21 was conducted. As can be seen, this is the moving wheel load stress path of Figure 17 with  $q$  going from negative to positive states and then going from positive back to negative. Tests were conducted by cycling load and unload to each point shown on the path. By cycling to each point in succession, an orderly sequence of moving wheel offsets to a point were simulated. The total path represents a wheel passing directly over a point. Points along the path also represent offset distances to a static wheel load or plate load test.

87. Figure 23 shows the characteristic load response curves of Figure 22 for the loading model projection of Figure 19. The data points from conducting the above stress path are shown. These data points are actually projections from the negative and positive  $q$  space walls onto the  $P$ - $\Delta V/V$  plane. In other words, the  $\Delta V/V$  deformation path that is shown is actually twisting and turning in the  $-q$  space and up into the  $+q$  space. The deformation path is predicted and controlled on the load walls and moves between load walls by the stress path.

88. Figure 23 shows the uniqueness of the response walls of the  $P$ - $q$  -  $\Delta V/V$  model. The line of principal axes change separating  $-q$  and  $+q$  spaces was discussed previously. In Figure 23, the point of  $90^\circ$  change of principal axes was specified by the isotropic load point of the stress path.

89. The expansion reload path discussed previously is shown in Figure 23. With the first loading to  $P = 11$ , the response point was on the initial expansion curve. Subsequent loadings fell on the expansion reload curve except for the second loading to  $P = 25$ . As is obvious, the initial expansion load curve becomes very sensitive to load magnitude. The author believes the second loading to  $P = 25$  had magnitudes slightly greater than  $P = 11$  and  $q = -12$  at the

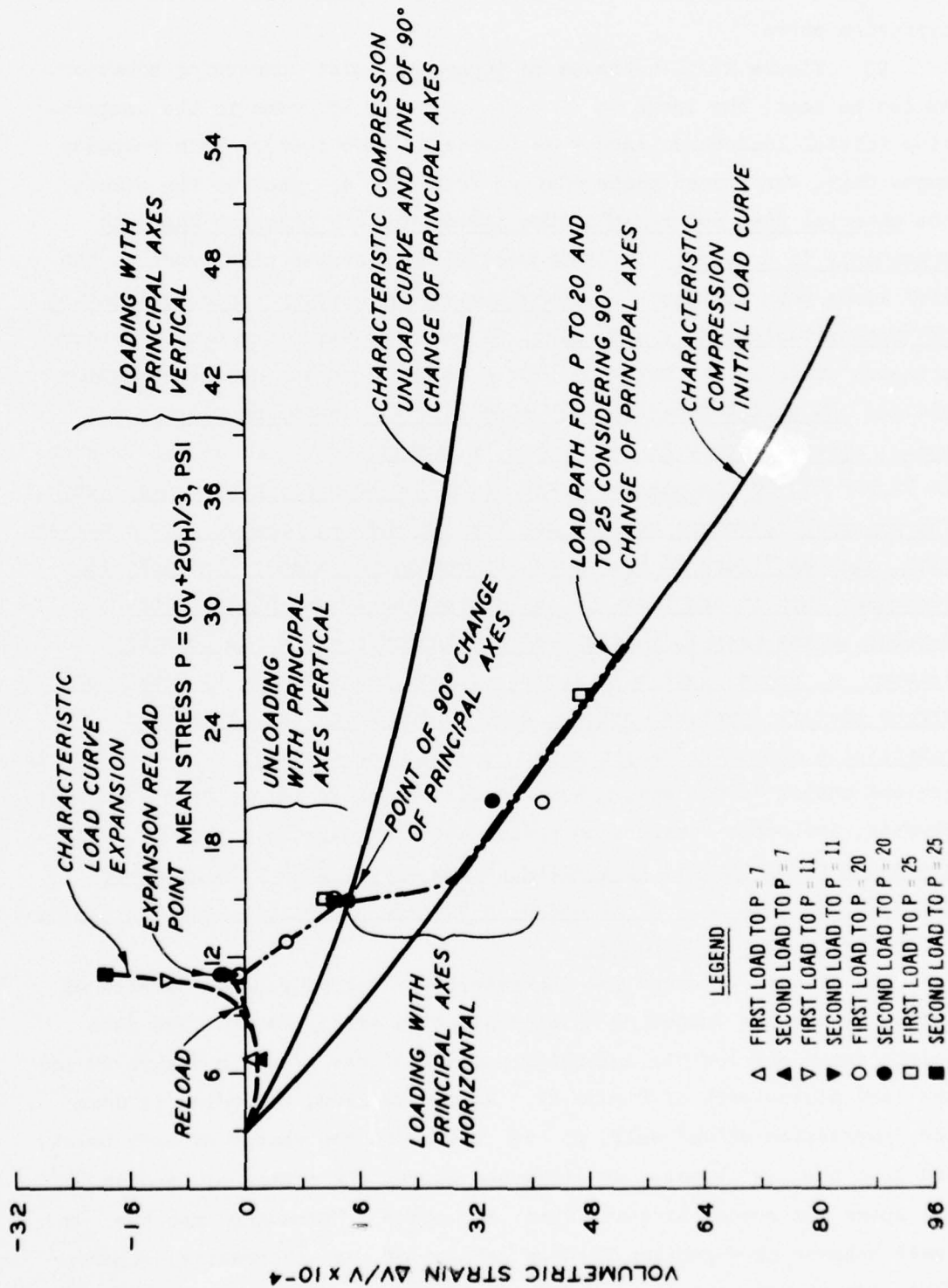


Figure 23. Stress path load response of Vicksburg loess

stress path turning point. Therefore, the response fell on the initial expansion curve.

90. Figure 23 illustrates an important point concerning behavior. As can be seen, the loads to  $P = 20$  and  $P = 25$  came to the compression initial load curve each time (twice at each load). This response means that, for stress paths that go from one  $q$  space to the other, the material does not remember the stress history that has happened previously in a space. In other words, for a stress path, such as the test loads path of Figure 21, previous stress history (preconsolidation or precompression) does not exist. A pavement structure has no precompression state in its materials for a moving load but has preexpansion states. By moving from the  $-q$  space to  $+q$  space and back to  $-q$  space, stress history in  $+q$  space is erased. However, as can be seen in Figure 23, if the path stays in or on the boundary of the  $-q$  space, the material remembers that it has been in the  $-q$  space. For a stress path, such as Figure 18 that does not change  $q$  spaces, the material remembers when it has been in  $+q$  space, and stress history states develop as the path is loaded. If a path moves along the boundary between  $q$  spaces (which is isotropic load conditions), it establishes stress history (preload) states, such as the load, unload, reload compression characterization tests described previously. These isotropic preload states do not get erased, as will be shown later for a sand test. However, isotropic compression erases the  $-q$  expansion history. The above can be summarized by stating that a stress path will remember where it has been only if it stays in the  $-q$  space, in the  $+q$  space, or on the isotropic boundary.

91. Figure 24 shows the characteristic unload response curves of Figure 22 for the unloading model projection of Figure 20. The data points shown are for the unloading portion of the tests in Figure 23 and the test stress path of Figure 21. As can be seen, unloading is down the compression unload wall, in  $+q$  space, to the change of axes point, and into the  $-q$  space. As discussed above, the effect of loading in  $-q$  space was erased by going into  $+q$  space. Unloading into the  $-q$  space behaves as expansion loading because of  $-q$  increasing. Therefore, the unload path is to the initial expansion load wall. From the

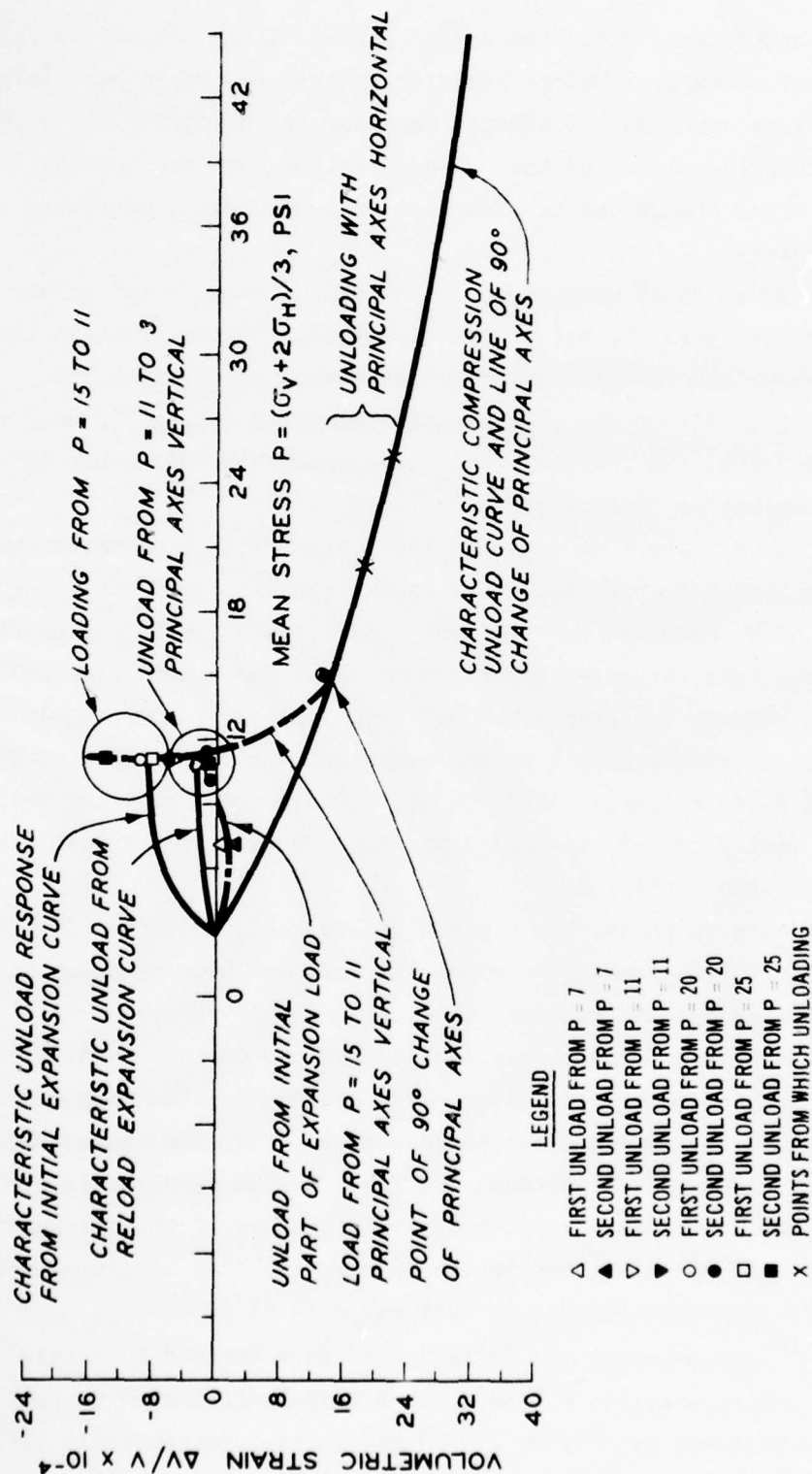


Figure 24. Stress path unload response of Vicksburg loess

initial expansion load wall, the unload path is along the unload from expansion reload wall. (Unload behavior in the  $-q$  space was discussed in the previous section.) Inelastic response is the difference between the prior to load volume and the unloaded volume for each loading. The inelastic volume change can be expansion or compression, depending on the load history.

92. Figures 25-27 show vertical and radial strains and volume changes for the loess expansion and compression characterization tests. Figure 28 shows the  $P-\Delta V/V$  behavior for stress paths which lie entirely in the  $+q$  space. These paths (shown in Figure 21) were for resilient modulus,  $M_R$ , tests, which were conducted before the expansion and compression characterization tests.

93. The  $M_R$  tests were cyclic load tests using a haversine wave form with a load duration of 0.2 sec and a rest time of 3 sec. Figure 28 shows the  $\Delta V/V$  response for the last load cycle at each load point. As shown, the load responses generally followed the compression initial load curve, because the sample had not been previously compressed. Some of the loads of stress path 1 caused expansion, and some loads of stress paths 2 and 3 caused large  $\Delta V/V$  values. The reason for these deviations can easily be seen in Figure 21 and is because the stress states were near failure conditions.

94. Figure 28 shows, for a given cyclic load, that the  $\Delta V/V$  change from prior to loading to where the response becomes constant is the characteristic load response value. The number of cycles required to reach constant conditions is a function of the time property of the inelastic behavior phase. Within a given cycle after the response becomes constant, the load and unload responses lie on the characteristic compression unload curve. Because the load forcing function is cyclic or oscillatory, there is a mean or central tendency of the forcing function. This mean value appears to act as a static load condition from which the dynamic load and unload soil response is occurring.

95. Another material was investigated in a drained triaxial laboratory test. This was a cohesionless Reid-Bedford sand sample constructed to a dry density of 102.36 pcf. The friction angle  $\phi$

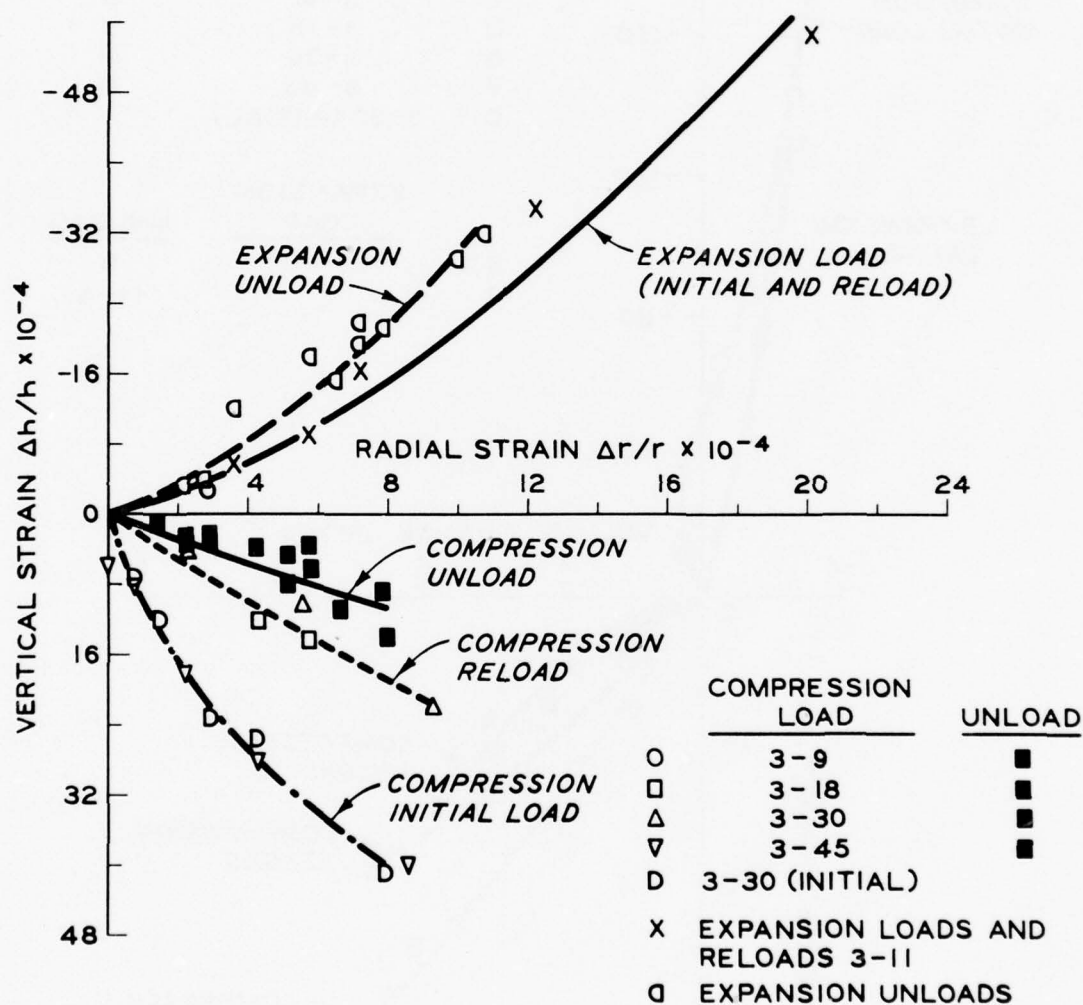


Figure 25. Vertical strain versus radial strain for Vicksburg loess

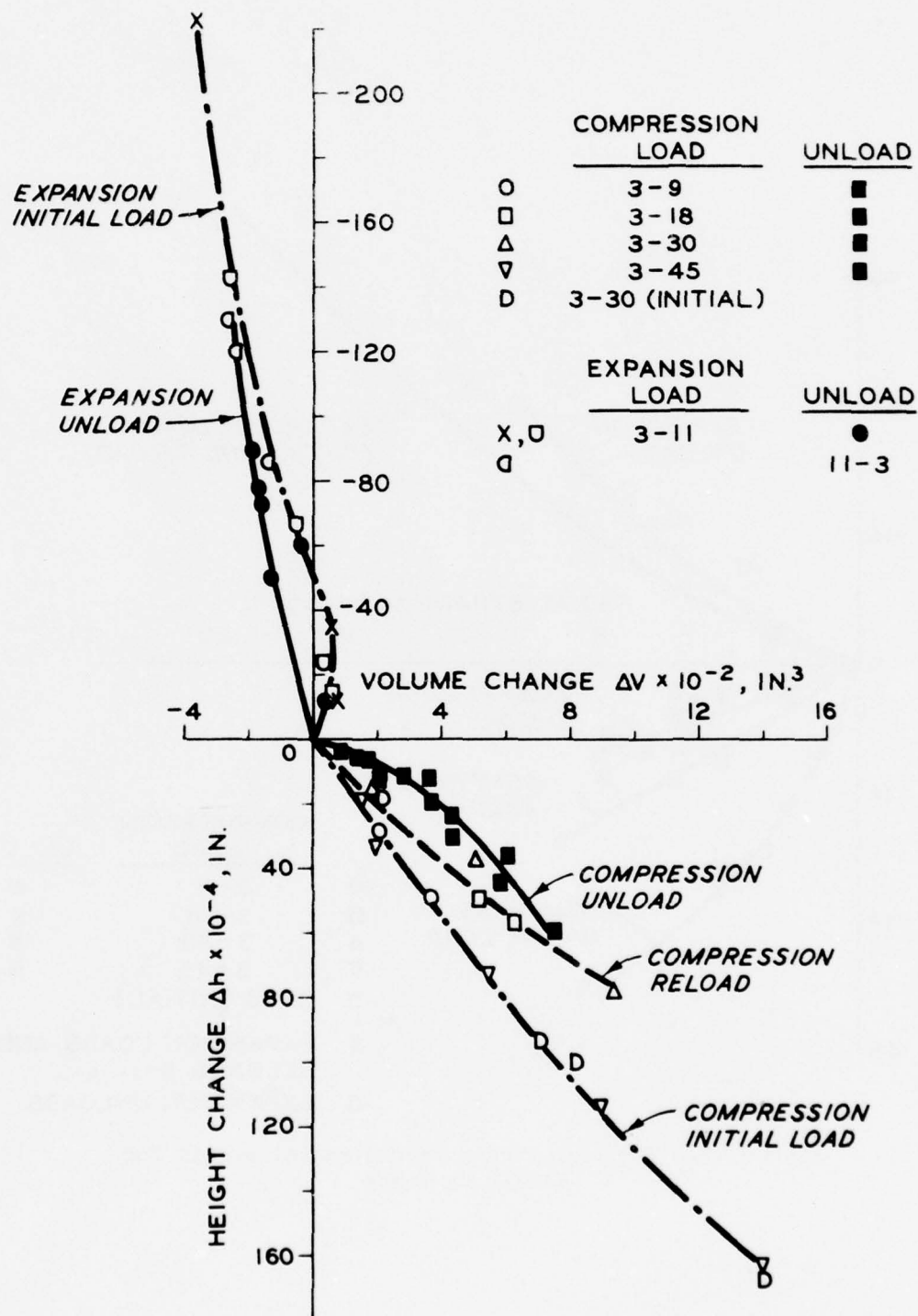


Figure 26. Volume change versus vertical change for Vicksburg loess

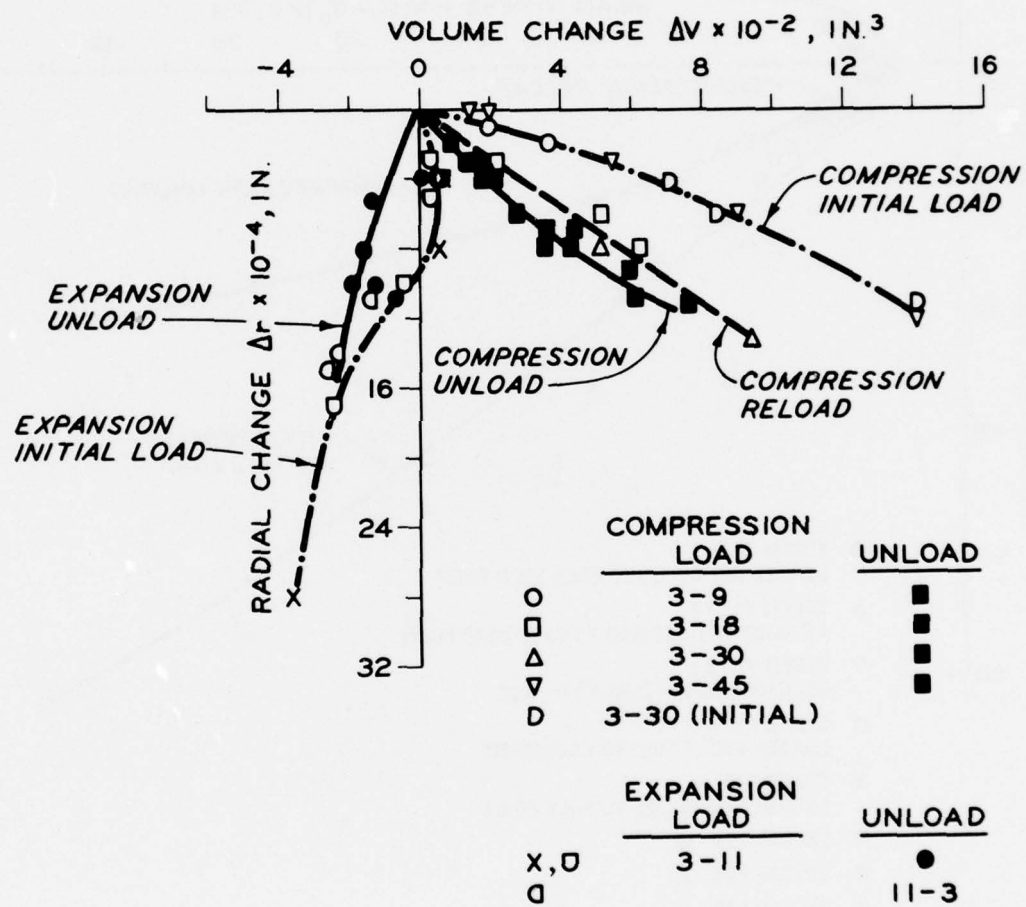


Figure 27. Volume change versus radial change for Vicksburg loess

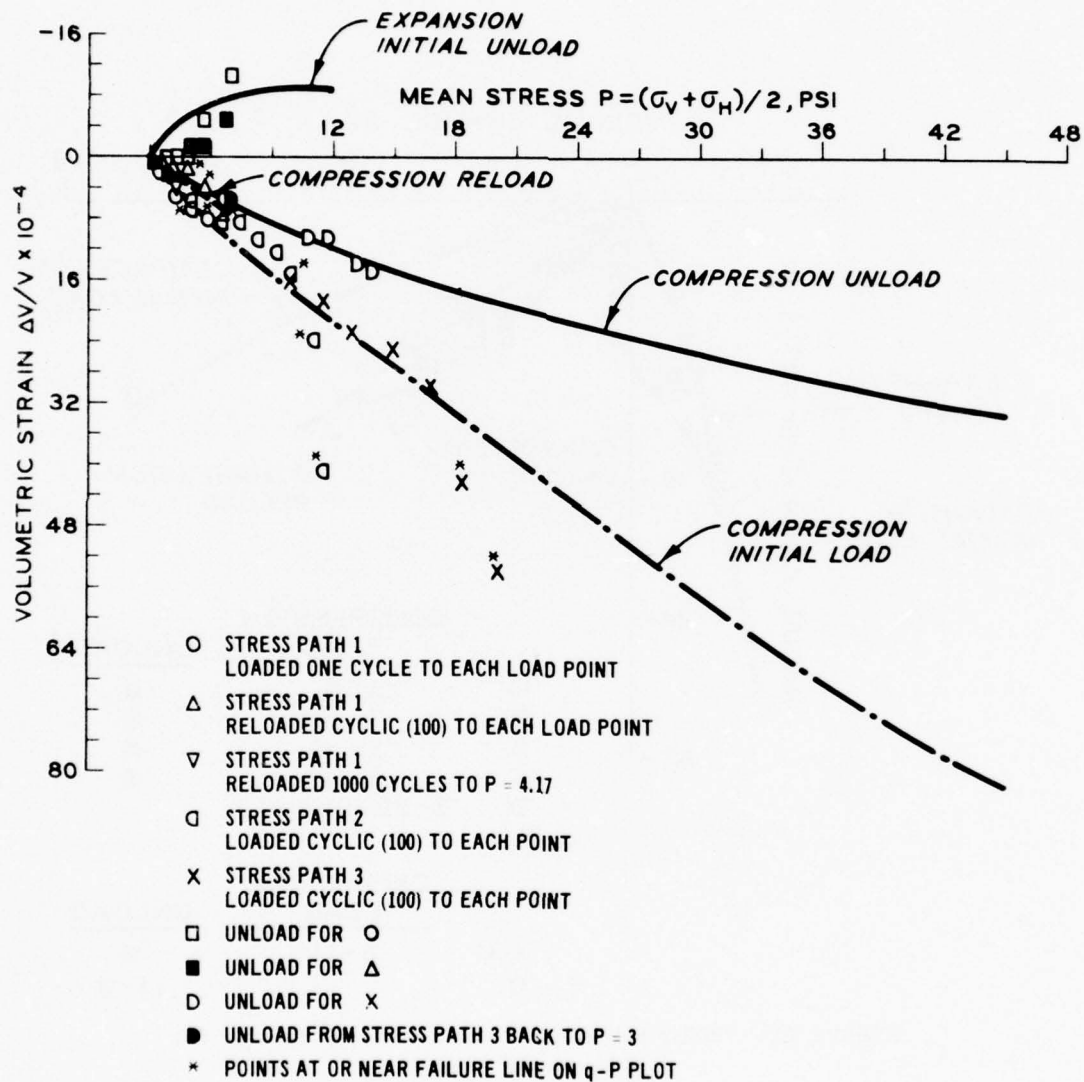


Figure 28. Resilient modulus test behavior for Vicksburg loess

was approximately  $36^\circ$ . A standard 6-in.-high and 2.8-in.-diam triaxial specimen was used with frictionless end platens and back-pressure saturation. Volume changes were measured in the center two-thirds of the specimen by LVDT clamps. Three LVDT clamps measured diameter changes, and two clamps measured height changes. For comparative purposes, volume change burette measurements were made (this is why the sample was saturated).

96. Figure 29 shows the stress path tests that were conducted on the sand sample. At-rest condition was  $P = 6$  and  $q = 0$ . In order to establish the  $P$ - $q$  -  $\Delta V/V$  model for the sand, only expansion and isotropic compression characterization tests needed to be conducted. The sand sample was subjected to the following sequence of tests:

- a. Expansion characteristics to and from  $P = 16$  and  $q = -15$ .
- b. Isotropic compression characterization to and from  $P = 30$ .
- c. Expansion characterization to and from  $P = 16$  and  $q = -15$ .
- d. Isotropic compression characterization to and from  $P = 45$ .
- e. Tests along stress path 1 in Figure 29.
- f. Expansion almost to failure.
- g. Isotropic compression to  $P = 45$ , then unloading.
- h. Expansion characterization to and from  $P = 22$  and  $q = -24$ .
- i. Tests along stress path 2 in Figure 29.
- j. Unloading stress path 2 back to  $P = 0$ ,  $q = 0$ .
- k. Isotropic compression from  $P = 0$  to  $P = 45$ , then unloading.
- l. Isotropic compression to  $P = 12$ , then up  $+q$  space to failure, which gave a  $\phi$  value of  $36^\circ$ .

97. Figures 30 to 34 present the  $P$ - $\Delta V/V$  plane projections for the  $P$ - $q$  -  $\Delta V/V$  model characterizations. (Data shown are LVDT data.) Figure 30 is the expansion initial load and unload characteristics. The load and unload data points along the first part of the curve, which is in the  $+\Delta V/V$  space, came from steps a and c above. Data in the

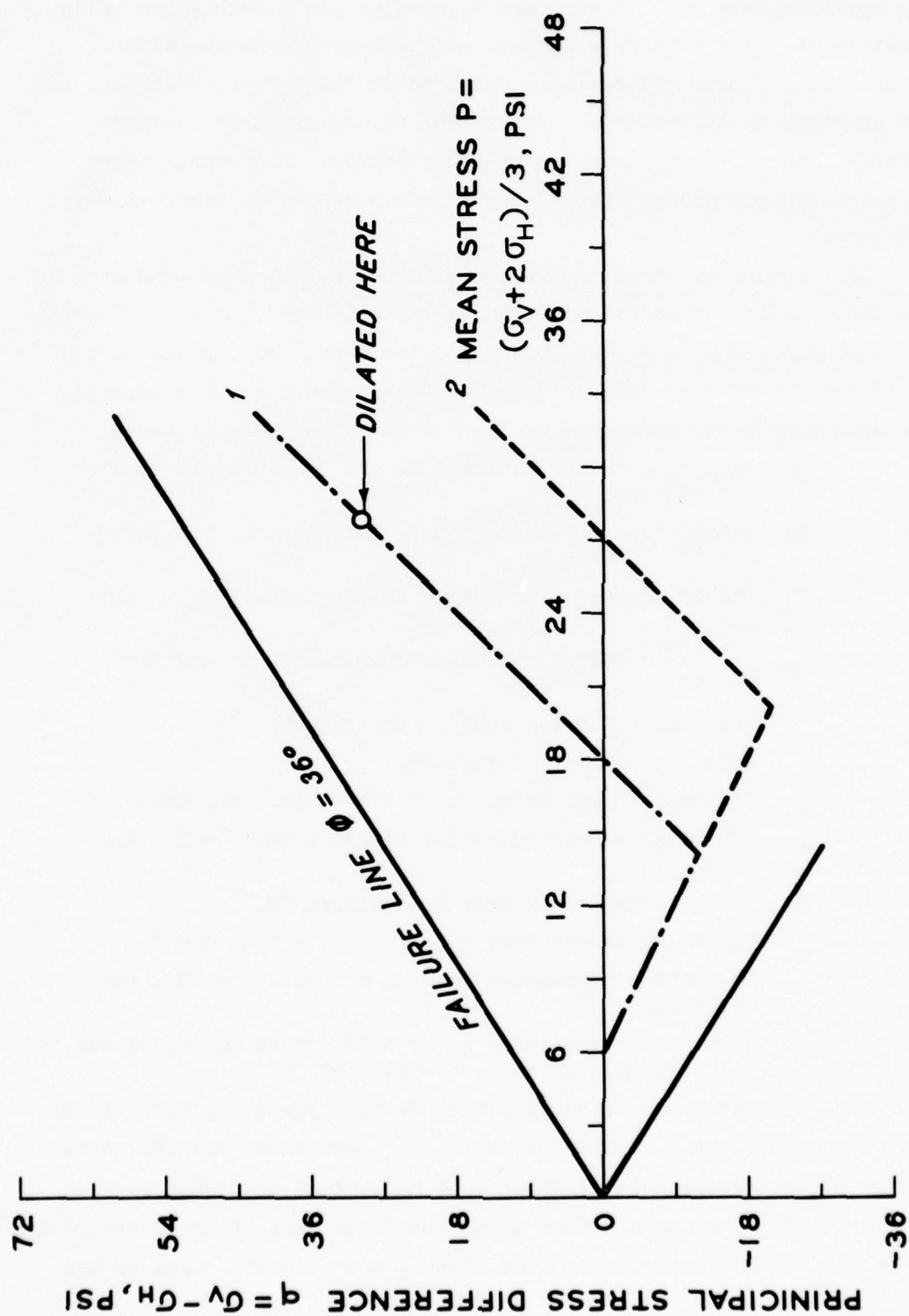


Figure 29. Test stress paths 1 and 2 on Reid-Bedford sand

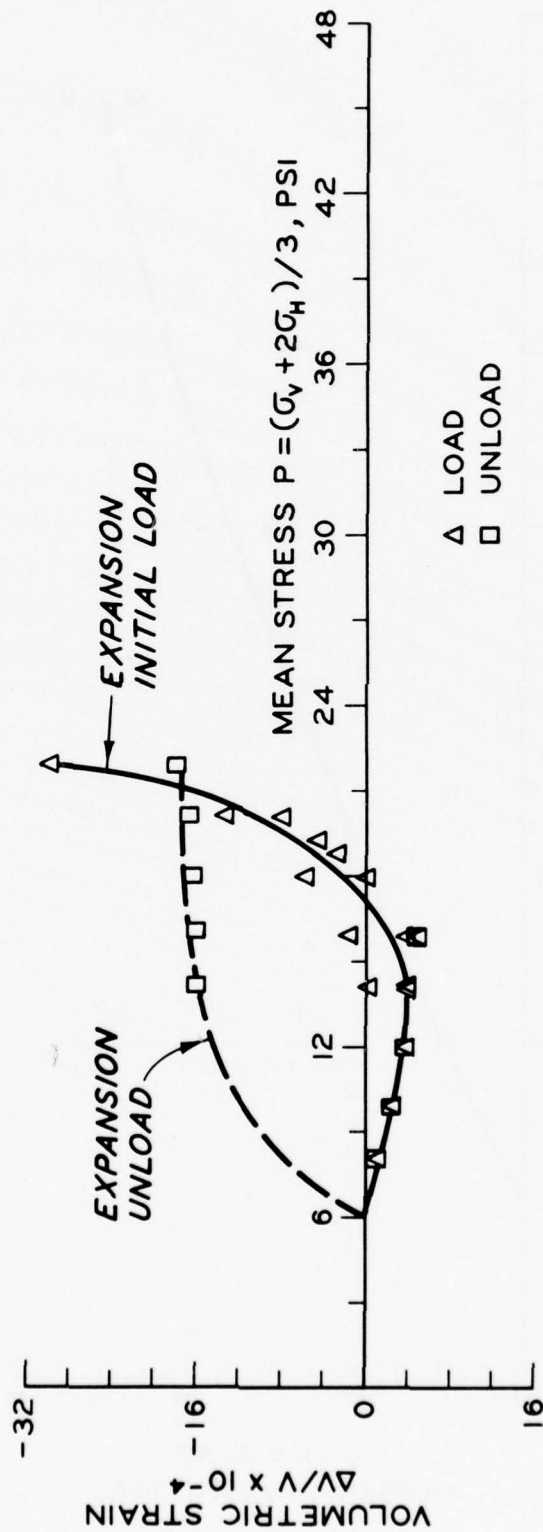


Figure 30. Expansion characteristics for Reid-Bedford sand

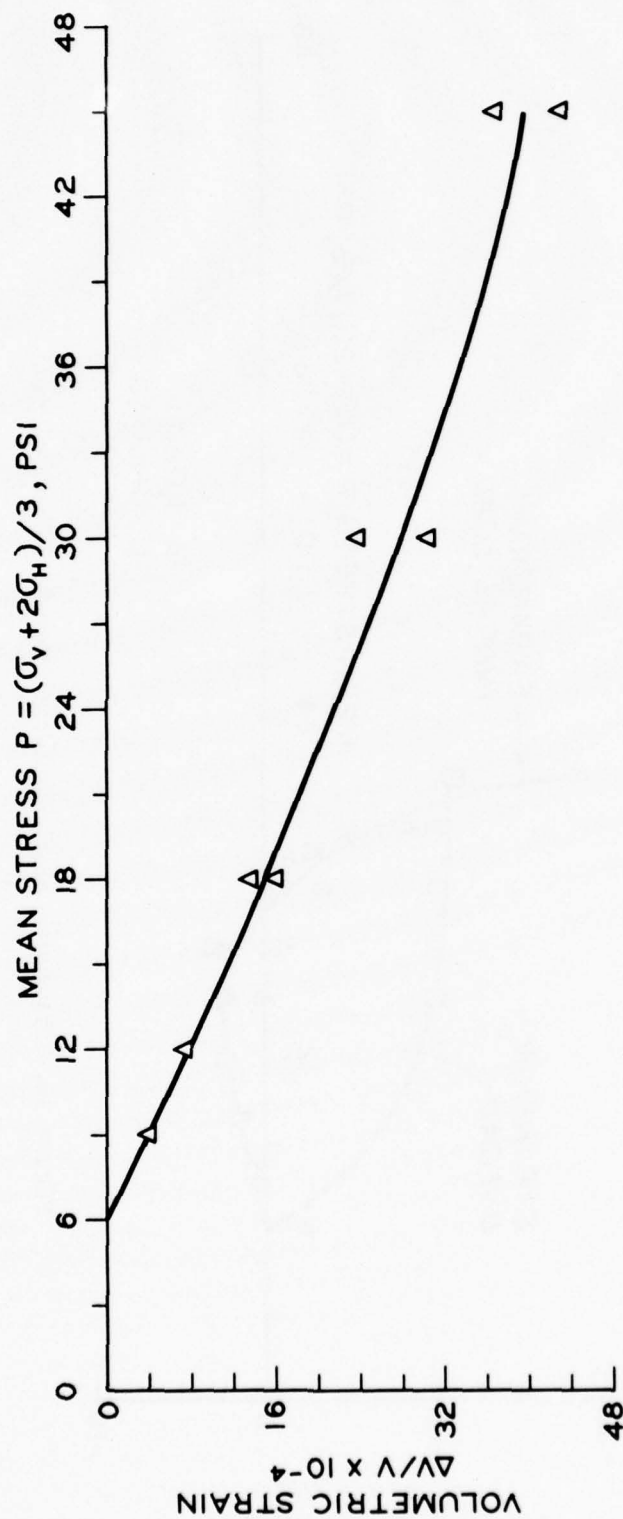


Figure 31. Initial load compression characteristics for Reid-Bedford sand

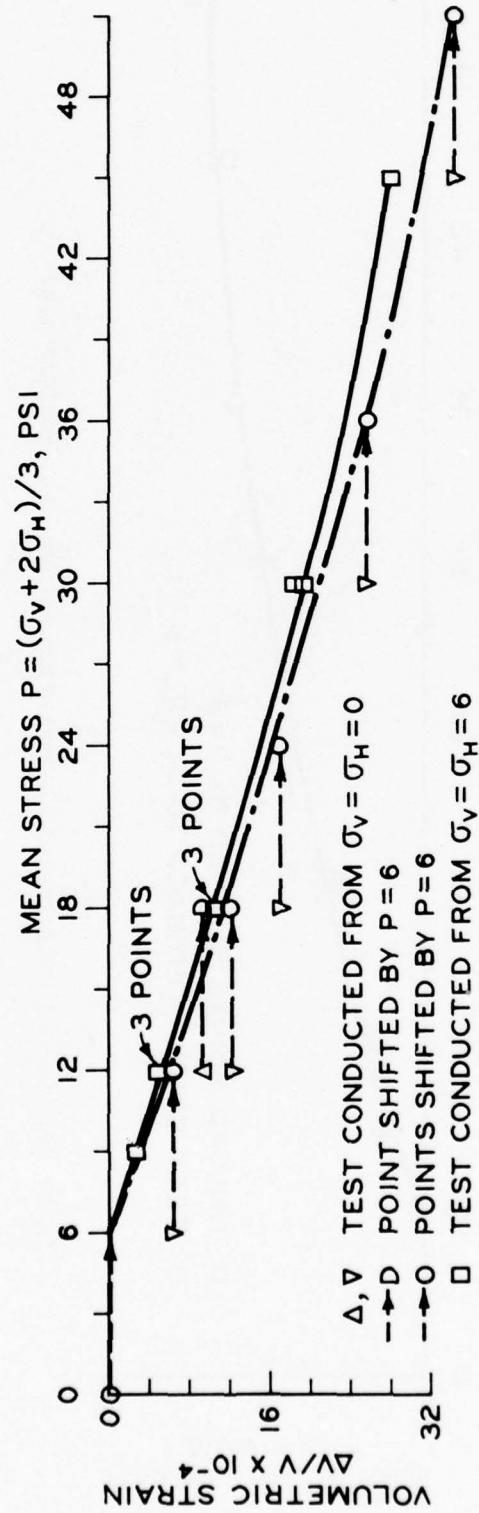


Figure 32. Reload compression characteristics for Reid-Bedford sand

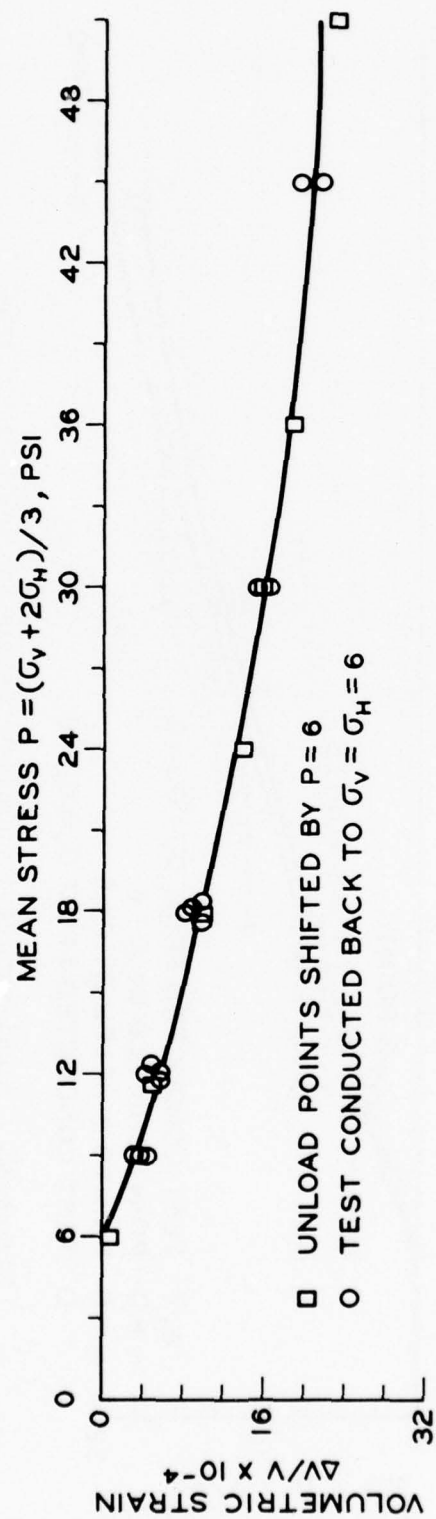


Figure 33. Unload compression characteristics for Reid-Bedford sand

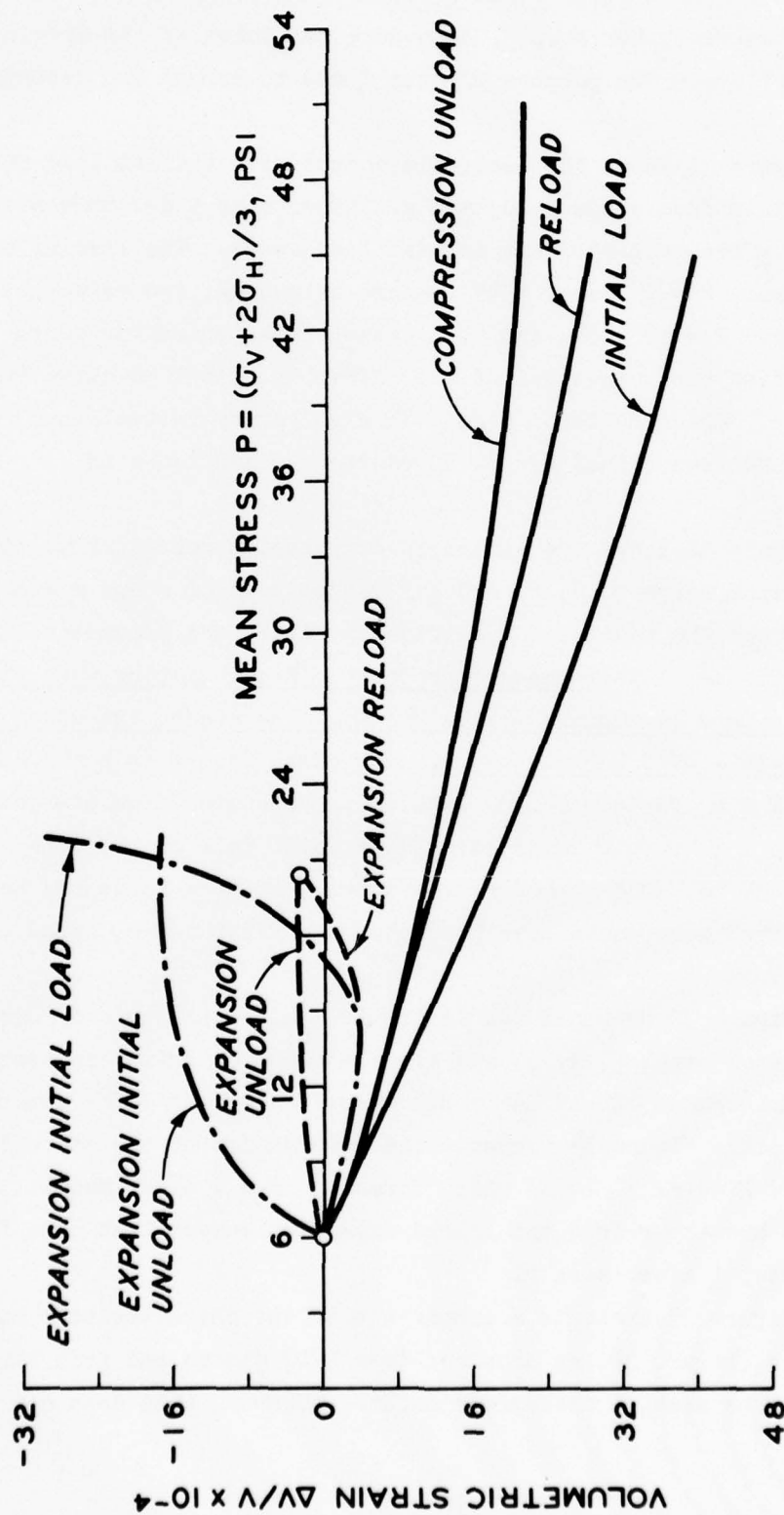


Figure 34.  $P-\Delta V/V$  plane projection of the general deformation model for Reid-Bedford sand

$-\Delta V/V$  space came from steps f and h, after compression and stress path 1 had been run. For step f, data were not taken as the specimen approached failure. The purpose of step f was to expand and decompress the sample.

98. Figure 31 shows the isotropic compression initial load curve with data points from steps b, d, and g. After step f decompressed the sample, step g reestablished the initial load curve. The loading of step g was from  $P = 6$  to  $P = 45$  before unloading, and response was sampled at  $P = 18, 30$ , and  $45$ . These characterization tests further verified the uniqueness of the  $\Delta V/V$  initial load curve in the  $P-\Delta V/V$  plane. The results of Figure 31 also verify initial load  $\Delta V/V$  values obtained from reload cycles as previously mentioned in paragraph 84.

99. Figure 32 shows the isotropic compression reload curve with data points from steps b, d, k, and l. The purpose of steps k and l was to show that the model and specifically  $\Delta V/V$  are dependent on change in  $P$ ,  $\Delta P$ . This means that for a  $\Delta P$ , no matter what the at-rest  $P$ , there are unique  $\Delta V/V$  values. Therefore, the model is a unique  $\Delta P-\Delta q - \Delta V/V$  behavior model. The data from step k are shown shifted by  $P = 6$  for comparison with tests conducted from at-rest  $P = 6$ . Step l isotropic compression data point fell on the other side of the first curve. The author believes that, if more loads had been run, the shifted data would have bracketed the first curve, conducted from  $P = 6$ .

100. Figure 33 presents the isotropic compression unload curve with data points from steps b, d, g, and k. These characterization tests verify the uniqueness of the isotropic unload curve and  $\Delta V/V$  unload for  $\Delta P$  unload. Figure 34 presents the combination of the characteristic curves of Figures 30 to 33 which form the  $P-q - \Delta V/V$  model. Shown in Figure 34 are the reload and unload expansion curves that came from conducting step i after step h.

101. Figure 35 presents a comparison of the characteristic response curves (Figure 34) as obtained from LVDT clamps and from burette data. As can be seen, a difference exists; however, this does not

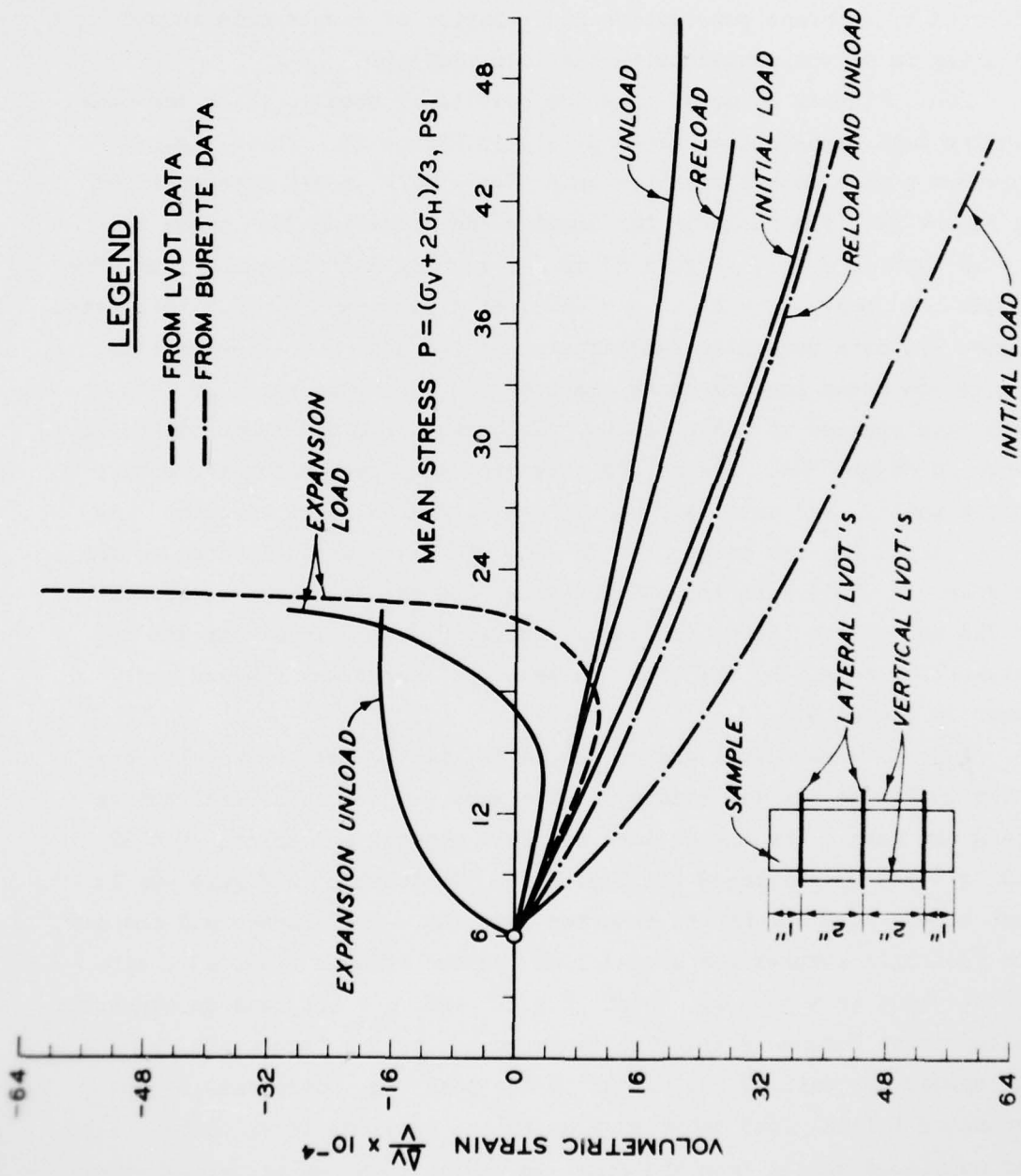


Figure 35.  $P-\Delta V/V$  plane projection for burette data of Reid-Bedford sand

violate the unique  $\Delta P - \Delta q - \Delta V/V$  model as will be shown later in this section. The author believes that the LVDT data from the sample center are more accurate than the burette data. Burette volume data are affected by membrane penetration and behavior of sample ends caused by being in direct contact with the load platens.

102. Figures 36 to 39 show the results of step e, which was conducting load tests along stress path 1 in Figure 29. These figures show how stress path 1 fits the sand  $P-q - \Delta V/V$  model characterized in Figure 34. Figure 36 is for loading and unloading four times to  $P = 10$  and  $q = -6$ . Figure 37 is for loading and unloading four times to the  $-q$  peak ( $P = 14$ ,  $q = -12$ ) of stress path 1. For this test, Figure 37, data were also sampled at  $P = 10$  and  $q = -6$  each time. Figure 38a shows loading three times to the isotropic point of path 1 with data sampled at other points. Unloading from the isotropic point is shown in Figure 38b. Figure 39a shows loading twice along the entire stress path 1, and data sampled at several points along the path. As can be seen, the end point  $P = 32$  and  $q = +42$  was dilating, volume increasing. This dilation mode affected the unload behavior, because it did not follow the unload curve. However, the unload response had returned to normal by the time the peak  $-q$  point was reached, as shown in Figure 39b.

103. Stress path 2 was conducted in step i, and the results are shown in Figure 40a for loading. Data were sampled at several points along the path. The author does not know why the end point,  $P = 32$  and  $q = +15$ , fell below the load line. Noticeable in Figure 40a is that stress path 2 took the behavior into the  $-\Delta V/V$  space and crossed the isotropic compression unload line (change of axis line) at a different value from path 1. Point  $P = 20$  and  $q = -21$  was an expansion reload point because step h was an expansion test. Figure 40b shows the unload for path 2, and unload to the peak  $-q$  point came to the expansion initial load curve just as in the previous loess tests. Also, the continued unload from the peak  $-q$  point is along an unload curve from expansion reload just as for the loess tests. Step j was the

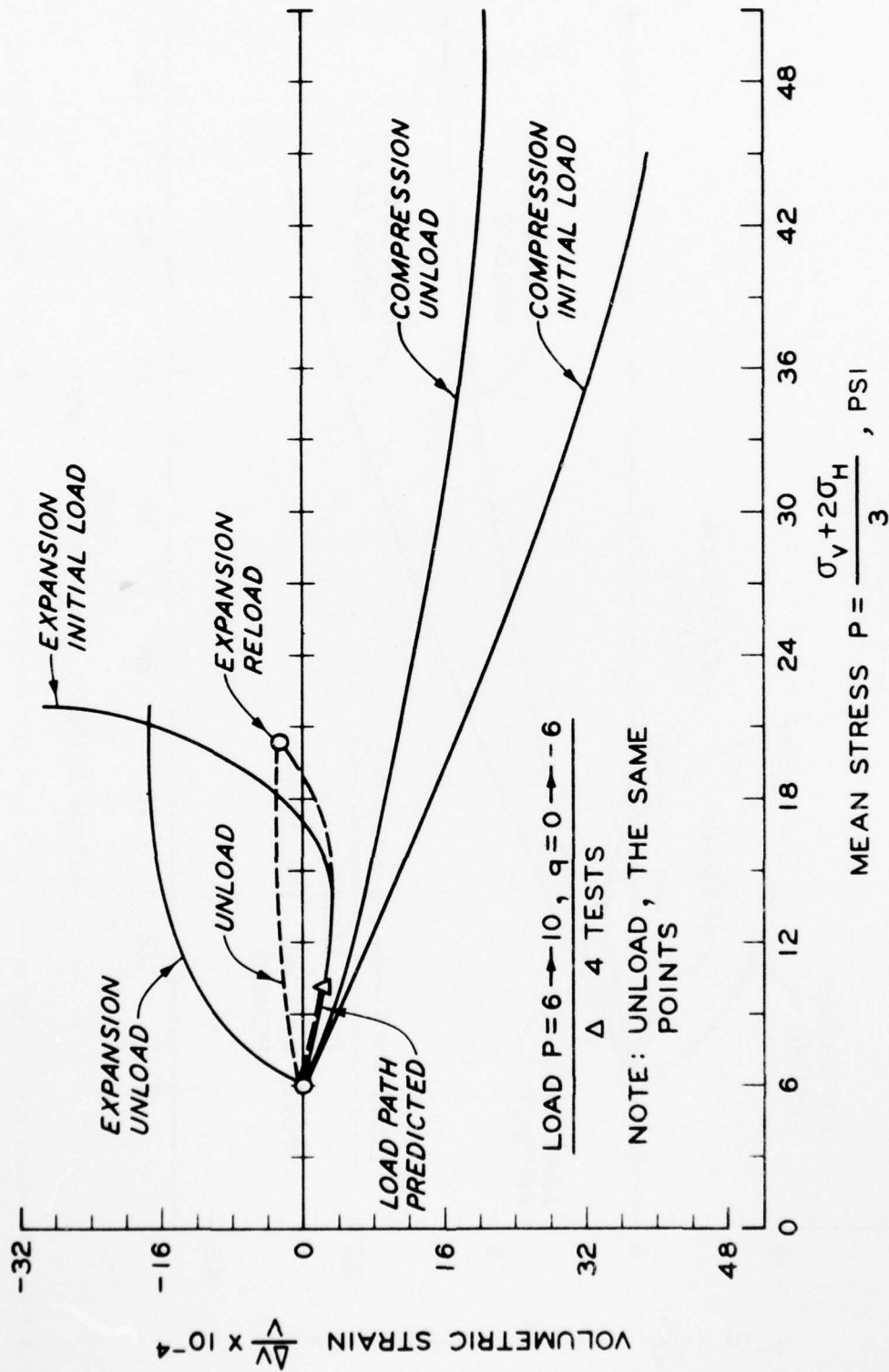


Figure 36. Load and unload stress path test for Reid-Bedford sand,  $P = 6$  to  $10$  and  $q = 0$  to  $-6$

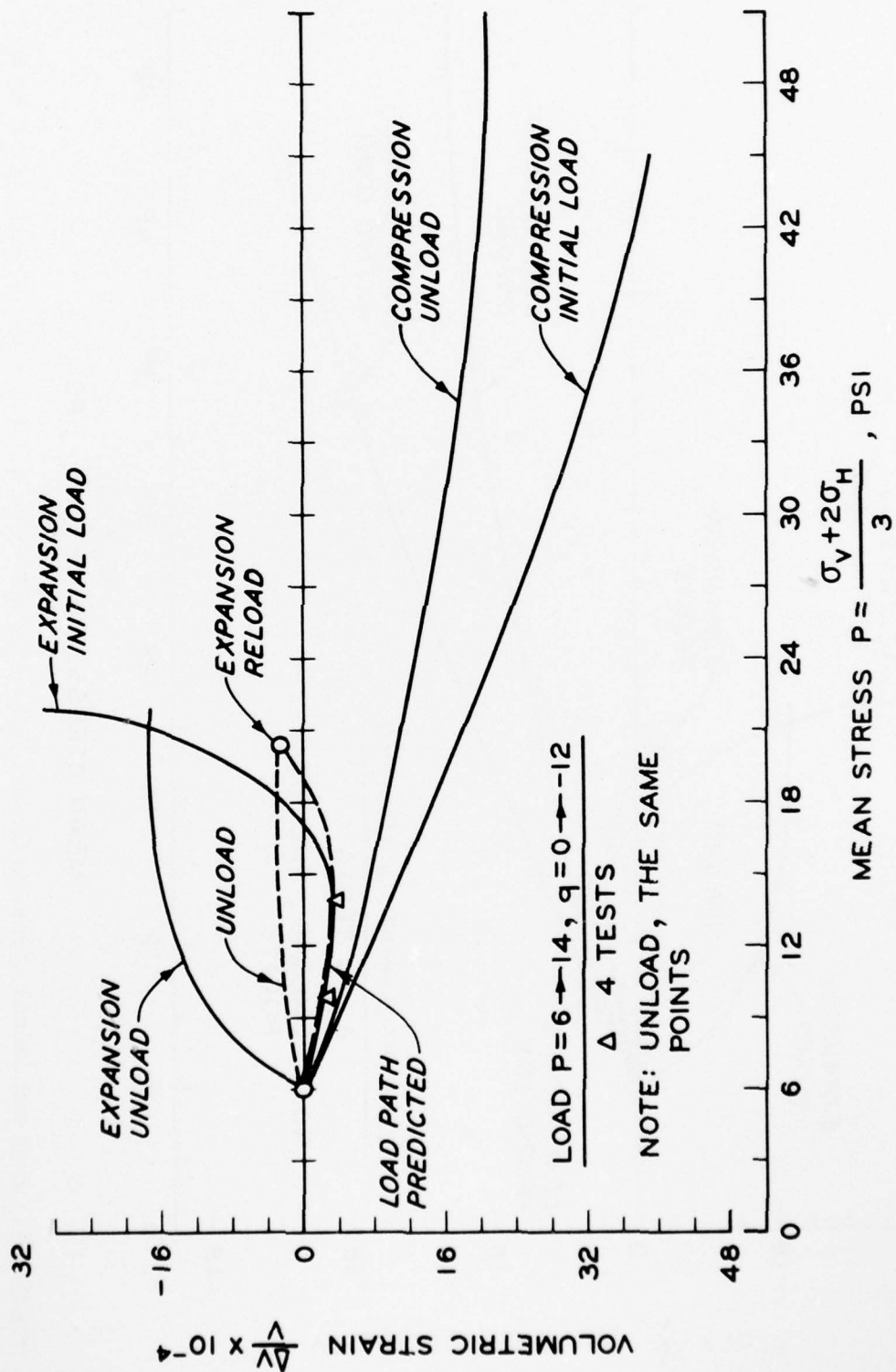


Figure 37. Load and unload stress path test for Reid-Bedford sand,  $P = 6$  to  $14$  and  $q = 0$  to  $-12$

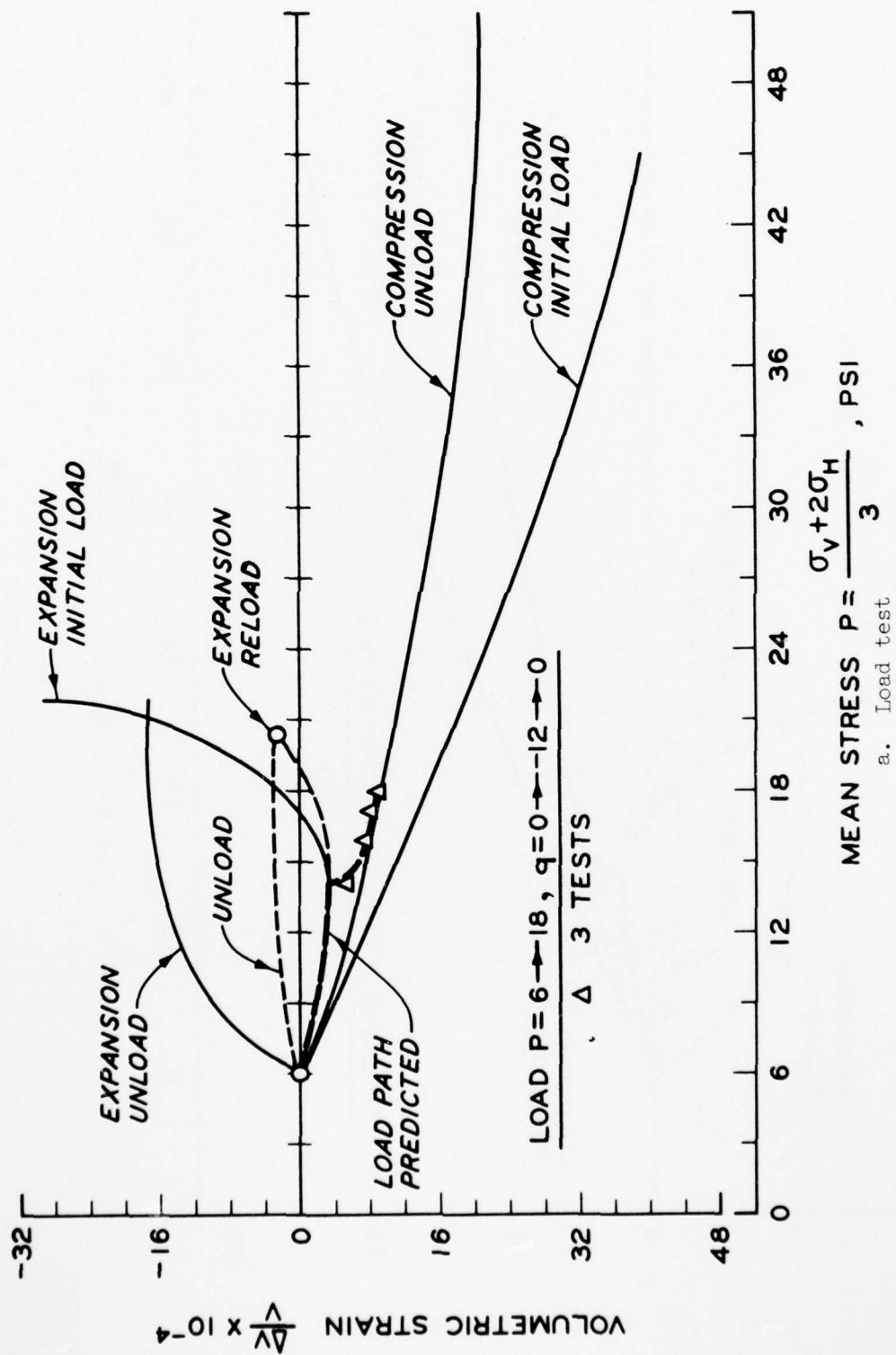
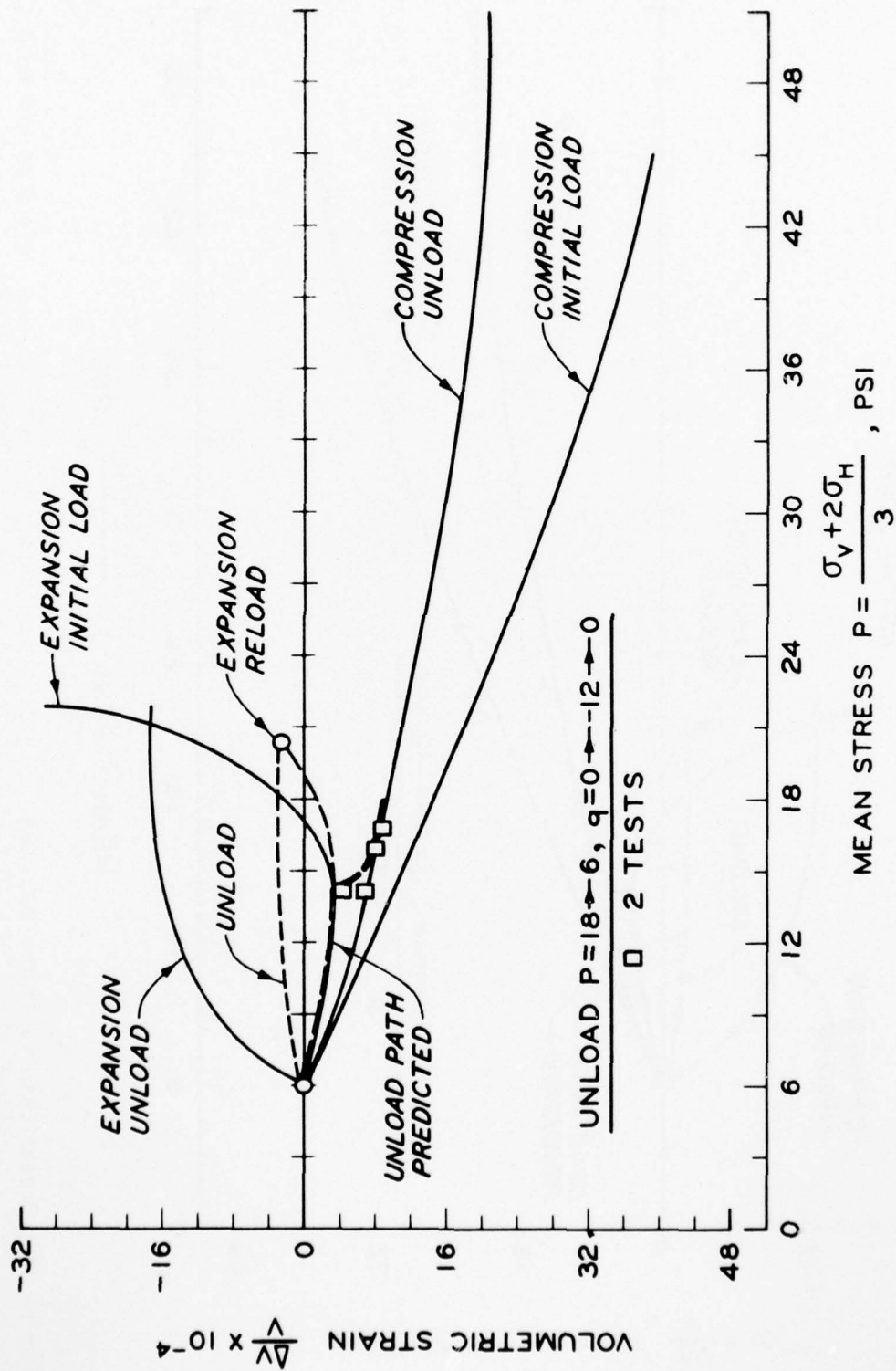
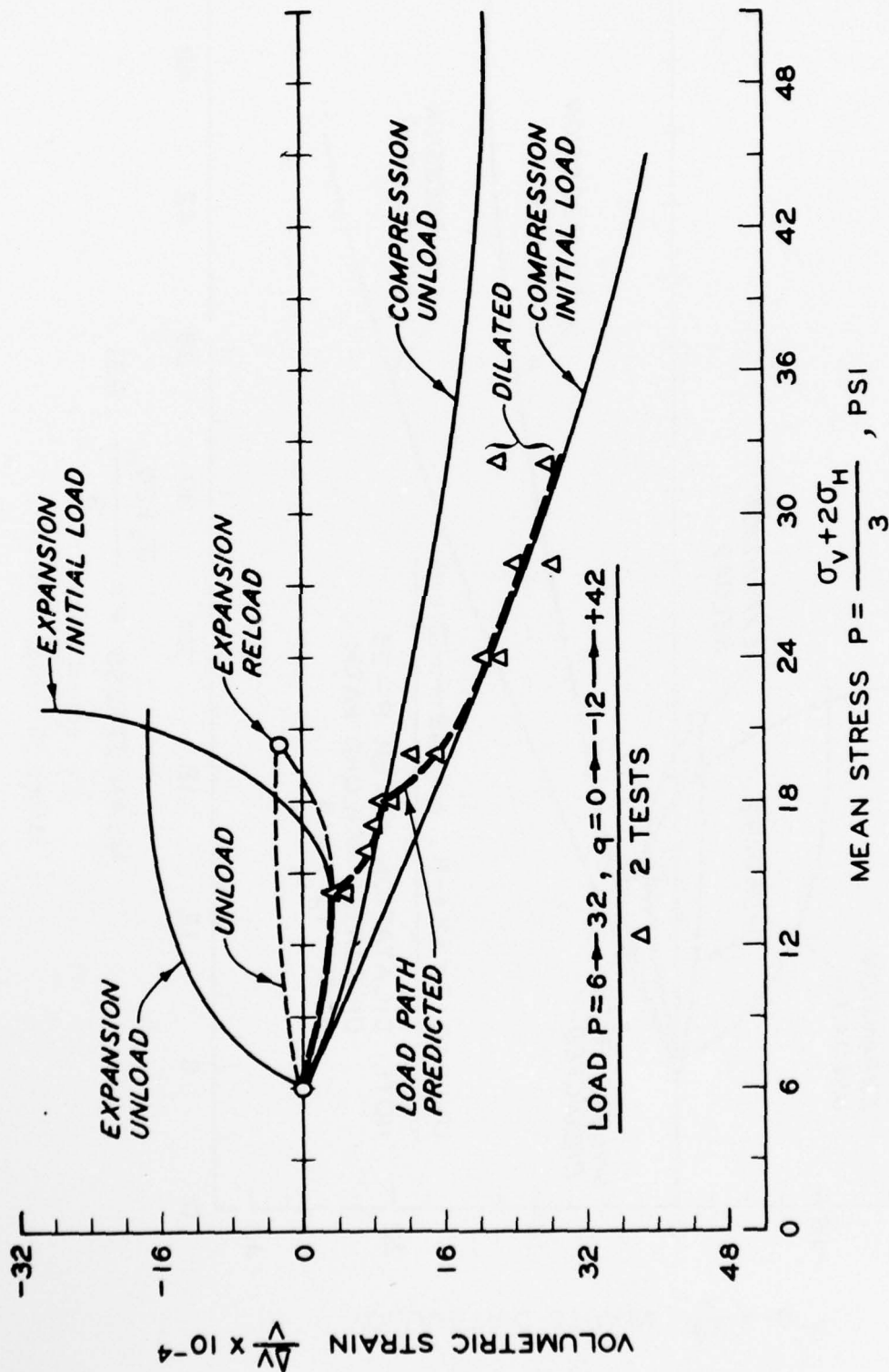


Figure 38. Stress path tests for Reid-Bedford sand: load test,  $P = 6$  to  $18$  and  $q = 0$  to  $-12$  to  $0$ ; unload test,  $P = 18$  to  $6$  and  $q = 0$  to  $-12$  to  $0$  (sheet 1 of 2)



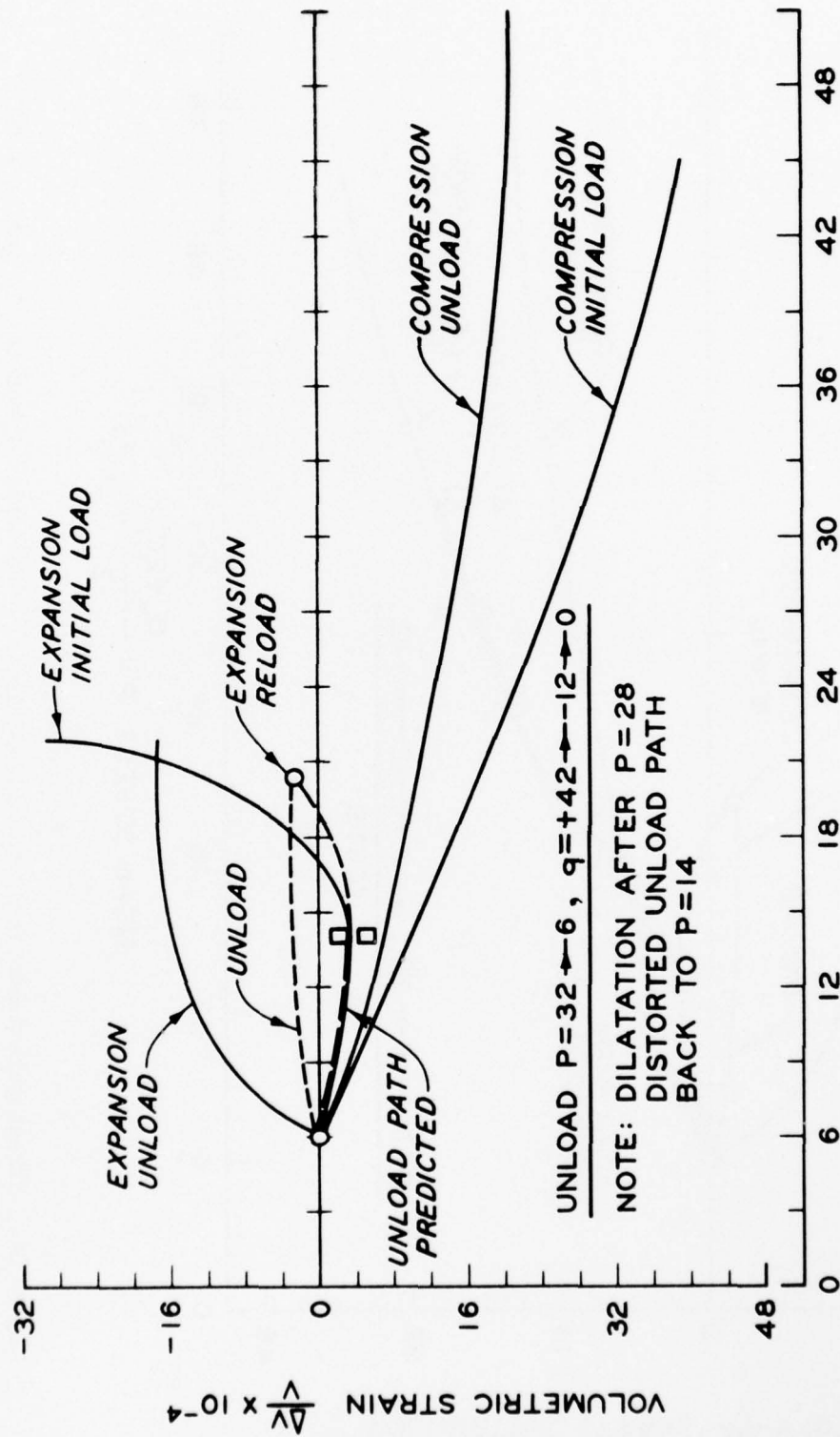
b. Unload test

Figure 38 (sheet 2 of 2)



a. Load test

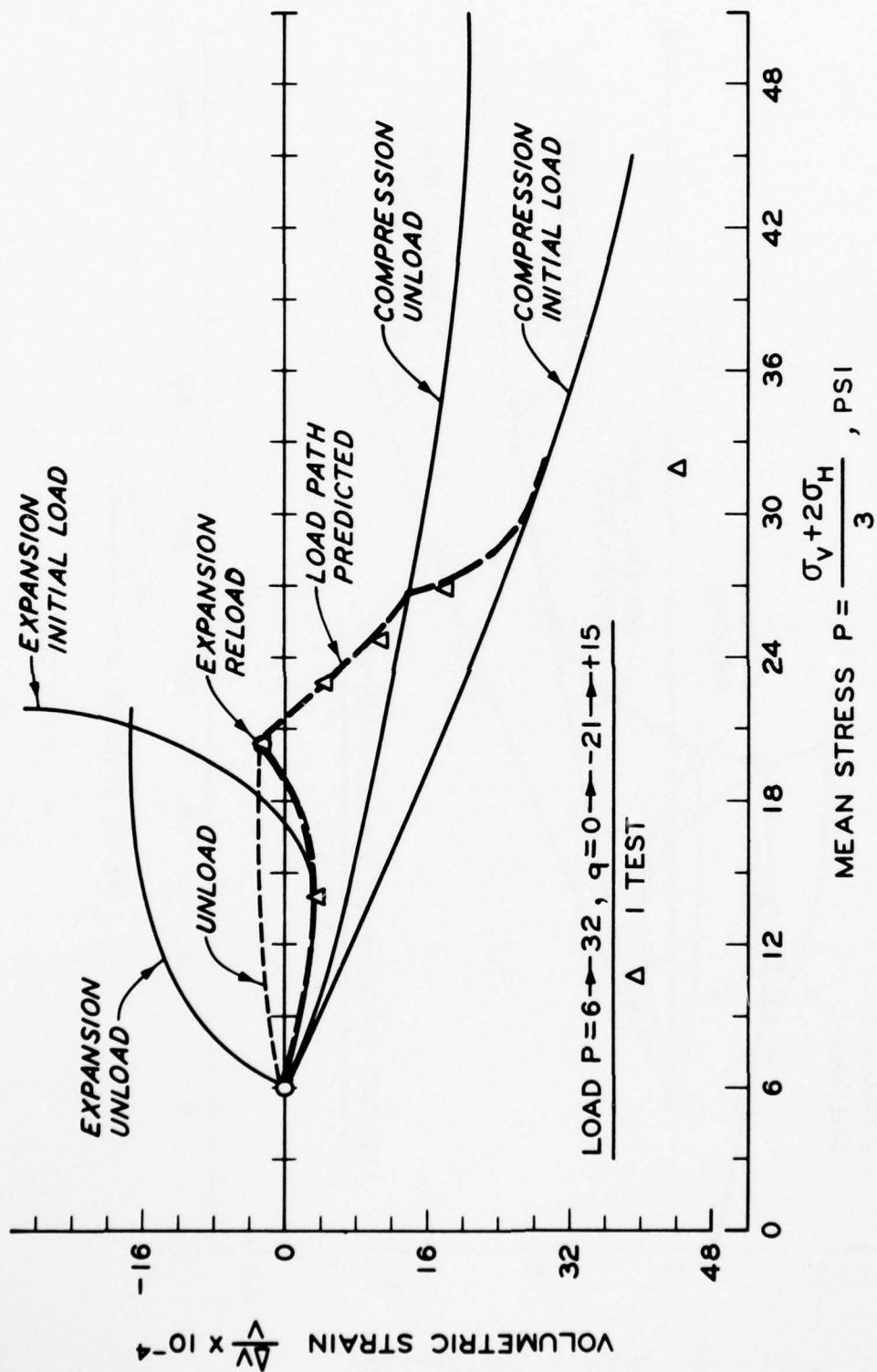
Figure 39. Stress path tests for Reid-Bedford sand: load test,  $P = 6$  to  $32$  and  $q = 0$  to  $-12$  to  $+42$ ; unload test,  $P = 32$  to  $6$  and  $q = +42$  to  $-12$  to  $0$  (sheet 1 of 2)



$$\text{MEAN STRESS } P = \frac{\sigma_V + 2\sigma_H}{3}, \text{ PSI}$$

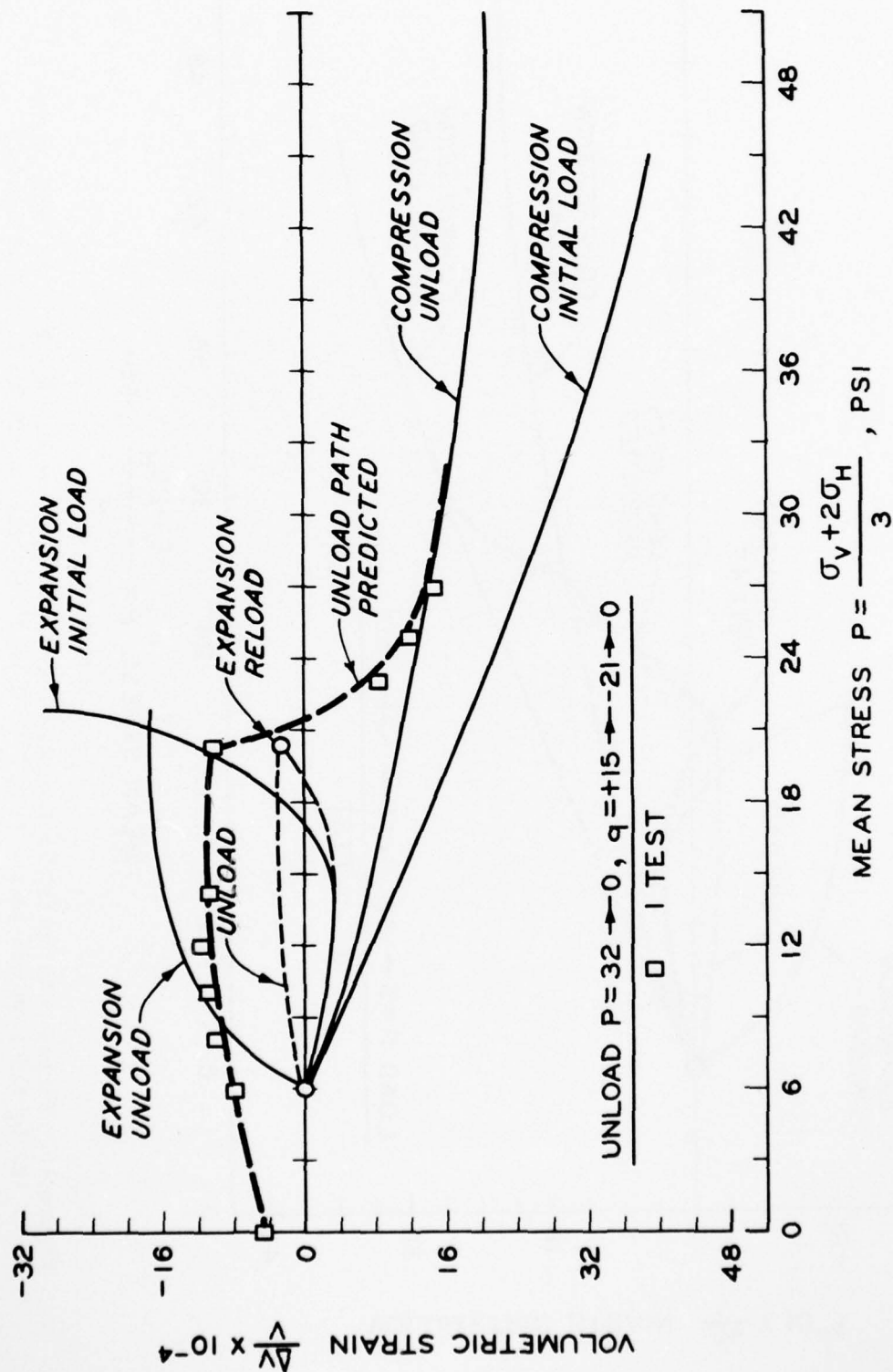
b. Unload test

Figure 39 (sheet 2 of 2)



a. Load test

Figure 40. Stress path tests for Reid-Bedford sand: load test,  $P = 6$  to  $32$  and  $q = 0$  to  $-21$  to  $+15$ ; unload test,  $P = 32$  to  $0$  and  $q = +15$  to  $-21$  to  $0$  (sheet 1 of 2)



b. Unload test

Figure 40 (sheet 2 of 2)

continued unloading of path 2 from  $P = 6$  and  $q = 0$  to  $P = 0$  and  $q = 0$ , as shown in Figure 40b.

104. Figure 41 shows a comparison of the sand and loess characteristic response curves in the  $P-\Delta V/V$  plane. Similarities of the  $P-q - \Delta V/V$  model for both  $C$  and  $\phi$  materials and  $\phi$  materials are obvious. Figure 42 shows a comparison of the sand and loess characteristic response curves in a  $\Delta P-\Delta V/V$  plane. (The  $\Delta P-\Delta q - \Delta V/V$  model was previously shown to exist for the sand test.)

105. Discussion in the previous section concerning the invariant nature of  $\Delta V/V$  pointed out that load  $\Delta V/V$  should be unique whether for initial loading or reloading. Figure 43 shows compression  $\Delta V/V$  in percent of total  $\Delta V/V$  versus  $\Delta P$  for both sand and loess. As can be seen on a normalized basis,  $\Delta V/V$  is the same for both initial load and reload. Only two invariant  $\Delta V/V$  curves exist: load and unload. The burette data curve for the sand is shown, and it resulted in only one curve falling between the LVDT load and unload curves. As previously discussed, the burette data were affected by test conditions. However, as can be seen in Figure 43, the burette responses also validate the  $P-q - \Delta V/V$  model. The burette data are only shifted and averaged by the test conditions.

106. Figure 43 is interesting, because both the sand and loess characteristic response curves are exactly the same on a normalized basis. This means that the  $P-q - \Delta V/V$  model is the same for both a  $\phi$  and  $C$  soil and a  $\phi$  soil. The characteristic response curves are only spread differently because of the different strengths of the sand and loess. The sand and loess models being the same may be only a coincidence; however, it is a very interesting occurrence.

107. Figure 44 shows  $\Delta P$  in percent of total  $\Delta P$  versus initial expansion  $\Delta V/V$ . The sand and loess initial expansion curves are the same on a normalized basis. Sand burette data for expansion are also shown.

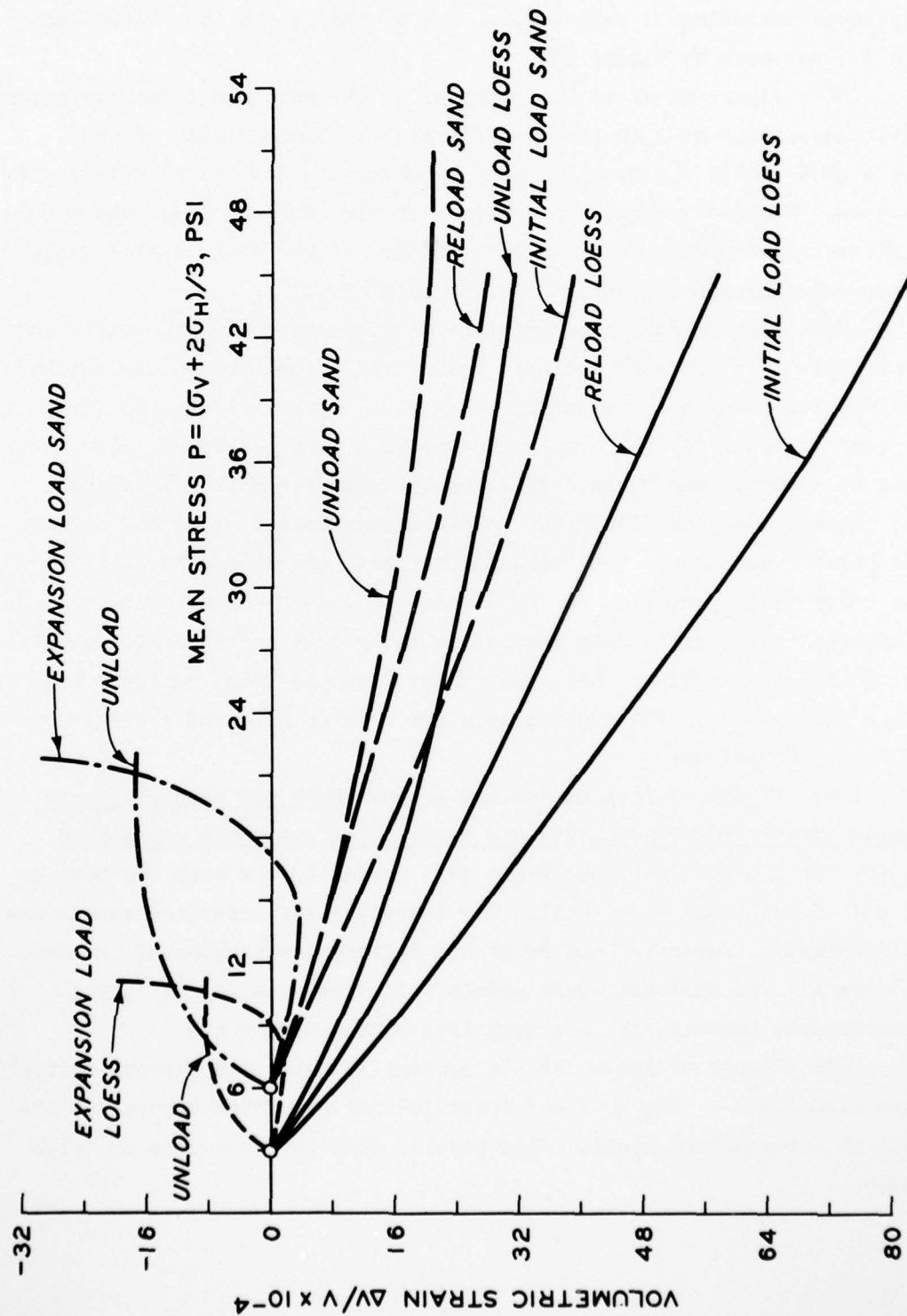


Figure 41. Loess and sand comparison on  $P-\Delta V/V$  plane

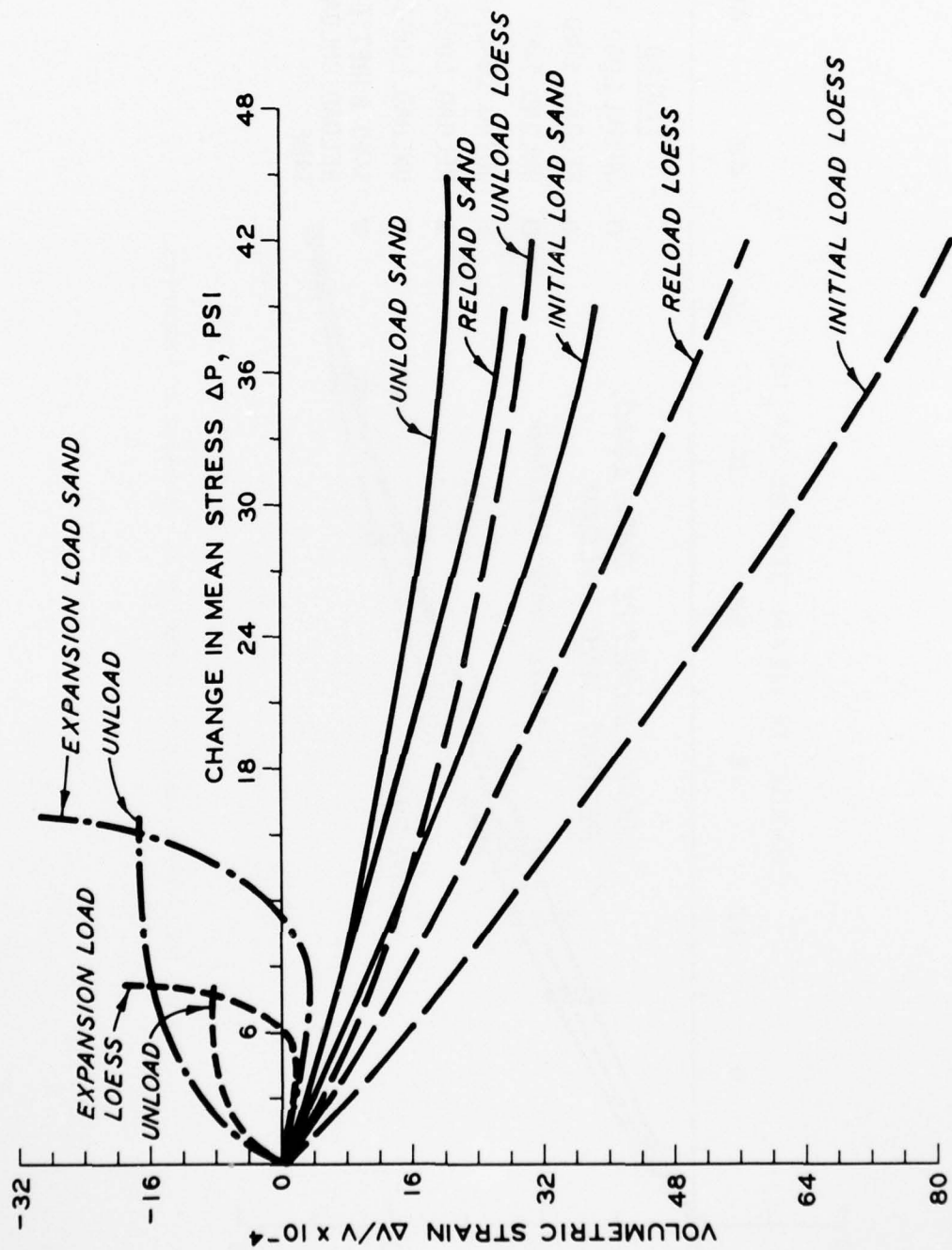


Figure 42. Loess and sand comparison on  $\Delta P$ - $\Delta V/V$  plane

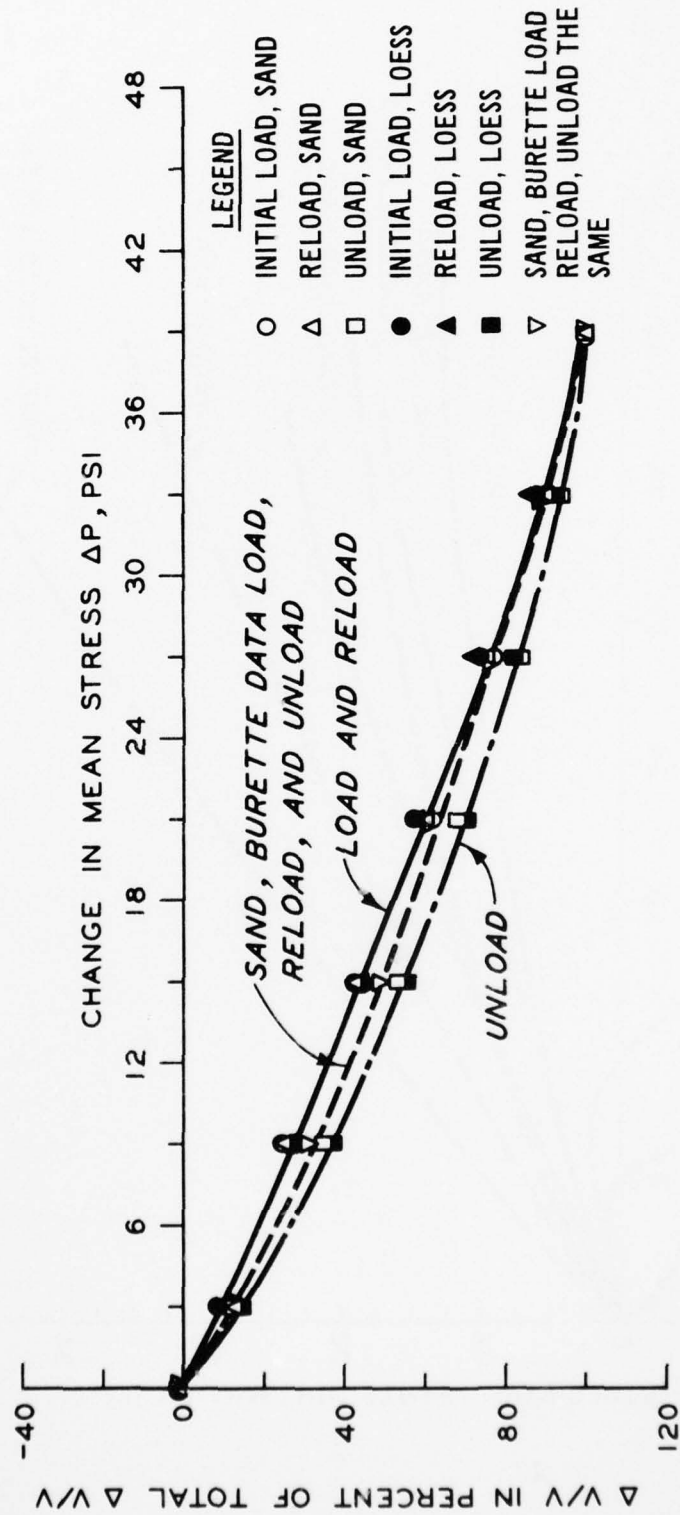


Figure 43. Loess and sand normalized compression comparison

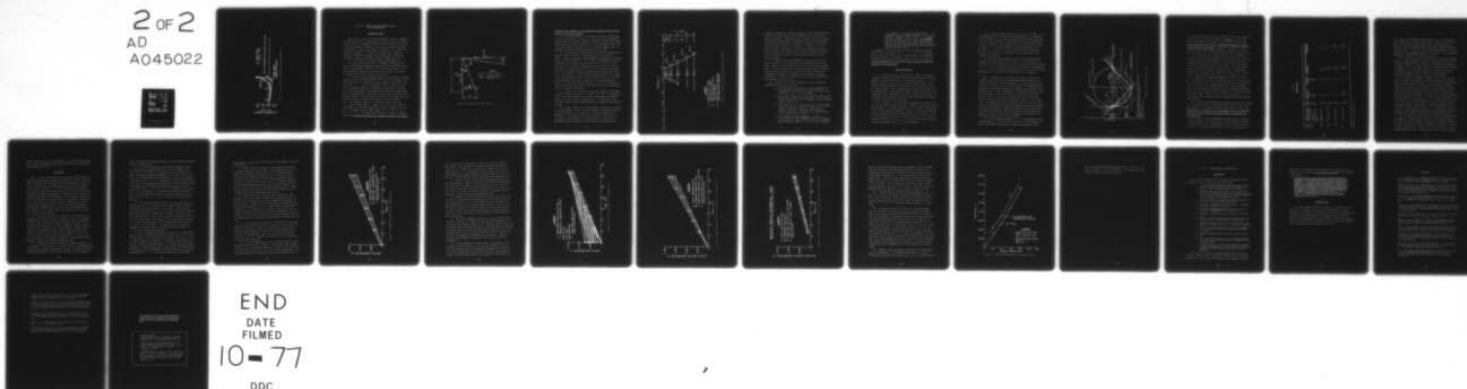
AD-A045 022

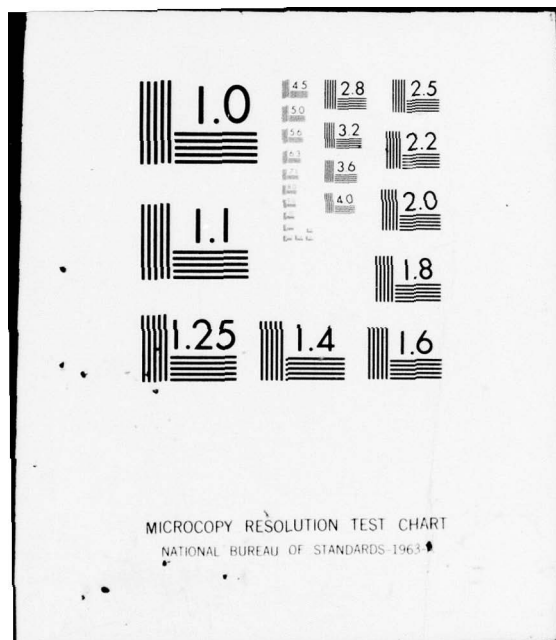
ARMY ENGINEER WATERWAYS EXPERIMENT STATION VICKSBURG MISS F/G 8/13  
GENERAL DEFORMATION (ELASTIC AND INELASTIC) AND STRESS DISTRIBUTION--ETC(U)  
SEP 77 R H LEDBETTER  
WES-TR-S-77-10

UNCLASSIFIED

NL

2 OF 2  
AD  
A045022





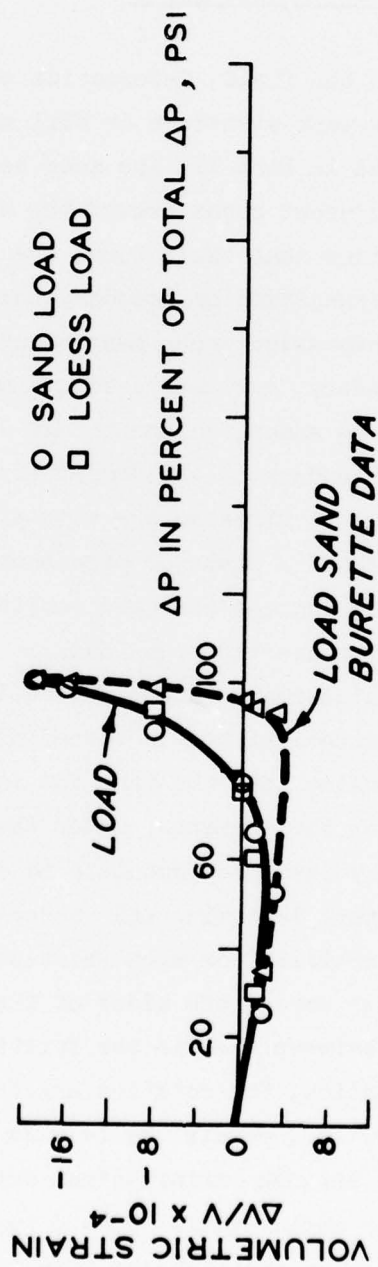


Figure 44. Loess and sand normalized expansion comparison

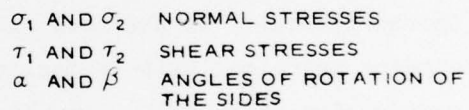
PART IV: GENERAL DEFORMATION MODEL APPLIED  
TO FIELD CONDITIONS

Deformation Zones

108. Consider that, in the field, deformation zones of compression and expansion exist in a pavement structure or soil mass for a loaded wheel or plate. As presented in Part II, the zone beneath a wheel has compressive movements and adjacent zones around the wheel have expansive movements. Also, consider that these zones are of volumetric compression and expansion. A transition or boundary that separates volumetric compression and expansion zones must exist. Within the transition or along the boundary, volumetric change must be zero.

109. For a state of pure shear, volume change equals zero,  $\Delta V = 0$ . At this deformation boundary in a pavement structure or soil mass, the load-induced principal stresses are adjusting themselves such that no volume change occurs and a state of pure shear exists. Past the deformation boundary, the induced stresses continue to dissipate or distribute with offset distance from the load.

110. Consider an infinitesimal element at the deformation boundary. Figure 45 shows a two-dimensional view of a corner of the element. The third stress is in the dimension into the page and is adjusting so that pure shear,  $\Delta V = 0$ , acts on the element. Under the action of pure shear, the element deforms by the sides rotating as shown. Consider that the element material stops deforming and reaches equilibrium when the frictional strength is mobilized or when friction is supporting the material structure. In other words, the sides of the element will rotate or distort until the angle between them is the friction angle  $\phi$  as shown. For symmetric distortion, the rotation angles are equal,  $\alpha = \beta$ , and the shear angle,  $\gamma$ , equals  $2\alpha$  ( $\gamma = 2\alpha = 2\beta$ ), which is the decrease of right angle between infinitesimal orthogonal line segments. Therefore, the shear angle equals  $90 - \phi$  ( $\gamma = 90 - \phi$  and  $\alpha = \beta = 45 - \phi/2$ ). The element side labeled 1 in Figure 45 therefore becomes the deformation boundary which separates the zones of volumetric



95

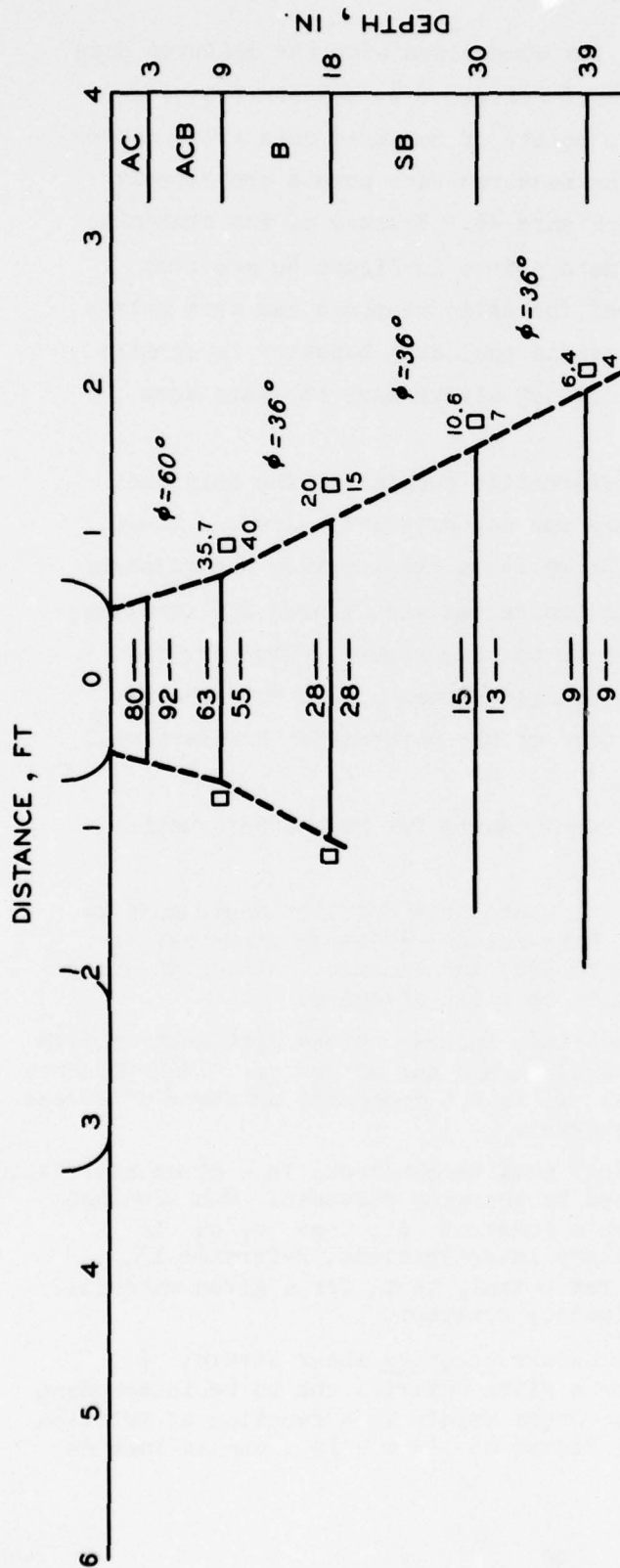
compression and expansion. This deformation boundary is not a failure plane or a discontinuity plane.

111. As developed above, the deformation boundary is controlled by the friction angle of a material. For extension of the deformation boundary through a material, consider a series of infinitesimal elements being connected along the rotated side,  $l$ , of each element. When a soil or soil type changes with depth, the friction angle changes, and the deformation boundary therefore changes direction or angle.

112. The deformation boundary separates volumetric compression and expansion zones. Therefore, it separates positive and negative  $q$  spaces. This also means the boundary separates zones where the principal axes are inclined differently. As is obvious, the deformation boundary corresponds to the change of principal axis line in the  $P-q - \Delta V/V$  model and occurs where the principal axes are at  $\pm 45^\circ$  to the vertical and horizontal (discussed in Part III). In the zone on the compressive side of the boundary, the major principal axis is inclined less than  $45^\circ$  to the horizontal. In the zone on the expansion side of the boundary, the major principal axis is inclined less than  $45^\circ$  to the vertical. On the compressive side of the boundary, the major principal axis rotates to the horizontal directly beneath a load. For the expansion side of the boundary, the major principal axis rotates, with increasing offset distance, to the vertical.

113. Consider, now, how such a deformation boundary as discussed above can possibly be verified or located in the field. One possibility might be to observe the points or locations where measured movements within layers pass through or approach zero. In other words, locate, in layers, the zero points separating measured compressive and expansive movements.

114. Figure 1 shows the flexible pavement structure for the field tests of References 3 and 8. The base, subbase, and subgrade materials are gravelly sands. By locating the zero points of measured layer movements in the appendix of Reference 8 (Figure 9 of this report is an example of layer movements from Reference 8), the points can be plotted as shown in Figure 46. Friction values and the predicted



### LEGEND

- PREDICTED AVG STRESS
- - - MEASURED AVG STRESS
- ZERO DEFORMATION POINTS (FIELD MEASURED)
- · - · - PREDICTED ZERO DEFORMATION AND STRESS DIST. BOUNDARY

Figure 46. Measured and predicted deformation boundary

deformation boundaries are shown for comparison with the measured data. The data are for the winter tests of Reference 8, and the friction values are estimates. Exact zero points of measured data are a matter of individual interpretation. The measured zero points are closely distributed around the points in Figure 46. Because of the constant nature of elastic response, the data points in Figure 46 are from elastic behavior. The majority of inelastic response had zero points at the same locations. However, since inelastic behavior is erratic when load history is random, it did not always have the same zero points as elastic.

115. Figure 46 shows the deformation boundaries for only one wheel. The inner or left boundary was not extended below the 18-in. depth, because below this depth there is an overlap from the adjacent wheel. Overlap or combination of boundaries and deformation zones has not been studied by the author prior to this report. However, the combination of boundaries and deformation zones should not present complications. Further verification of the deformation boundary will be presented in the next section.

116. Consider some of the requirements for such a deformation boundary to exist in soil materials.

- a. For a given material state, the friction angle must be fairly constant. Mohr-Coulomb criteria show that  $\phi$  is generally well behaved and constant until high stress intensities cause it to begin changing.
- b. For a layer of material, induced stress distribution with depth (stress change) should not affect  $\phi$ . Mohr-Coulomb criteria show that  $\phi$  is not dependent on state of stress except at high stresses.
- c. Stress ratio  $\sigma_1/\sigma_3$  must be constant, in a given material, and not be affected by changing stresses. Mohr-Coulomb criteria show, for a constant  $\phi$ , that  $\sigma_1/\sigma_3$  is constant. Laboratory investigations, Reference 13, involving stress ratio imply that, for a given material,  $\sigma_1/\sigma_3$  is approximately constant.
- d. The deformation boundary requires shear strain,  $\delta$ , to be constant for a given material and to be independent of stress change. Shear strain is a function of friction angle as shown in Figure 45 ( $\delta = \epsilon/L$ ), and as long as

$\phi$  is constant  $\delta$  is constant. Shear stress,  $\tau$ , is changing with stress change, but shear strain,  $\delta$ , is constant. Therefore, shear modulus,  $G$ , is changing with stress changes,  $G = \tau/\delta$ , and is not constant. Reference 14 shows that shear strain is approximately constant for a constant stress ratio (item c above). This item, d, also shows that stress ratio is constant. (Shear strain being constant requires stress ratio to be constant, and vice versa.)

As a summary of the above items (a to d), the deformation boundary requires, for a given soil, that  $\phi$ ,  $\sigma_1/\sigma_3$ , and  $\delta$  be constants until high stress intensities cause them to change. The deformation boundary derived above and shown in Figures 45 and 46 indicates the frictional properties of a soil can be fully acting even though the material is not near failure.

#### Stress Distribution

117. Consider that, for a loaded wheel or plate, the confined compression zone, which is defined and circumscribed by the deformation boundary, is supporting the load. At the surface, depth  $Z = 0$ , the vertical stress,  $\sigma_v$ , acting is the major principal stress (if the wheel is not moving) and is the load divided by the contact area of the wheel or plate. With increasing depth, the major principal stress is decreasing due to the increasing volume of material and larger areas along which it acts and rotates. Along a horizontal plane, within the compression zone, at depth  $Z$ , the principal stress has been reduced by the larger area than at the surface.

118. At depth  $Z$  directly beneath the surface load contact area, the major principal stress is vertical. Adjacent to the surface contact area at depth  $Z$ , the major principal axis is rotating from horizontal to  $45^\circ$  at the deformation boundary. At depth  $Z$ , the major principal stress acting at the surface has been reduced by the proportion of the areas of horizontal planes at the surface and depth  $Z$ . By using the constant stress ratio,  $\sigma_1/\sigma_3$  or  $\sigma_v/\sigma_H$ , for the material at depth  $Z$ , the minor principal stress,  $\sigma_H$ , can be determined.

119. Once the principal stresses ( $\sigma_V$  and  $\sigma_H$ ) at depth  $Z$  for the compression zone are known, the vertical stress,  $\bar{\sigma}_V$ , component can be determined at the deformation boundary where the principal axes are  $\pm 45^\circ$  to the horizontal. In other words, by knowing the principal stresses at depth  $Z$ , Mohr's stress circle can be developed as shown in Figure 47. A rotation (as shown) of the principal axes of the circle, to  $\pm 45^\circ$  from the horizontal, gives the stress components, at the deformation boundary, on vertical,  $\bar{\sigma}_V$ , and horizontal,  $\bar{\sigma}_H$ , planes of the material.

120. The deformation boundary is also the stress distribution boundary where the principal axes are at  $45^\circ$  to the horizontal and vertical. From the boundary and in toward the load, the major principal axis rotates to the horizontal, and the inclosed zone is in compression,  $\sigma_V > \sigma_H$ . From the boundary and away from the load, the major principal axis rotates to the vertical, and the material is in expansion,  $\sigma_H > \sigma_V$ .

121. Verification of the deformation and stress distribution boundary can be achieved with field-measured vertical stresses. For the flexible pavement tests of Reference 8, the tire footprint had a length of 24 in. and a width of 12 in. and the load averaged 28,073 lb per wheel with a standard deviation of 2,990 lb. The compression zone beneath this tire is an odd-shaped cone intersecting the surface along the circumference of the tire footprint. Computing the vertical stresses beneath the tire and at the boundary, as described above, gave the predicted values shown in Figure 46 ( $\sigma_H/\sigma_V = 1 - \sin \phi$  was used). The measured values are from Reference 8 for the winter tests. As for the zero deformation points, the measured stresses are subject to individual interpretation concerning the exact values at points along the distribution boundary. These field vertical stresses were measured with 1-in.-diam and open-face diaphragm SE soil pressure cells (briefly described in Part II of this report).

122. For a frictionless material,  $\phi = 0$ , the deformation boundary development in the last section indicates that the decrease of right angle between infinitesimal orthogonal line segments is  $90^\circ$ .



This means one side has rotated into the other side. Logic, therefore, implies that the deformation boundary is vertical. For the summer tests of Reference 8, the asphaltic concrete (AC) was hot, and the vertical stress below the 9 in. of AC was approximately the applied vertical stress on the surface. Naturally, the boundary of Figure 46 moved inward and measured values increased. Apparently the AC lost friction strength by the hot asphalt lubricating the aggregate surfaces.

123. As is obvious, the deformation and stress distribution boundary can be verified by measured zero deformation points in layers and/or by measured vertical stresses. For field tests where layer movements were not measured, measured vertical stresses can be used to verify the compression zone and its boundary. The test flexible pavement structure of Reference 2 had 6-in.-diam stress-averaging chamber WES soil pressure cells (briefly described in Part II of this report). These pressure cells were at various depths from 9 in. to 12 ft. Load-induced stresses were transmitted through 3 in. of AC, 6 in. of crushed stone, 24 in. of gravelly sand, 36 in. of heavy clay, and 75 in. of lean clay. Table 1 gives predicted and measured vertical stresses below the center of single-wheel (SW) loadings (footprint 24 by 12 in.) and at the deformation and stress distribution boundary. The second column of Table 1 gives the material type above the pressure cell at each depth. Also given in the second column of Table 1 are the friction angles (estimated) used to establish the boundary through the materials.

124. Variation between measured and predicted values for the largest load can be observed. The variation should be due to the friction angle changing at high loads, as shown by Mohr-Coulomb criteria. An important point to be made is that the measured stresses of Figure 46 and Table 1 were obtained with different (type and operating) soil pressure cells.

125. Vertical stress measurements were made below the center of a SW 30-kip load on the crushed stone test section briefly described in Part II for Figure 14. The measured vertical stress at the bottom of the 21 in. of crushed stone averaged  $25 \pm 3$  psi, as measured by

Table 1

MWHGL Tests\*

Depth ft	Material Above Pressure Cells	SW Load kips	Vertical Stress at C, psi		Vertical Stress at Boundary, psi	
			Predicted	Measured	Predicted	Measured
0.75	3-in. AC, 60° and 6-in. crushed stone, 50°	15 30 50	28 56 93	26 60 80		
2.75	Gravelly sand, 40°	15 30 50	7 14 24	7 15 19	5 10 16	5 6 12
4.50	Heavy clay, 16°	15 30 50	3 5 8	3 7 11	2.6 4.3 7.0	1.5 3 4
7.50	Lean clay, 26°	15 30 50	1 2 3	1 2 3	0.8 1.6 2.3	0.2 0.5 1
12	Lean clay, 26°	15 30 50	0.4 0.8 1.3	1 1 2	0.3 0.5 1.0	0.0 0.5 0.7

\* Reference 2, test item 3

6-in.-diam stress-averaging chamber pressure cells. By estimating a friction angle of  $50^\circ$  for the crushed stone, a prediction of 20 psi is made. The variation between measured and predicted values can be accounted for by the friction angle being slightly larger and measurement variation. As should be obvious, measuring stresses in or at the interface of large aggregate materials is difficult. The measurements usually have variations of several units of psi.

126. The previous field test results were for flexible pavements. Asphaltic concrete appears to behave as a highly cohesive soil with a frictional strength that may be high or low, depending on temperature. The asphalt content also causes viscoelastic behavior that is dependent on temperature. In other words, asphaltic concrete may behave as a high-friction material, such as crushed stone and sand, but with temperature-dependent cohesion added by the asphalt binder.

127. Consider a comparison of asphaltic concrete and portland cement (PC) concrete; both materials can have cohesion and high frictional strength. However, there is a basic difference between the two materials. As shown in the previous field test results, asphaltic concrete is not distributing stresses as a solid material. Portland cement concrete does distribute stresses as a solid type material (PC concrete beams, for example). In other words, the stress distribution boundary does not exist in PC concrete, and it behaves more as a solid material in stress distribution. As PC concrete solidifies from a fluid type state, internal crystals form and strong particle and crystalline (chemical) bonds develop. These strong particle bonds do not exist in soil or asphaltic concrete. In other words, soils and asphaltic concrete materials cannot carry or distribute the high shear stresses that PC concrete can distribute and internally sustain.

128. PC concrete pavement slabs do not have the stress distribution boundary. However, once the loads or stresses pass through the PC slabs into the soil foundation materials, the boundary develops in the soil, and the soil behaves as described in this report. This is verified by Reference 8, in Figures 11 and 13 of this report, and in unreported WES test data. As discussed in Part II, the soil behavior

below a slab does affect the slab response. For lack of better description, stress distribution through a PC concrete slab acts as very large plate loading on the soil.

#### Field Tests

129. A series of field tests was conducted at the site where the undisturbed loess sample, characterized in Part III of this report, was taken. The field tests were plate load and vibratory load tests, both on 30-in.-diam plates. A standard plate load test, which is only increasing load, was conducted. Out of the influence of the standard test, a cyclic plate load test was conducted. The cyclic test was run by loading, unloading, and reloading to a higher load for several steps. Vibratory load tests were conducted out of the influence of the above tests. The WES 16-kip portable (housed in a semitrailer) vibrator was used. This vibrator will produce vibratory loading from 0-15,000 lb at frequencies ranging from 5 to 100 Hz, thus producing a combined static plus peak dynamic load of 31 kips. The loess vibratory tests were conducted at 15 Hz with dynamic load ranging from 0 to 8.4 kips plus a static load of 16 kips.

130. In order to predict field behavior of the above tests, the deformation and stress distribution boundary is needed. The boundary will define the confined compression zone and the stress distribution below the 30-in.-diam plates. Once the boundary is defined, states of stress for the various loads can be determined. Beneath plate loads in the confined compression zone, the stress path is always in the positive  $q$  space and is the path shown in Figure 18. Obviously, once the states of stress and path are determined, the  $\Delta P - \Delta q - \Delta V/V$  model for the loess can be used to predict the load, unload, and reload volumetric strains of the confined compression zone.

131. Consider that the volume within the confined compression zone is changing as  $\Delta V/V$  predicts. In order to reflect the changing volume, there is only one degree of freedom for movement. The degree of freedom is vertical; therefore, volume change within the confined compression

zone is reflected at the surface, beneath the load, by vertical displacement of the loaded plate.

132. For a 30-in.-diam plate, the confined compression zone is a truncated cone intersecting the surface at the periphery of the plate. The cone is defined and circumscribed by the deformation and stress distribution boundary as described in the first section of this part. As previously defined, the boundary is inclined to the vertical at an angle of  $45 - \phi/2$ ;  $\phi$  is approximately  $26^\circ$  for the loess, given in Part III. For various loads on the plate, the major principal stress at any depth can be determined as defined in the previous section. A stress ratio  $\sigma_H/\sigma_V = 1 - \sin \phi = 0.56$  in the loess was used to determine  $\sigma_H$  at various depths. As described in the previous section,  $\sigma_V$  and  $\sigma_H$  are the principal stresses acting within the zone at a given depth. From  $\sigma_V$  and  $\sigma_H$ ,  $P$  and  $q$  values can be calculated for any depth.

133. For the field tests, average  $\Delta P$  and  $\Delta q$  values were calculated for each 12 in. of depth for every plate loading. The stress distribution calculations were taken to the 60-in. depth where the induced major principal stress  $\sigma_V$  was 0.5 and 2.6 psi for the smallest and largest plate loads, respectively. Average  $\Delta P$  values for the bottom layer, 48-60 in., were 0.4 and 1.9 psi for the smallest and largest loads, respectively. For the 12-in. layer below the 60-in. depth, the  $\Delta P$  value for the largest load became negligible with respect to the  $\Delta V/V$  that it would cause. In other words, the bottom of the compression zone was chosen to be the depth below which average  $\Delta P$ ,  $\Delta q$ , and  $\Delta V/V$  values became negligible.

134. For the standard plate load test and using the loess characteristic initial compression load curve of Figure 42, the  $\Delta V/V$  values for each average  $\Delta P$  of each layer were obtained. The initial, prior to loading, volume of each layer in the compression zone cone was calculated. Using these initial volumes,  $\Delta V$  for each layer and load was calculated. As described previously, only one degree of freedom exists. Therefore, the vertical displacement within each layer can be calculated corresponding to the  $\Delta V$  of each layer. Summation of the vertical

displacements of each layer gives the vertical displacement of the plate at the surface.

135. Figure 48 shows the comparison of predicted and measured (dial gage) displacements of the plate. The standard plate load test is conducted by increasing and holding the load at increasing levels. After dial gage movement essentially stops for a load, the load is increased to the next level. In other words, approximate equilibrium of motion is achieved for each load. Some of the variation between predicted and measured response could be due to the possibility that the time element for each field load should have been larger. Another possible cause for the variation is that the compression zone used in the predictions may have been slightly too large.

136. Cyclic plate load field tests were conducted by loading, unloading to zero, reloading to a larger load, unloading to zero, etc. The loads were held both on and off until approximate equilibrium of motion occurred. Predictions of the plate vertical displacements were made using two approaches in order to further verify the characteristic response model. One approach was to use the initial, prior to any loading, volume for each layer and the initial compression load curve of Figure 42. This was the same procedure followed previously and gave the displacements for each load as if the test was a standard plate load test.

137. As is obvious, for each layer, the volume ( $V_L$ ) under each load can be calculated from the initial volume and  $\Delta V/V$  values. By using the load volume  $V_L$  and  $\Delta V/V$  values from the loess characteristic compression unload curve of Figure 42, the rebound  $\Delta V$  for each load can be calculated. (Use of load volume with unload was discussed in Part III.) Therefore, the rebound vertical displacements of the plate were calculated.

138. The second approach was to use the response model the same way that the load tests were conducted. For the first load increment, the initial prior to loading volumes were used with  $\Delta V/V$  values from the initial load curve, Figure 42, to give the load displacement. The volumes under the first load increment were calculated and used with

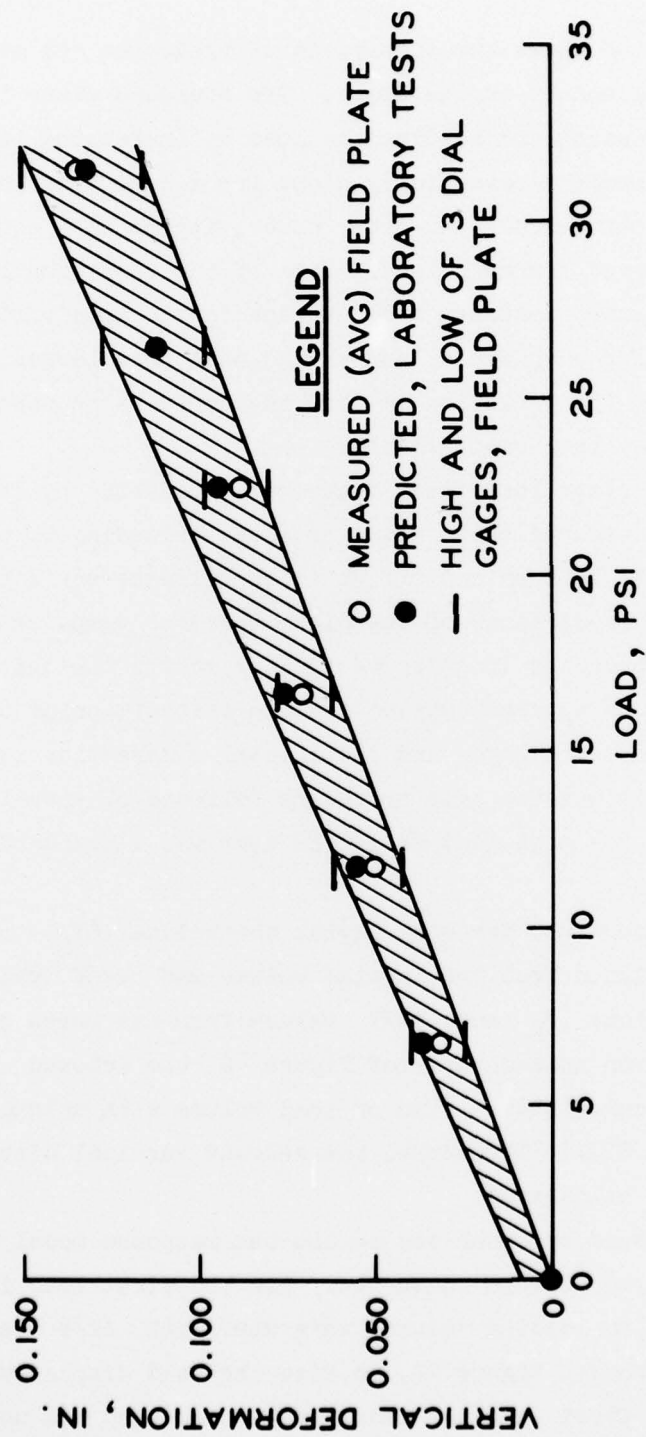


Figure 48. Standard field plate test, Vicksburg loess

$\Delta V/V$  values from the unload curve, Figure 42, to give the rebound displacement. For reloading, the unloaded volume was calculated and used with  $\Delta V/V$  values from the reload curve, Figure 42, to give the reload displacement. (The changing unloaded volume for each load sequence defines the changing reference, discussed previously in Parts II and III.) The above procedures were followed for the remaining cycles.

139. Predicted cyclic load vertical displacements were the same for both approaches. Figure 49 shows the load and unload final displacement points for field-measured and predicted cyclic plate load tests. The actual load and unload paths were not determined in the field, only the end points. However, as should be obvious, the response model will predict the loading and unloading displacement paths.

140. Comparisons between predicted and measured cyclic plate load tests can be better shown by separating the response data into elastic and inelastic behavior. The elastic behavior for both field tests and model predictions is the rebound or unload responses. In other words, for each load sequence the elastic behavior is the difference between the load and final rebound point, which defines the changing reference. Figure 50 shows the predicted and measured elastic vertical displacements of the plate.

141. The inelastic behavior for both the field cyclic load tests and model predictions is obtained by using the changing reference. In other words, the inelastic behavior is the difference between the initial and rebound points for each load sequence. Figure 51 shows the predicted and measured inelastic vertical displacements of the plate. Also shown in Figures 50 and 51 are the field elastic and inelastic behaviors for the last load increment of the standard plate load test. (This was possible because unloaded readings were taken after the last load increment.)

142. Field measurements of plate vertical displacements for the vibratory tests were made with a velocity gage attached to the plate. The velocity gage signals were automatically integrated and plotted in the field simultaneous with conducting the tests. This capability is part of the WES 16-kip vibrator test equipment. The data that are

# LEGEND

- MEASURED (AVG) FIELD PLATE
- - - PREDICTED, LABORATORY TESTS
- , ● INITIAL
- Δ, ▲ LOAD
- , ■ REBOUND
- HIGH AND LOW OF 3 DIAL GAGES, FIELD PLATE

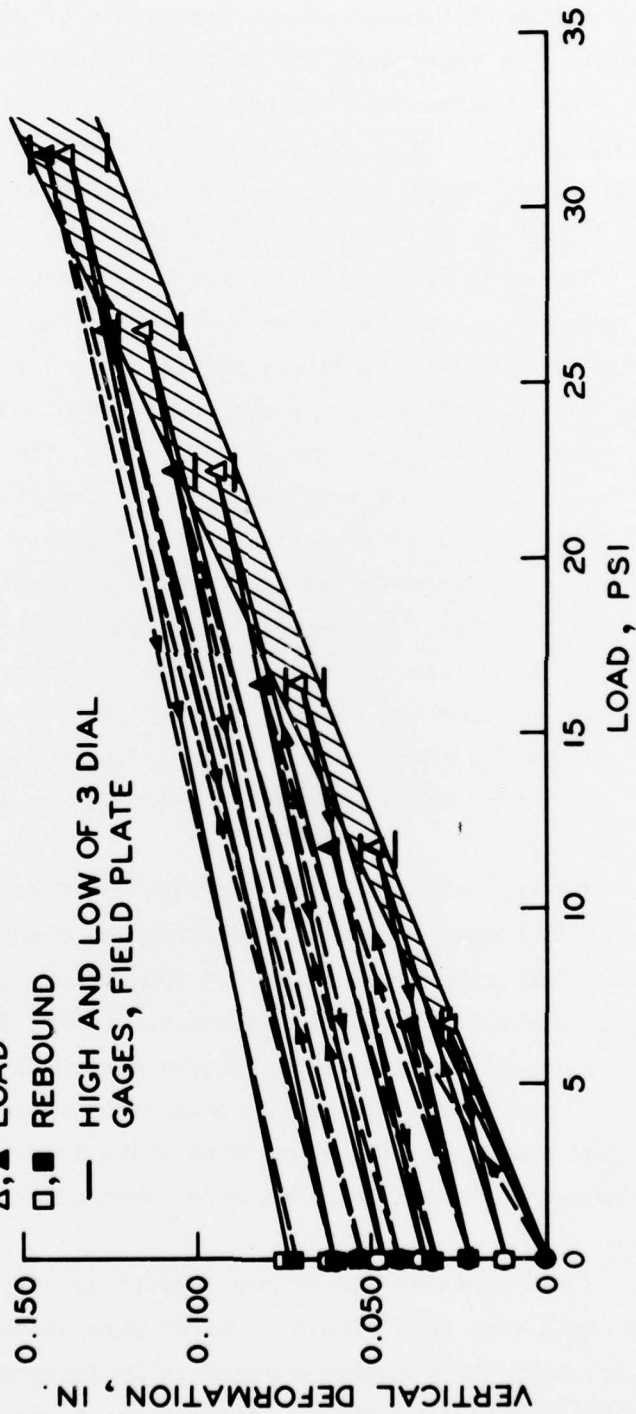


Figure 49. Cyclic field plate test, Vicksburg loess

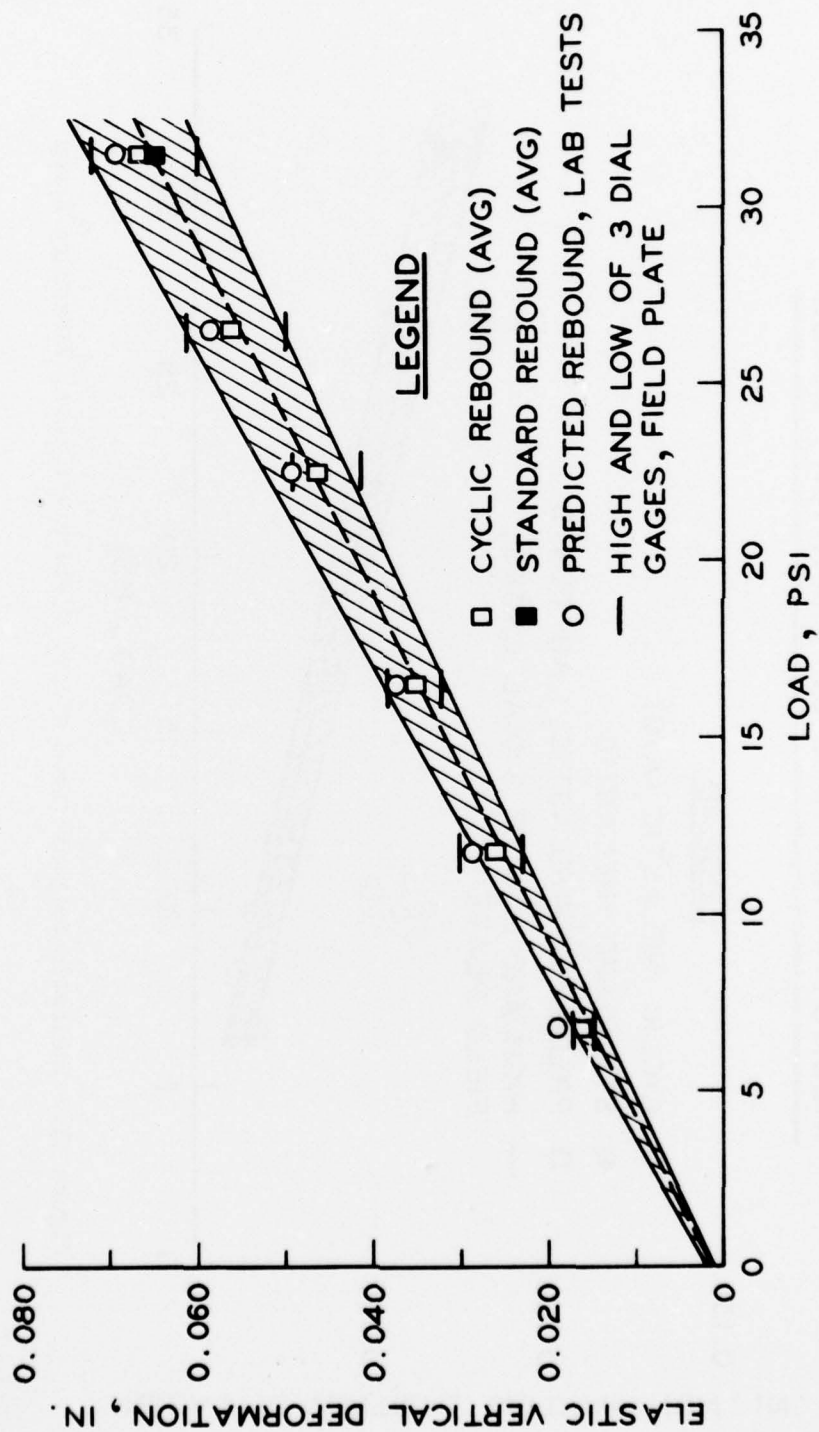


Figure 50. Elastic response from cyclic field plate test, Vicksburg loess

# INELASTIC VERTICAL DEFORMATION, LOESS

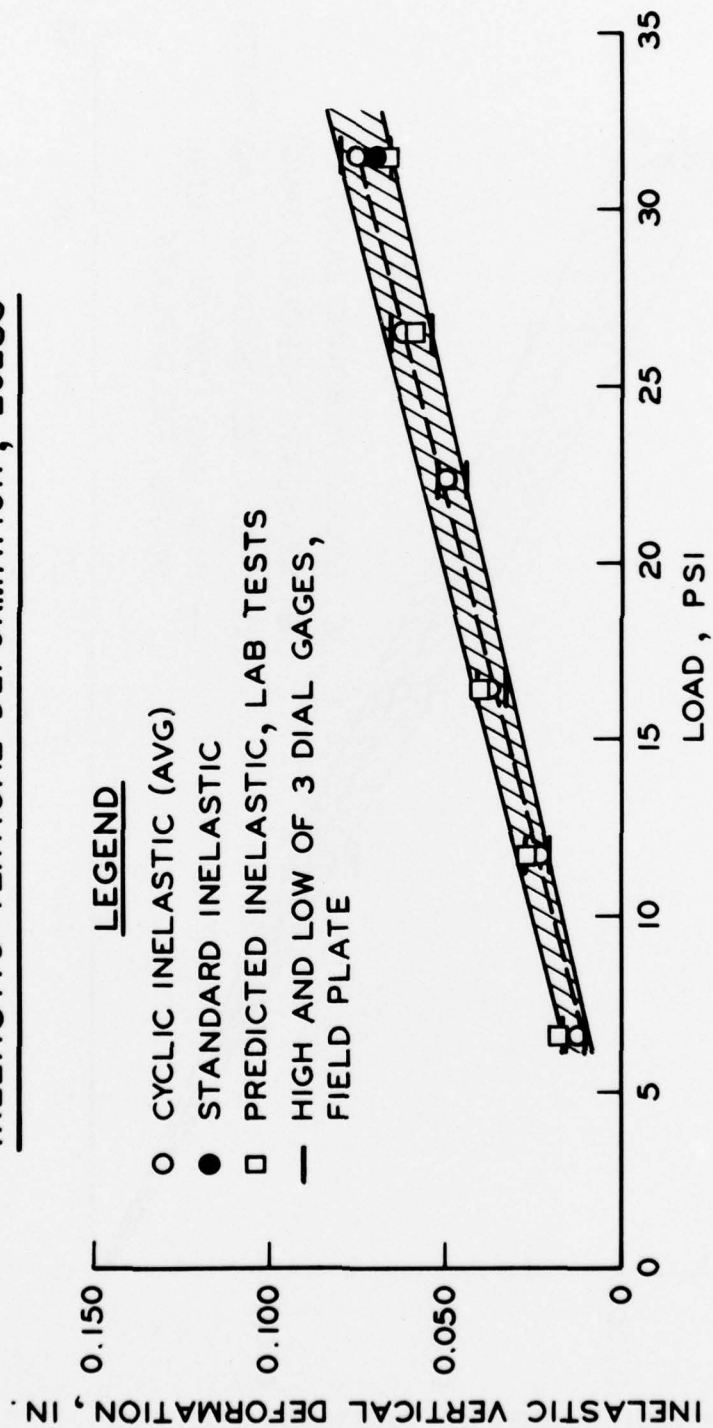


Figure 51. Inelastic response from cyclic field plate test, Vicksburg loess

plotted in the field correspond only to the downward stroke of loading from the 16-kip static load and unloading back to the static load. (Displacement associated with the static load cannot be measured with a velocity gage; therefore, it is not normally measured and was not in these tests.) A load sweep test, which was an automatic increasing dynamic load from 0 to +8.4 kips around the static load while vibrating at 15 Hz, was used. The load sweep took about 2 min, which resulted in approximately 21 cycles per 100 lb of load or 210 cycles per 1000 lb. Therefore, the load sweep test was essentially a steady state test.

143. For predicting the vibratory plate displacements,  $\Delta P$ ,  $\Delta q$ , and  $\Delta V/V$  values for the dynamic loads became negligible below the 48-in. depth. Therefore, for the dynamic loads, the bottom of the compression zone was chosen at the 48-in. depth. The dynamic loads at which  $\Delta P$ ,  $\Delta q$ , and  $\Delta V/V$  values were calculated were 2, 4, 6, and 8 kips.

144. As discussed in Part III for the  $M_R$  test and as shown above for the cyclic plate test, the peak load, static plus dynamic, should be following the characteristic initial load curve, Figure 42, from initial conditions. Unload from and reload to the peak load should be following the characteristic unload curve. For the peak load  $\Delta P$  values, the initial prior to any loading volumes were used with  $\Delta V/V$  values from the initial load curve, Figure 42, to calculate the volumes,  $V_L$ , under each loading. By using the load volumes,  $V_L$ , and  $\Delta V/V$  values corresponding to unloading from peak back to static load from the unload curve, Figure 42, the  $\Delta V$  values for rebound to static were calculated for each loading. Therefore, the rebound vertical displacements of the plate from peak loads back to static load were calculated. These rebound displacements should correspond to the plotted velocity response data for the downward side of the vibratory load (discussed above).

145. Figure 52 shows the predicted and measured (velocity gage) vertical displacements of the vibratory loaded plate. In order to investigate the sensitivity of stress ratio,  $\sigma_3/\sigma_1$ , for the vibratory

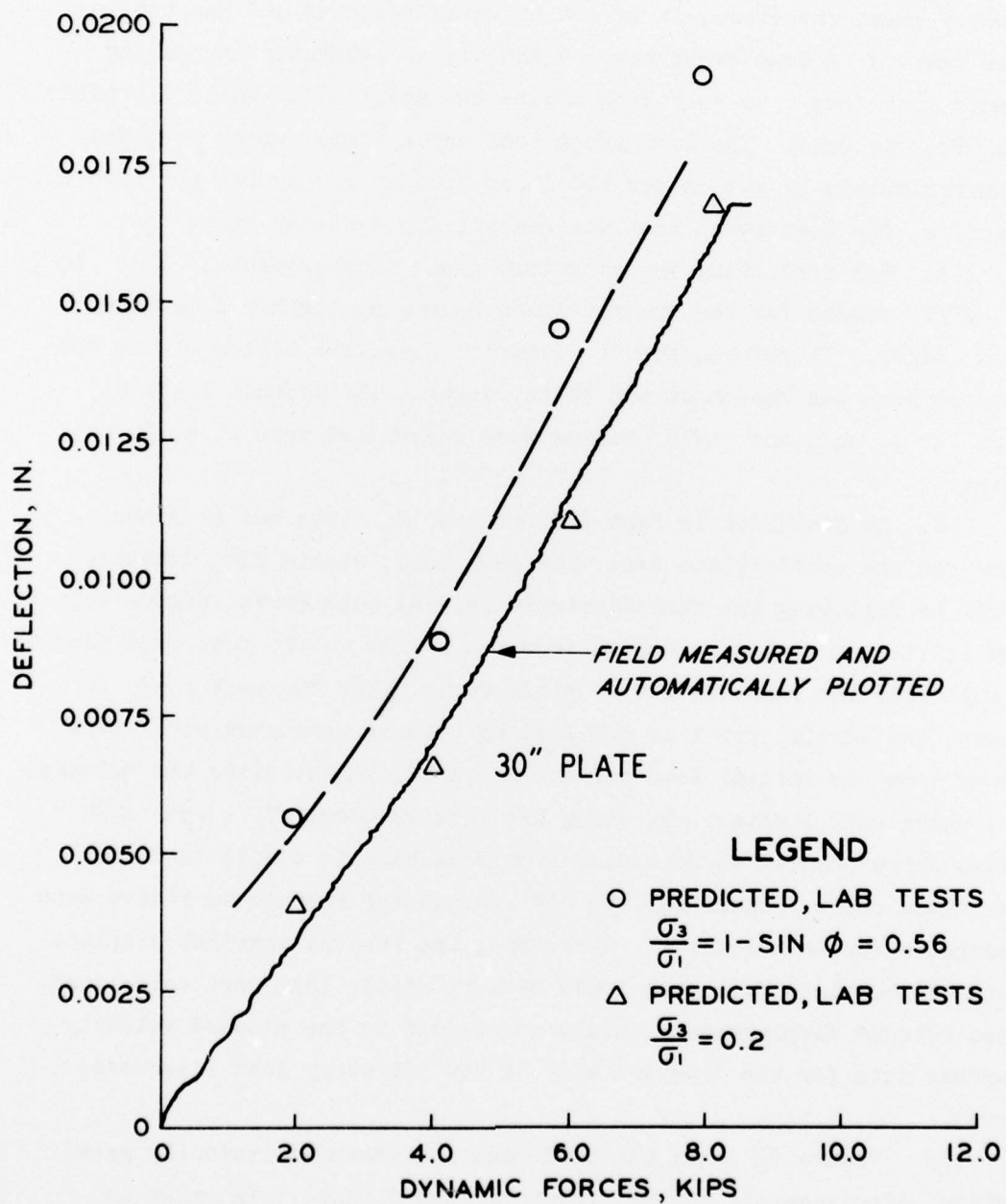


Figure 52. Vibratory field plate test, Vicksburg loess

tests, the displacements were recalculated with  $\sigma_3/\sigma_1 = 0.2$  , as shown in Figure 52. Also, the different stress ratios caused about 0.002-in. difference in predicted values.

## PART V: CONCLUSIONS AND RECOMMENDATIONS

### Conclusions

146. Within the bounds (time and monetary limitations) of this investigation, the following conclusions are drawn:

- a. A nonstrain-hardening general deformation model that describes both elastic and inelastic behavior of soils, whether unbound or asphalt-bound, was developed.
- b. The model circumvents the need for yield surfaces or yield stresses separating elastic and inelastic behavior. Also, the model defines elastic plus inelastic behavior as they naturally and simultaneously occur.
- c. The model unifies soil behavior by being applicable to both cohesive and cohesionless materials.
- d. The model is applicable to soils whether in a pavement structure or beneath a foundation.
- e. The model is directly applicable to soil behavior for both laboratory and field test conditions.
- f. The model is applicable for both static and vibratory tests.
- g. The model can be established with laboratory tests and applied directly to field behavior and vice versa.
- h. Response to moving loads, such as a wheel, can be completely simulated in laboratory tests based on the model.
- i. Traffic distribution and mixed traffic on a pavement structure can be simulated in laboratory tests based on the model.
- j. The model characterizes soil behavior for any stress path.
- k. Soil stress distributions for field loading conditions can be derived from properties and requirements of the deformation model.
- l. The model applied to field conditions implies that soils (unbound and asphalt-bound) do not behave as continuum solids, such as portland cement concrete and steel materials.

147. After this study was completed and the report written, a reference (Reference 15) was found that verified much of the testing and findings of this study. In Reference 15, sand samples that were

subjected to stress reversal from compression to extension and vice versa were observed to have "directional independency." This reference further states,

Yielding of sand in reversing stress condition could occur independent of the previous stress history in an opposite direction. When shear stress in extension is reversed, the behavior in subsequent triaxial compression is almost the same as if the sample were not subjected to a previous cycle in extension. The memory of previous stress history does not appear in subsequent tests, and the sample behaves from the outset as if it were in a virgin state. The current deformation characteristics as a virgin sample are not erased even after the sample has been previously sheared in an opposite direction.

#### Recommendations

148. With regard to further development of the findings of this study, it is recommended that research, development, and testing validation be continued. The potentials of problem-solving capabilities and unification of the behaviors of different soil types should be exploited. Capitalization upon the potentials of the general deformation and stress distribution theory for soils can give unique capabilities in dealing with soils behaviors and problems.

## REFERENCES

1. O. J. Porter and Co., "Accelerated Traffic Tests at Stockton Airfield, Stockton, Calif., Stockton Test No. 2," 7 volumes, prepared for U. S. Engineer Office, Sacramento, Calif., May 1948.
2. Ledbetter, R. H. et al., "Multiple-Wheel Heavy Gear Load Pavement Tests; Presentation and Initial Analysis of Stress-Strain-Deflection and Vibratory Measurements; Data and Analysis," Technical Report S-71-17, Vol IIIB, Nov 1971, U. S. Army Engineer Waterways Experiment Station, CE, Vicksburg, Miss.
3. Ledbetter, R. H., "Pavement Response to Aircraft Dynamic Loads; Vol III: Compendium," Technical Report S-75-11, Vol III, Jun 1976, U. S. Army Engineer Waterways Experiment Station, CE, Vicksburg, Miss.
4. Chou, Y. T. and Ledbetter, R. H., "The Behavior of Flexible Airfield Pavements Under Loads--Theory and Experiments," Miscellaneous Paper S-73-66, Jul 1973, U. S. Army Engineer Waterways Experiment Station, CE, Vicksburg, Miss.
5. Schofield, A. N. and Wroth, C. P., "Critical State Soil Mechanics," McGraw-Hill Book Co., Inc., New York, New York, 1968.
6. Prévost, J. H. and Höeg, K., "Effective Stress-Strain-Strength Model for Soils," Journal of The Geotechnical Engineering Division, ASCE, Vol 101, No. GT3, Proc. Paper 11179, Mar 1975.
7. Lade, P. V. and Duncan, J. M., "Elastoplastic Stress-Strain Theory for Cohesionless Soil," Journal of the Geotechnical Engineering Division, ASCE, Vol 101, No. FT10, Proc. Paper 11670, Oct 1975.
8. Ledbetter, R. H., "Pavement Response to Aircraft Dynamic Loads; Presentation and Analysis of Data," Technical Report S-75-11, Vol II, Sep 1975, U. S. Army Engineer Waterways Experiment Station, CE, Vicksburg, Miss.
9. Ahlvin, R. G., Chou, Y. T., and Hutchinson, R. L., "The Principle of Superposition in Pavement Analysis," Highway Research Record No. 466, Highway Research Board, Washington, D. C.
10. U. S. Army Engineer Waterways Experiment Station, CE, "Investigations of Pressures and Deflections for Flexible Pavements," Technical Memorandum No. 3-323, 4 reports, Vicksburg, Miss., 1951-1954.

11. Highway Research Board, "The AASHO Road Test," 7 reports, Highway Research Board of the National Academy of Sciences - National Research Council, Washington 25, D. C., 1961-1962.
12. Donaghe, R. T. and Townsend, F. C., "Effects of Anisotropic Versus Isotropic Consolidation in Consolidated-Undrained Triaxial Compression Tests of Cohesive Soils," Technical Report S-75-13, Oct 1975, U. S. Army Engineer Waterways Experiment Station, CE, Vicksburg, Miss.
13. Al-Hussaini, M. M. and Townsend, F. C., "Investigation of  $K_o$  Testing in Cohesionless Soils," Technical Report S-75-16, Dec 1975, U. S. Army Engineer Waterways Experiment Station, CE, Vicksburg, Miss.
14. Taylor, D. N., "Fundamentals of Soil Mechanics," John Wiley and Sons, Inc., New York, New York, 1948.
15. Tatsuoka, F. and Ishihara, K., "Drained Deformation of Sand Under Cyclic Stresses Reversing Direction," Japanese Society of Soil Mechanics and Foundation Engineering, Vol 14, No. 3, Sep 1974.

In accordance with letter from DAEN-RDC, DAEN-ASI dated 22 July 1977, Subject: Facsimile Catalog Cards for Laboratory Technical Publications, a facsimile catalog card in Library of Congress MARC format is reproduced below.

Ledbetter, Richard H

General deformation (elastic and inelastic) and stress distribution theory in soils / by Richard H. Ledbetter. Vicksburg, Miss. : U. S. Waterways Experiment Station, 1977.

119 p. : ill. ; 27 cm. (Technical report - U. S. Army Engineer Waterways Experiment Station ; S-77-10)

Prepared for Assistant Secretary of the Army (R&D), Washington, D. C., under Project No. 4A161101A91D.

References: p. 118-119.

1. Cohesionless soils. 2. Cohesive soils. 3. Elastic deformation. 4. Inelastic behavior. 5. Live loads. 6. Pavements. 7. Soils. 8. Static loads. 9. Stress distribution. 10. Vibratory loads. I. Series: United States. Waterways Experiment Station, Vicksburg, Miss. Technical report ; S-77-10.

TA7.W34 no.S-77-10